Ing. Jürgen Hinterreiter, BSc MSc

Multi-Viewpoint Solar Wind Modeling in Comparison to In-situ Measurements

MASTER'S THESIS

to achieve the university degree of

Diplom-Ingenieur

Master's degree programme: Space Sciences and Earth from Space

submitted to

Graz University of Technology

Supervisor

Assoz. Univ.-Prof. Dr. Manuela Temmer

Institute of Physics
University of Graz

Graz, March 2018

AFFIDAVIT

I declare that I have authored this thesis independently, that I have not used other than the declared sources/resources, and that I have explicitly indicated all material which has been quoted either literally or by content from the sources used. The text document uploaded to TUGRAZonline is identical to the present master‘s thesis.

Date

Signature

Acknowledgment

I would first like to thank my supervisor Dr. Manuela Temmer for the help throughout the project and the whole process of writing this master's thesis. Her door was always open to me whenever I struggled with programming or found myself in a writer's block.

I am grateful for having been given the possibility to attend the 14^{th} European Space Weather Week in Ostend, Belgium in 2017 and the General Assembly of the European Geoscience Union in Vienna, Austria in 2018. These experiences certainly broadened my horizon.

I would also like to thank the CCSOM science team for accepting me in their project and providing the EUHFORIA data.

In addition, I want to thank my colleagues at the institute for countless inspiring discussions, not only regarding my master thesis but also other topics.

Finally, I want to give special thanks to my loved ones, who have supported me throughout my studies.

Abstract

This thesis presents statistical results from a thorough comparison between modeled and observed solar wind parameters. Successfully modeling the solar wind is an important input for Space Weather forecasting and to better understand the physics of the interplanetary propagation of coronal mass ejections. To simulate the background solar wind, we applied different empirical and numerical models. In a first approach, we evaluate the performance of empirical models that are based on in-situ and EUV data. The fractional areas of coronal holes (CHs) are extracted from STEREO and SoHO/SDO EUV data and compared to each other. The STEREO in-situ measured solar wind speeds are then adjusted according to the evolution of the CHs in order to improve the forecast at Earth. The performance of the model is evaluated by comparing the results to a persistence model based on ACE in-situ measurements for the time period January 2008 to December 2012. With the STEREO persistence model including the information of the CH evolution (STEREO+CH), 12% more high-speed streams (HSS) are correctly predicted and the number of false alarms and misses is decreased by 19% and 23% compared to the ACE persistence model. The uncertainty for predicting the arrival times of HSS lies within less than one day ($dt = 0.11 \pm 0.86$ hours). Second, the results of two numerical models (EUHFORIA and ENLIL) are compared to each other. EUHFORIA (EUropean Heliospheric FORecasting Information Asset) is a new forecast model for the inner heliosphere. It is still under development which is performed within the CCSOM (Constraining CMEs and Shocks by Observations and Modelling) project. ENLIL, on the other hand, is an already operational forecast model to simulate the structure and the evolution of the solar wind. We investigate the model results for a limited time range covering in total seven months for times of low (four months in 2008) and high (three months in 2012) solar activity. We find that the solar wind parameter best modeled by EUHFORIA and ENLIL is the solar wind bulk speed v_b, with a better performance of ENLIL ($\mathrm{RMSE}_{ENLIL} = 102$ km/s, $\mathrm{RMSE}_{EUHFORIA} = 132$ km/s for the year 2008, which corresponds to about 30% of the mean measured solar wind speed). ENLIL also gives better predictions for the density n, pressure P, temperature T, total magnetic field B_t, and the B_z component of the magnetic field compared to EUHFORIA, but the RMSE of each of the individual parameters is in the order of the mean measurement or even higher. In general both models underestimate the solar wind speed v_b and overestimate the density n.

Kurzfassung

In dieser Arbeit wird ein umfassender Vergleich von modellierten und beobachteten Sonnenwind Parametern durchgeführt. Erfolgreiches Modellieren des Sonnenwindes ist ein wichtiger Aspekt für die Vorhersage des Weltraumwetters und trägt dazu bei, die Physik der interplanetaren Ausbreitung von koronalen Massenauswürfen zu verstehen. Um den ruhigen Sonnenwind zu simulieren, werden verschiedene empirische und numerische Modelle verwendet. Zuerst wird die Performance von empirischen Modellen, basierend auf in-situ und EUV-Daten, evaluiert. Dazu werden die extrahierten Flächen von koronalen Löchern, beobachtet von unterschiedlichen Raumsonden (STEREO und SoHO/SDO) im EUV-Wellenlängenbereich, miteinander verglichen. Die von STEREO in-situ gemessene Sonnenwindgeschwindigkeit wird dann entsprechend der Entwicklung des koronalen Loches angepasst. Die Performance des Modells wird evaluiert und dann mit den Ergebnissen eines, auf ACE in-situ Messungen basierenden, Persistenz-Modells verglichen. Dazu werden Daten aus dem Zeitraum Januar 2008 bis Dezember 2012 herangezogen. Das STEREO Persistenz-Modell, unter Berücksichtigung der Entwicklung des koronalen Loches (STEREO+CH), liefert im Vergleich zum ACE Persistenz-Modell 12% mehr richtig prognostizierte schnelle Sonnenwindströme (High-Speed Streams, HSS), produziert 19% weniger Fehlalarme und reduziert die Zahl der beobachteten aber nicht richtig vorhergesagten HSS um 23%. Die Unsicherheit der prognostizierten Ankunftszeiten von HSS beträgt weniger als einen Tag ($dt = 0.11 \pm 0.86$ Stunden). In weiterer Folge werden zwei numerische Modelle (EUHFORIA und ENLIL) miteinander verglichen. Im Rahmen des CCSOM (Constraining CMEs and Shocks by Observations and Modelling) Projektes entstand EUHFORIA (EUropean Heliospheric FORecasting Information Asset), ein sich noch in Entwicklung befindliches Vorhersagemodell für die innere Heliosphäre. Im Gegensatz dazu ist ENLIL ein Vorhersagemodell, das bereits angewendet wird, um die Struktur und Entwicklung des Sonnenwindes zu simulieren. Die Modellergebnisse von insgesamt sieben Monaten zu Zeiten von geringer (vier Monate im Jahr 2008) und hoher (drei Monate im Jahr 2012) Sonnenaktivitätwerden untersucht. Es zeigt sich, dass die Sonnenwindgeschwindigkeit v_b der Parameter ist, der am besten von EUHFORIA und ENLIL vorhergesagt wird. ENLIL gelangt dabei zu besseren Ergebnissen ($\mathrm{RMSE}_{ENLIL} = 102$ km/s, $\mathrm{RMSE}_{EUHFORIA} = 132$ km/s, für das Jahr 2008), wobei RMSE_{ENLIL} ungefähr 30% des Mittelwerts der beobachteten Sonnenwindgeschwindigkeit beträgt. ENLIL liefert im Vergleich zu EUHFORIA auch bessere Resultate für Dichte n, Druck P, Temperatur T, Gesamtmagnetfeld B_t und die B_z-Komponente des Magnetfelds, jedoch ist der RMSE etwa so groß, oder sogar größer als der Mittelwert der Messung des jeweiligen Parameters. Generell unterschätzen die beiden Modelle die Sonnenwindgeschwindigkeit v_b und überschätzen die Dichte n.

Contents

1. Introduction

The Sun is the host star of our solar system and thus it is the closest star. Hence, the Sun is the driving factor for Earth's climate, it influences the magnetosphere and determines the near Earth space environment. As a consequence, the Sun is responsible for disturbances in our space environment. It emits a continuous stream of plasma, the so called solar wind, but also releases a huge amount of matter during coronal mass ejections (CMEs). CMEs are clouds of magnetized plasma that are expelled from the Sun with speeds of several hundreds up to a few thousand kilometers per second. The occurrence of CMEs strongly depends on the solar activity and in particular on the Schwabe cycle that lasts approximately 11 years (Aschwanden, 2005). It starts with sunspots forming at heliographic latitudes of $\sim 30° - 40°$ and over time, new sunspots form closer to the solar equator. This leads to the famous butterfly diagram when plotting the heliographic latitudes of the sunspots as a function of time. There exists an east-west orientation of the magnetic field in sunspot groups which is opposite in the northern and the southern solar hemisphere, switching every Schwabe cycle. The original magnetic configuration is restored approximately every 22 years and is called the Hale cycle, named after George Ellery Hale (Aschwanden, 2005).

The term "space weather" has been established over the last few decades. It is generally accepted that space weather refers to time-variable conditions of the Sun, in the solar wind, and within Earth's magnetosphere, ionosphere and thermosphere (Hanslmeier, 2002). When directed towards Earth, CMEs can cause magnetic storms in the space environment around Earth, the magnetosphere and the upper atmosphere. One of the most commonly known effects are the Northern Lights (aurora borealis) which can also be seen in the southern hemisphere where they are called aurora australis. Since the dependence of mankind on technology (space-borne and ground-based), is ever increasing also the effects of space weather are more noticeable. Figure 1.1 shows examples of nowadays technology that can be affected by space weather events. Therefore, social and economic aspects with the aim to avoid consequences of space weather events by system design or efficient warning and prediction exist (Hanslmeier, 2002). Severe conditions in space can lead to spacecraft charging and hinder or even damage satellite operations. Humans in space may be affected by radiation and particles, but also airplane crews and passengers on high altitude and high latitude flights may be harmed by cosmic rays that penetrate to the lower atmosphere. In addition, global satellite-based navigation system and satellite-ground communication may be influenced by space weather. Even power outages are possible, due to induced currents in the electrical transmission line facilities, which may endanger human health and live. Such a phenomenon actually happened in October

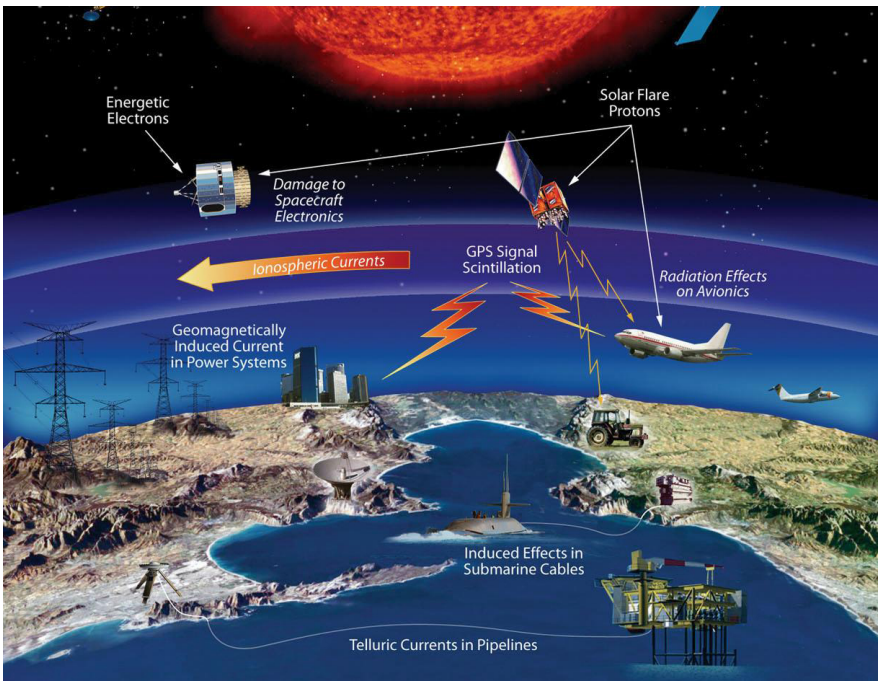

Figure 1.1.: Examples of technological infrastructure that may be affected by space weather events. From NASA[1].

2003 in Sweden and is related to the famous Halloween Storm (Hady, 2009).

Not only CMEs can have effects on Earth but also co-rotating interaction regions (CIRs), which are regions where the slow solar wind is compressed by the following high-speed solar wind streams (HSS), are able to create geomagnetic storms (Gosling and Pizzo, 1999; Foukal, 2004). A geomagnetic storm is defined as a temporary disturbance of the Earth's magnetic field by a solar wind shock wave or a magnetic cloud. The most severe geomagnetic storms are observed when the B_z component of the interplanetary magnetic field (IMF) is southward directed (Schwenn, 2006b). The prediction of the space weather, and especially the prediction of geomagnetic storms, is a very complex problem. One has to take interactions between the Sun, solar wind, Earth's magnetic field, and Earth's atmosphere into account. Transient events like CMEs have a lead time for the prediction of less than two days, which corresponds to the travel time of the magnetic cloud. The fast solar wind on the other hand can be regarded as recurrent phenomena (Schwenn, 2006b).

In the last decades more effort has been put in the space weather research and in the space weather prediction models. There already exist several empirical models, which use observation to predict future conditions (e.g., persistence models), and numerical forecast models, that solve magnetohydrodynamic (MHD) equations (e.g., ENLIL). CIRs are related to the fast solar wind that originates from long living coronal holes (CHs). As a consequence, the solar wind properties can be predicted

[1]https://solarscience.msfc.nasa.gov/dynamo.shtml [March 3, 2018]

using the measurements obtained 27.27 days prior. This time corresponds to the Carrington rotation which is the synodic rotation period of the Sun, where Carrington rotation 1 started on November 9, 1853. The so-called 27 day persistence model is the simplest way to forecast the solar wind (Owens et al., 2013). CMEs on the other hand cannot be predicted by the 27 day persistence model, since these are sporadic and transient events, therefore more sophisticated forecast models are needed. One can use in-situ and remote sensing data obtained by multiple spacecraft to predict the space weather at Earth. Measurements of the solar wind parameter at location east of Earth can be used to forecast the solar wind that will arrive a couple of days later at Earth location. A different approach to forecast space weather are physics-based numerical models that solve magnetohydrodynamic (MHD) equations. For such numerical models boundary conditions are needed where the initial information comes from the magnetic field of the Sun. Numerical models, like ENLIL and EUHFORIA, are three-dimensional time-dependent MHD simulations that self-consistently predict the propagation, evolution and interaction of the solar wind (Owens et al., 2008).

In this study we present a statistical analysis of the solar wind background properties. Particular emphasis is put on the comparison of the background solar wind bulk velocity which is predicted by different models. The selected time range covers periods of low solar activity (2008) and high solar activity (2012), where the models are believed to perform better during the low solar activity. The results of several empirical models based on different input data (in-situ ACE: Persistence model 27d; in-situ STEREO: Persistence model STEREO; in-situ STEREO + remote sensing data: Persistence model STEREO+CH) and the results of the numerical MHD simulations (ENLIL and EUHFORIA) are compared to in-situ measurements. The model results are compared based on continuous variables (e.g. mean absolute error, root-mean-square error) as well as on binary variables (hit, false alarm, miss).

The structure of the thesis is as follows: Chapter 2 gives an overview of the origin and the properties of the solar wind. In Chapter 3 follows a description of the instruments. In Chapter 4 the methods to compare in-situ measurements and model forecasts are presented. Chapter 5 describes the empirical and numerical models used in this study. Chapter 6 deals with the statistical results of the empirical models and the numerical models. Chapter 7 summarizes the study.

Publication (peer-reviewed) from the thesis:

Temmer, M., Hinterreiter, J., and Reiss, M. A. (2018). Coronal hole evolution from multi-viewpoint data as input for a STEREO solar wind speed persistence model. *Accepted for publication in SWSC.*

Poster presentations:

Hinterreiter, J., Temmer, M., Poedts, S., Pomoell, J., Verbeke, C., Kilpua, E., Asvestart, E., Rodriguez, L., Scolini, C., Magdalenic, J. (2017). EUHFORIA background solar wind modeling – validation within the CCSOM project. *14^{th} European Space Weather Week in Ostend, Belgium.*

Hinterreiter, J., Temmer, M., Verbeke, C., Poedts, S., Pomoell, J., Magdalenic, J., Scolini, C., Rodriguez, L., Kilpua, E., Asvestart, E. (2018). Validation of the background solar wind modeled by EUHFORIA. *General Assembly of the European Geoscience Union in Vienna, Austria.*

2. The Sun and Solar Wind

The Sun is the host star of our solar system, hence having large influence on Earth. With a total mass of $1.99 \cdot 10^{30}$ kg, a radius of $6.96 \cdot 10^5$ km, and a luminosity of $3.84 \cdot 10^{26}$ W, the Sun is the brightest object on the daytime sky (Bhatnagar and Livingston, 2005). The structure of the Sun is divided into the interior and the atmosphere. The first is made up of three different layers:

- **Core:** In this region the energy is produced by nuclear fusion of hydrogen.
- **Radiation zone:** The energy produced in the core is transferred outwards via radiation.
- **Convection zone:** In this layer the energy transport happens through convection.

The solar atmosphere consists of the:

- **Photosphere:** A thin layer representing the solar surface and emits the bulk of sunlight in the visible and IR spectrum and is therefore visible with the naked eye.
- **Chromosphere:** An inhomogeneous dynamic layer where the temperature increases with increasing height. It can be observed during solar eclipses or in narrow-band filters centered at strong absorption lines, like the Hα line of neutral hydrogen or the Ca II K line of ionized calcium.
- **Transition region:** A very thin region where the temperature abrubtly rises from 10^4 K to 10^6K.
- **Corona:** The outermost layer of the solar atmosphere consisting of highly rarefied gas.

2.1. The Solar Corona

As already mentioned, the solar corona is the extended outer atmosphere of the Sun. It reaches out into the interplanetary space and can be observed with coronagraphs that block out the direct sunlight, since the corona is approximately 10^{-6} times the brightness of the photosphere. In order to obtain on-disk observations of the corona, extreme ultraviolet (EUV) or soft X-ray (SXR) emission is used (Aschwanden, 2005). The plasma in the corona is a highly ionized proton-electron gas having very high kinetic temperatures (1–2$\cdot 10^6$ K). With increasing height the density in the corona decreases, which is estimated to be in the order of 10^8 cm^{-3} at about 1.5 $R_\odot$ (Mullan, 2000).

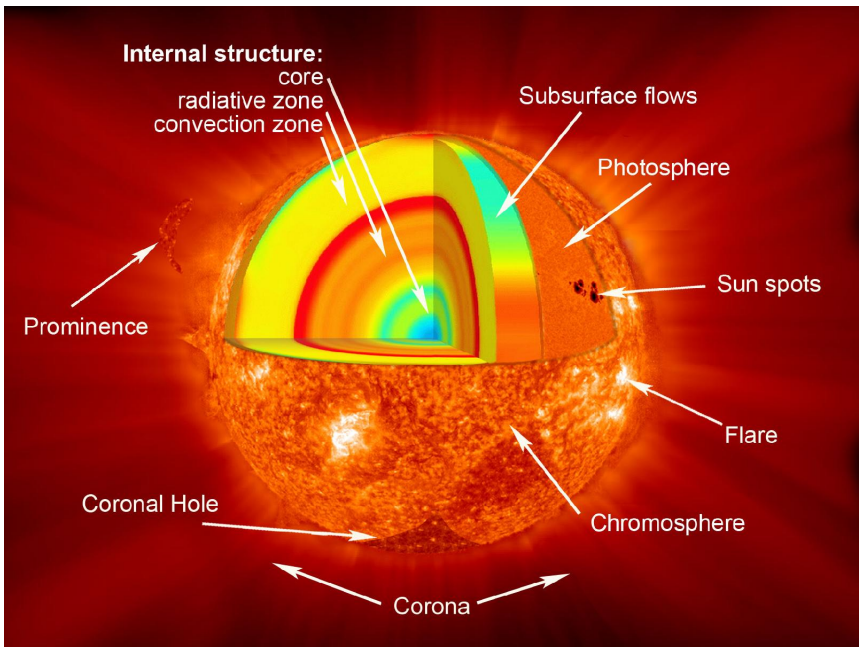

Figure 2.1.: Different layers of the Sun. From NASA[2].

The corona can be divided into three different parts:

1. K-corona (*kontinuierlich* is German for continuous),
2. F-corona (Fraunhofer corona),
3. E-corona (emission corona).

The K-corona (continuous corona) forms due to light coming from the photosphere that is scattered on free electrons and reaches out to about $2R_\odot$ (Foukal, 2004). The spectrum of the K-corona doesn't show any spectral lines, due to the Doppler broadening of the fast moving scattering electrons (T $\sim 2{\cdot}10^6$ K, leading to an electron speed of $\sim$10000 km/s). The F-corona (Fraunhofer corona) arises because the photospheric light is scattered on dust particles. These dust particles have much lower velocities, leading to absorption lines in the spectrum. The E-corona (emission corona) forms due to very high kinetic temperatures, leading to highly ionized atoms (e. g. Fe XIV, $\lambda = 530.3$ nm) that produce spectral emission lines (Foukal, 2004).

The corona is a very variable layer of the Sun's atmosphere. Depending on the solar activity, the shape and the intensity of the solar corona can largely differ. The top panel in Figure 2.2 shows the corona during a solar eclipse taken close to the solar minimum in 1994. Streamers can only be seen in low latitudes near the equator of the Sun. In contrast, the bottom panel shows the corona close to solar maximum in 1980 where the streamers can be found in all latitudes (Cranmer, 2009).

[2]https://www.nasa.gov/mission_pages/sunearth/multimedia/Sunlayers.html [March 12, 2018]

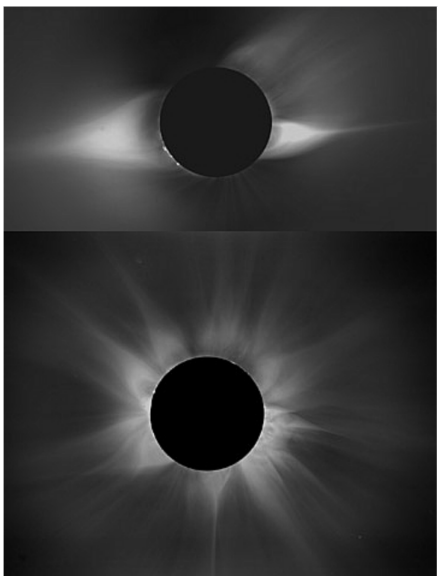

Figure 2.2.: Solar corona during a solar eclipse taken in 1994 near the solar minimum (top panel) and in 1980 near the solar maximum (bottom panel). From UCAR[3].

2.1.1. Coronal Holes (CH)

In the late 1960s observations of the Sun in X-ray and UV with space-borne instruments led to the discovery of dark areas on the solar disk with very low coronal emission. These structures are called "Coronal Holes" (CHs). Above the limb CHs can be observed as areas with low density in the coronographic white light images. CHs are long living features, which appear dark because these areas show a constant outflow of plasma leading to low density, low temperatures, and low pressure. The plasma outflow is possible because CHs are characterized by "open" magnetic field lines, i.e. field lines which close at large distances to the Sun, reaching far out into the interplanetary space (Cranmer, 2009). The magnetic field of CHs is known to have a dominant polarity, because the field lines do not close in the CHs or in the vicinity of CHs. During the minimum phase of the solar cycle, CHs are predominately found on the solar poles. During the maximum phase CHs may appear at all heliographic latitudes and many of them are located at the edge of active regions (Cranmer, 2009). However, in low latitudes they may only persist for a couple of solar rotations. In contrast to the underlying photosphere, CHs rotate more like a rigid body (Timothy et al., 1975). The abundances of the ions coming from CHs match those of the photosphere with electron temperatures of about 0.8 MK and proton temperatures of roughly 3 MK. An additional evidence for the outflow of plasma is that the radiation within CHs is blue shifted. Studying CHs is of particular interest for space weather forecasts, since they are associated with high-speed streams (HSS) and are responsible for geomagnetic activity at 1 AU (astronomical unit: $1.496 \cdot 10^{11}$ m), when interacting with the slow solar wind (Cranmer, 2009). CHs are usually best visible

[3]https://scied.ucar.edu/sun-corona-solar-min-max [March 12, 2018]

in the 195 Å wavelength (Lemen et al., 2012) and Figure 5.2 shows a CH observed on February 22, 2011 by STEREO/SECCHI (left) and six days later by SDO/AIA (right).

2.2. The Solar Wind

Since the plasma in the corona is not in hydrostatic equilibrium, particles are constantly ejected from the Sun. This stream of particles is called the "solar wind" (introduced by Eugene Parker) and expands in the interplanetary space forming the heliosphere. Every year the Sun loses about $2{\cdot}10^{-14}$ $M_\odot$ (Aschwanden, 2005). The solar wind streams into space until it is stopped by the low pressure interstellar medium, which happens at about 100 AU. At this distance the so-called heliopause is forming, which is more or less defining the limits of the solar system. Studying the solar wind started in the 1950s with Ludwig Biermann and the observation of comets. He found that comets have two different tails. One is due to the radiation pressure of the Sun and the other arises from the plasma pressure and has a different direction and shape. Biermann postulated that the second tail, the plasma tail, arises due to a particle stream from the Sun (Biermann, 1951). The existence of the solar wind was then confirmed about 10 years later by the US spacecraft Mariner 2, which measured a constant stream of charged particles on the way to Venus (Neugebauer and Snyder, 1966). In the late 1950s the first models describing the extending corona giving rise to the particle radiation were published and are described in the following.

Chapman Model

Chapman and Zirin (1957) first tried to give an explanation of the solar wind. They assumed a static corona, which is spherically symmetric, has a high thermal conductivity and no energy sources or sinks. Their results showed that the corona cannot be limited, but has to reach out far into the interplanetary space. They presumed a small temperature gradient of the corona which leads to small density gradients. As a consequence, they obtain density values at 1 AU of about 100 cm^{-3}, which is roughly an order of magnitude too high. At that time, this was in agreement with the electron density required to explain the zodiacal light, which is a faint conical glow in the night sky caused by sunlight scattering (Bhatnagar and Livingston, 2005). This turned out later to be incorrect, since the zodiacal light is mainly caused by the interplanetary dust. Also the expected low pressure in the interstellar medium was not matched by the high hydrostatic plasma pressure of this model (Foukal, 2004). As a consequence, the solar wind is not able to merge with the interstellar medium which was the major point of criticism of Eugene Parker.

Parker Model

Parker (1958) suggested that the corona is in a dynamic state of constant expansion and not in hydrostatic equilibrium far away from the Sun. With this model he was able to find a solution with vanishing pressure at large distances from the Sun,

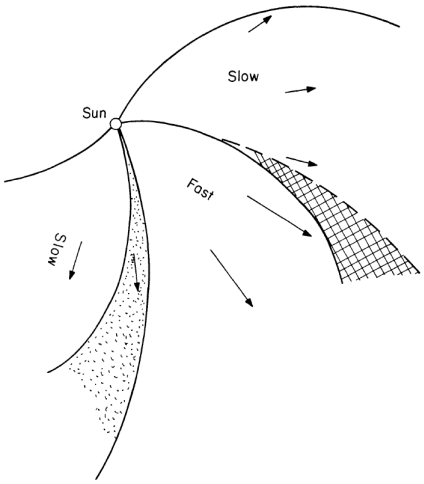

Figure 2.3.: Schematic illustration of the Parker spiral with the slow and fast solar wind with a SIR. From Parker (1965).

making it possible that the solar wind merges with the interstellar medium. In addition, Parker was also able to explain the formation of the interplanetary magnetic field.

In interplanetary space the conductivity, due to free electrons and ions, is very high. As a consequence, the magnetic field and the plasma are tied to each other, i.e. frozen-in. The plasma β is the ratio of the thermal pressure to the magnetic pressure and describes if the plasma has to follow the magnetic field or vice-versa. It is defined as:

$$\beta = \frac{nk_bT}{B^2/(2\mu_0)}, \tag{2.1}$$

where n is the particle density, k_b is the Boltzmann constant, T is the temperature, B is the magnetic field strength and μ_0 is the vacuum permeability. In the solar wind β>1, meaning that the plasma is dominating and the magnetic field has to follow. The shape of the solar wind streams, and therefore the interplanetary magnetic field, can be explained by the radial outflow velocity and the rotation of the Sun. As a consequence the so-called "Parker spiral" forms (see Figure 2.3). It is intuitive that the curvature of the solar wind stream depends on the speed but also on the distance to the Sun. Slow solar wind streams show higher curvature than fast streams and in farther distances to the Sun also the curvature increases. At the distance of Earth (1 AU) and assuming a moderate solar wind speed of 400 km/s the curvature of the solar wind stream is about 45° (Foukal, 2004). Parker also predicted regions of compression, where the fast wind coming from CHs outruns the slow solar wind and creates the so-called stream interaction regions (SIR).

Alfvén (1977) first proposed a three-dimensional model for the heliosphere and the structured solar wind, the so-called "Ballerina model" (see Figure 2.4). It describes the heliosphere of the quiet Sun when the solar magnetic field is roughly a dipole.

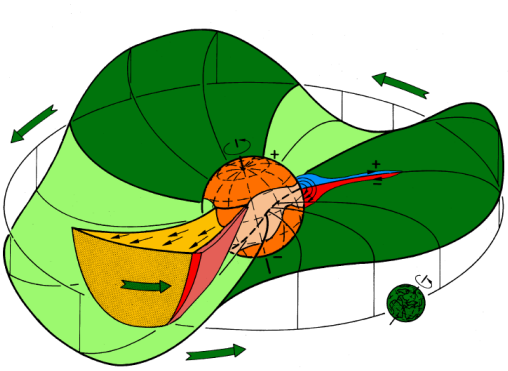

Figure 2.4.: Ballerina model for the three-dimensional inner heliosphere near the solar minimum according to Alfvén (1977). In equatorial regions streamer belts can be seen with loop-like and mainly closed magnetic structures. Large CHs appear on the solar poles where the southern hole has negative (inward directed) polarity and the northern hole positive polarity, having an extension reaching down to low latitudes, leading to a curved neutral line. From Schwenn (2006b).

Table 2.1.: Summary of characteristic solar wind parameters for a time of low solar activity at Earth. From Schwenn (2006b).

Solar Wind Parameter	Slow Solar Wind	Fast Solar Wind
Flow speed v_p	250–400 km s^{-1}	400–800 km s^{-1}
Proton density n_p	10.7 cm^{-3}	3.0 cm^{-3}
Proton flux density $n_p v_p$	$3.7 \cdot 10^8$ cm^{-2} s^{-1}	$2.0 \cdot 10^8$ cm^{-2} s^{-1}
Proton temperature T_p	$3.4 \cdot 10^4$ K	$2.3 \cdot 10^5$ K
Electron temperature T_e	$1.3 \cdot 10^5$ K	$1.0 \cdot 10^5$ K
Momentum flux density	$2.12 \cdot 10^8$ dyn cm^{-2}	$2.26 \cdot 10^8$ dyn cm^{-2}
Total energy flux density	1.55 erg cm^{-2} s^{-1}	1.43 erg cm^{-2} s^{-1}
Helium content n_p/n_{He}	2.5%, variable	3.6%, stationary

The heliosphere is divided by a separatrix in regions of different polarities since the magnetic field lines are dragged out by the solar wind. The magnetic neutral line is warped, making the heliospheric current sheet look like a ballerina skirt (Schwenn, 2006b). A switch in the polarity can be noticed when, i.e. a spacecraft passes a region where slow and fast solar wind interact. The so-called magnetic sector boundary reappears with a periodicity of roughly 27 days (synodical rotation period of the Sun) since the whole system rotates with the Sun.

As already mentioned, the solar wind is a steadily streaming outflow of plasma from the solar corona in all directions along the magnetic field lines. Because of the high temperatures it is a fully ionized plasma mainly consisting of electrons and protons, with minor fraction of helium ions and some heavier nuclei in different

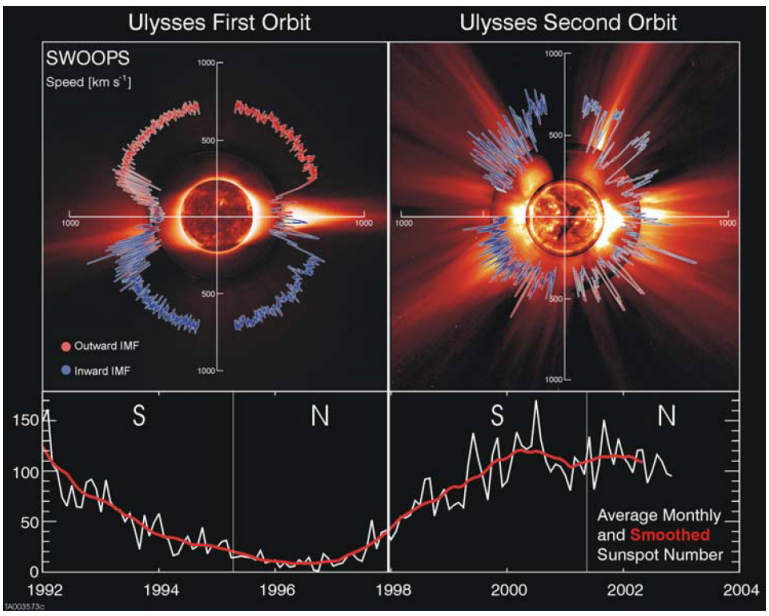

Figure 2.5.: Polar plots of the solar wind speed measured by Ulysses for the first orbit (top left panel) and second orbit (top right panel). The sunspot number (bottom panel) indicates that the first orbit occurred during solar minimum whereas the second orbit occurred during solar maximum. From McComas et al. (2003).

ionization levels. Typical solar wind speeds at a distance of about 1 AU are in the order of 400 km/s up to 800 km/s. The density is in the range of about 5 cm^{-3}, the temperature is roughly 10^5 K, and the magnetic field strength about 5 nT (Schwenn, 2006b). The acceleration of the solar wind due to the pressure gradient would result in a solar wind speed of only up to 200 km/s. Hence, an additional energy input for the measured speeds of up to 800 km/s is needed. The source of this additional energy is still unknown and can be relating to the coronal heating problem. The most promising theories, however, include heating through the dissipation of waves and microflares (Cranmer, 2004). The speed of sound in the interplanetary medium at Earth location is about 40–70 km/s, hence the solar wind is highly super-sonic and super-Alfvénic. As indicated earlier, the solar wind can be divided into two different components. The slow solar wind and the fast solar wind. They differ not only in the velocity, as indicated by their names, but also the other parameters show differences. Table 2.1 lists parameter values for the fast and the slow wind according to Schwenn (2006b).

Most of the spacecraft measure the solar wind properties in the ecliptic plane (e.g., Wind, ACE, STEREO). Ulysses, in contrast, was launched in 1990 with the aim to study the inner heliosphere in high latitudes. After a gravity-assist maneuver at Jupiter in 1992 the spacecraft was put in a solar orbit with an inclination of about 80° (Wenzel et al., 1992). During the first orbit, corresponding to a solar minimum, Ulysses passed over the south pole of the Sun in 1994 reaching the north pole in 1995 (see top left panel in Figure 2.5). It can be seen that during solar minimum the slow

wind is limited close to the equatorial plane whereas at high latitudes the fast wind dominates. In addition, the interplanetary magnetic field is strongly correlated to the Sun's hemispheres. In its second orbit, Ulysses passed the poles in 2000 and 2001, which corresponds to times of maximum solar activity (top right panel in Figure 2.5). At these times the slow and fast winds are not restricted to any latitudes and also the different polarities appear in both hemispheres (McComas et al., 2003).

2.2.1. Slow Solar Wind

The slow solar wind reaches speeds of up to 400 km/s and can be divided in the slow wind of minimum type and slow wind of maximum type. The difference lies in the helium ion content, which is for the slow wind of maximum type about 4% compared to less than 2% for the slow wind of minimum type. Coronal streamers are phenomena ranging farest over the limb and connect regions of different polarities and are believed to be one source of the slow solar wind. They prevent the plasma from escape until a certain height above the surface. At these heights the magnetic field strength weakens and the gas pressure may then be high enough for the plasma to escape (Schwenn, 2006a). Also helmet-streamers, which are bright arcs with a long radial needle, are thought to be a source of the slow solar wind. Another source are CHs next to active regions or polar CHs that vanish before the solar activity maximum. Sakao et al. (2007) detected at the edge of an active region, adjacent to a CH, a pattern of continuous outflow using Doppler shift methods on the basis of Extreme Ultra-Violet Spectrometer data onboard Hinode. They estimate the temperature and density and suggest a loss rate of about 25% of the total mass loss rate of the solar wind.

2.2.2. Fast Solar Wind

The fast solar wind, also called high-speed streams (HSS), may reach speeds that are about a factor of two faster then the slow solar wind speeds, leading to roughly 800 km/s. Also the proton temperature is higher whereas the density is lower (Schwenn, 2000). HSS are believed to originate from CHs and often fill the majority of the volume of the heliosphere. The location of CHs depends on the solar cycle, therefore the fast solar wind dominates at high latitudes (greater than $\pm$20–30°) during the solar minimum. Since CHs are long-living structures on the Sun also the fast wind reappears with every solar rotation, approximately every 27 days. The abundance of the fast solar wind is more comparable to that of the photosphere than to the abundance of the slow solar wind, indicating that the source region of HSS are located deeper in the corona. HSS contain about 95% hydrogen ions, 5% helium ions, heavier ions and free electrons (Cranmer, 2002).

2.2.3. Co-rotating Interaction Regions (CIRs)

The structure of the helisophere is formed by the outflow of plasma from the Sun. In some regions of interplanetary space, where the fast solar wind is east of the slow

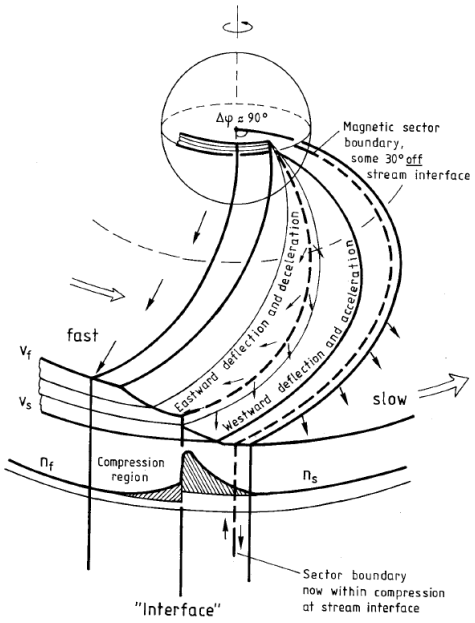

Figure 2.6.: Idealized view of a stream interaction region. From Schwenn (1990).

solar wind, the HSS may catch up to the slow wind, leading to interaction regions of the two solar wind components. Such regions are called stream interaction region (SIR), where the density, pressure, and the magnetic field is enhanced. Figure 2.6 shows an idealized view of a SIR where the fast wind originates east from the slow wind. At the "interface" the increase in the density is illustrated. Since HSS originate from long living CHs, the stream interaction regions may remain for several solar rotations. In such cases the interaction region is called co-rotating interaction region (CIR) and can be observed roughly every 27 days. The streams with higher velocity show smaller curvature, leading to a compression region when interacting with the slow solar wind stream. The particles are frozen-in to the interplanetary magnetic field, which results in a compression. The farther away from the Sun, the stronger the compression gets, leading to the increased density, pressure, and magnetic field (Gosling and Pizzo, 1999; Foukal, 2004). HSS can lead to geomagnetic storms when interacting with Earth's magnetosphere. Also shock fronts may be formed, since the solar wind speed is super-sonic and super-Alfvénic at distances of 1 AU.

2.2.4. Coronal Mass Ejections (CMEs)

Coronal mass ejections (CMEs) are clouds of magnetized plasma which are expelled from the Sun. In CMEs huge amounts of plasma (up to 10^{12} kg), reaching speeds of several hundreds up to a few thousand kilometers per second, are ejected. In an ideal case a CME shows an apparent three-part structure with an outer loop, followed by

a dark void and a bright kernel. A CME is defined (following Hundhausen et al., 1984; Schwenn, 1996) as an observable change in the coronal structure that:

1. occurs on a time scale of a few minutes up to several hours and
2. involves the appearance (and outward motion) of a new, discrete, bright, white light feature in the coronagraph field of view.

Often, fast CMEs drive large scale density waves out into the interplanetary space. Here the waves may steepen and produce collisionless shock waves, since the interplanetary space can be considered as a collisionless plasma with mean free paths of a few AU. At the shock front, the outer boundary of a plasma sheath, heating and deflection of the ambient solar wind happens. In contrast to CIRs, CMEs can be considered as transient events, which strongly disrupt the interplanetary space. A CME moving towards Earth, with a southward directed magnetic field, may strongly disturb Earth's magnetic field causing aurorae and geomagnetic storms (Schwenn, 2006b).

2.2.5. Interplanetary Shocks

CMEs traveling in the interplanetary space usually drive shock waves ahead of their leading edges. Also CIRs are able to drive shock waves but those are more frequently driven at further distances than 1 AU (Schwenn, 2006b). In a magnetized plasma three different MHD wave modes can propagate: fast, Alfvén, and slow wave modes, having three different corresponding characteristic velocities: fast (v_f), Alfvén (v_A), and slow (v_s) speeds. According to the speeds, slow, intermediate (Alfvén), and fast shocks may occur, but only the strong fast interplanetary shocks result in a significant magnetospheric response. The main driver for the fast shocks are CMEs and CIRs. The most important parameters that define the characteristics of an interplanetary fast shock are the magnetosonic Mach number M_{ms}, the plasma β, and the angle between the shock normal and the upstream magnetic field Θ_{Bn}. M_{ms} is an indicator of the shock strength, i.e. the energy processed by the shock (Burgess and Scholer, 2015). It is defined as:

$$M_{ms} = \frac{v_{flow}}{v_{ms}}, \tag{2.2}$$

where v_{flow} is the normal component of the solar wind speed and v_{ms} is the magnetosonic speed. It is given by:

$$v_{ms} = \sqrt{v_A^2 + c_s^2}, \tag{2.3}$$

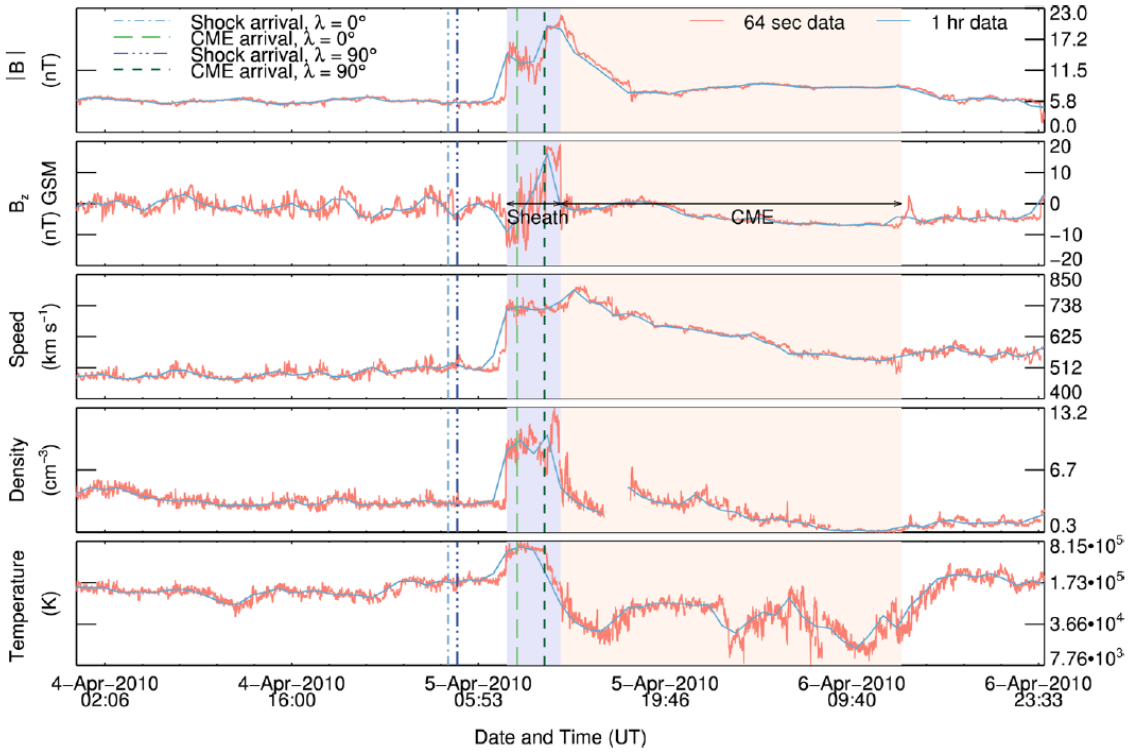

Figure 2.7.: ACE plasma and magnetic-field in-situ measurements for the 64 seconds data (red) and the 1 hour data (blue) in April 2010. The gray area indicates the sheath shock region, whereas the orange region corresponds to the CME. The vertical lines represent the shock and CME arrival times estimated by a stereoscopic self-similar-expansion model with different angular half-widths λ. Shown is from top to bottom: total magnetic field $|B|$, B_z component of the magnetic field, solar wind speed, density, and temperature. Adapted from Volpes and Bothmer (2015).

with the Alfvén speed v_A and the sound speed c_s defined as:

$$v_A = \frac{B}{\sqrt{\mu_0 \rho_p}}, \tag{2.4}$$

$$c_s = \sqrt{\gamma k_B (T_p + T_e) m_p^{-1}}. \tag{2.5}$$

In the equations above B is the magnetic field strength, μ_0 the vacuum permeability, ρ_P the proton density, γ the polytropic index, k_B the Boltzmann constant, m_p the proton mass, T_P and T_e the proton and electron temperature, respectively. The shock angle Θ_{Bn} controls the behavior of the particles that are propagating to the shock. As a consequence, quasi-perpendicular Θ_{Bn}>45° and quasi-parallel Θ_{Bn}<45° shocks have different internal structure. The latter are associated with extended foreshock regions having more gradual shock transitions, meaning that the jumps in the solar wind parameters and in the magnetic field magnitude are less distinct than for quasi-perpendicular shocks (Burgess and Scholer, 2015). The vector perpendicular to the shock front, the shock normal vector, can be calculated for all interplanetary shocks when having at least one in-situ measurement. Since CMEs propagate with very high velocities, making them travel in a radial direction, the shock normal is close to the Sun-Earth line. In contrast, the shock normals are often inclined for CIR driven shocks because the compression region follows the Parker spiral (Oliveira and Samsonov, 2018).

The solar wind plasma and magnetic field measurements obtained by ACE at a time when a CME was passing over the satellite are shown in Figure 2.7. Shown is the sheath shock (gray area) which is followed by the CME (orange area). The vertical lines indicate times, according to a stereoscopic self-similar-expansion model with the angular half-width λ, when the shock and the CME arrived (Volpes and Bothmer, 2015). It can be seen that when the shock passed the satellite, an increase in the total magnetic field $|B|$, the B_z component of the magnetic field, solar wind speed, density, and temperature is observed. Not shown in Figure 2.7 are B_x and B_y which are also measured by the spacecraft. When shocks hit Earth the magnetosphere is compressed leading to disturbances in the geomagnetic space around Earth but even on ground. Also the direction of the magnetic field of the shock has an influence on the geoeffectiveness. Shocks with a southward directed magnetic field usually produce the strongest geomagnetic storms. Due to the compression also heating of the highest layers of Earth's upper atmosphere can be observed (Oliveira and Samsonov, 2018). Figure 2.8 schematically illustrates the changes of the solar wind parameters for shocks driven by CMEs (left) and by CIRs (right). For CMEs usually a steep increase of the magnetic field B, one of the Cartesian magnetic field components B_i, velocity V, density N, and temperature T is observed, which then decreases gradually, except for T. This profiles are quite well matched by the ACE in-situ observations in Figure 2.7. CIRs, in contrast, reveal a different behavior, where the parameters already show a gradual increase. The *Dst*-index, which mainly corresponds to the ring current in the Earth's magnetosphere, and the electron flux e^- show quite similar profiles.

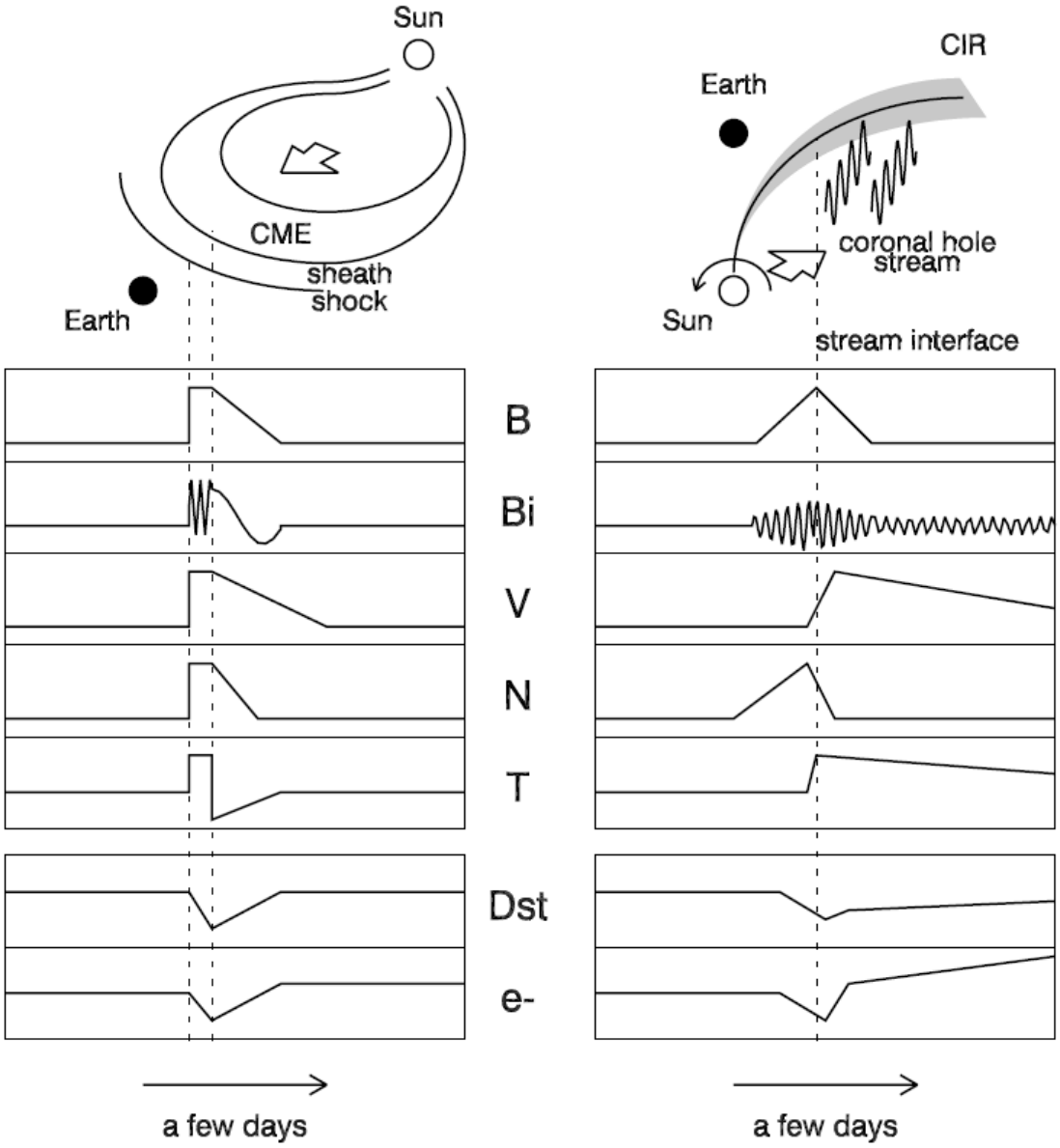

Figure 2.8.: Schematic representation of solar wind structures for CMEs (left) and CIRs (right). From top to bottom: total magnetic field B, one of the magnetic field components B_i, solar wind speed V, density N, temperature T, response of the Dst-index, and the >2.0 MeV electron flux e^-. From Kataoka and Miyoshi (2006).

3. Instruments

For this study, we use data from different satellites and spacecraft. The in-situ data, consisting of solar wind speed, density, temperature, and the magnetic field components, give the plasma conditions in the interplanetary space whereas images from the Sun are used to infer to the sources of the fast solar wind.

3.1. Advanced Composition Explorer (ACE)

The Advanced Composition Explorer (ACE), launched on August 15, 1997, is an Explorer mission managed by NASA and entered its Lissajous orbit (quasi-periodic orbital trajectory) close to L_1 (Lagrangian point; about 1.5 million km sunward in the Earth-Sun line) on December 12, 1997. ACE is designed to determine and compare the elemental composition of several distinct samples of matter, including e.g. the solar corona and the interplanetary medium. One of the goals is to study the acceleration of the solar wind, any charge and/or mass-dependent fractionation in various types of the solar wind flows, and to determine the elemental and isotopic composition of the solar corona. Due to its orbit, ACE is also able to measure the interplanetary magnetic field and properties of the solar wind before it impacts Earth's magnetosphere and can therefore be used to forecast space weather. ACE provides an ideal data set for heliospheric multi-spacecraft studies which can be used in conjunction with other observations from spacecraft such as STEREO (Stone et al., 1998). ACE consists of nine instruments:

1. Cosmic Ray Isotope Spectrometer (CRIS),
2. Solar Isotope Spectrometer (SIS),
3. Ultra Low Energy Isotope Spectrometer (ULEIS),
4. Solar Energetic Particle Ionic Charge Analyzer (SEPICA),
5. Solar Wind Ions Mass Spectrometer (SWIMS) and Solar Wind Ion Composition Spectrometer (SWICS),
6. Electron, Proton, and Alpha-particle Monitor (EPAM),
7. ACE Real Time Solar Wind (RTSW),
8. Solar Wind Electron, Proton and Alpha Monitor (SWEPAM),
9. Magnetometer (MAG).

For the study in this thesis SWEPAM and MAG data is used and the instruments are described in the following.

Solar Wind Electron, Proton and Alpha Monitor (SWEPAM)

SWEPAM is a modified version of the solar wind electron and ion sensor used for the Ulysses mission. It is designed to measure the three-dimensional characteristics of the bulk solar wind (electron from 1 to 900 eV and ions from 0.26 to 35 keV, Stone et al., 1998). The advanced three-dimensional plasma instrumentation provide observations of the elemental and isotopic composition at L_1 and allow the examination of different solar wind phenomena such as the low-speed streamer belt flows, the high-speed solar wind from CHs, the solar wind structure, interplanetary shocks, and coronal mass ejections. In addition, SWEPAM is one of the four instruments that provides a 24-hour monitoring of the space weather. Solar wind plasma conditions are provided every 64 seconds to the international space physics community (McComas et al., 1998).

Magnetometer (MAG)

The ACE magnetic field experiment (MAG) is a fully redundant triaxial flux-gate magnetometer that provides continuous measurements of the dynamic behavior of the vector magnetic field in the interplanetary medium. MAG is a reconditioned flight spare of the WIND/MFI experiment (Lepping et al., 1995). The twin-pair triaxial flux-gate sensors of MAG are mounted on booms with a distance of 8.38 m distance to each other. Due to the position of ACE at L_1, MAG establishes the large scale structure of the interplanetary magnetic field (IMF) and measures the characteristics of the IMF fluctuations over a wide range of frequencies. NOAA provides real-time observations with 1 second resolution (accuracy of $\pm$ 0.1 nT) for near-instantaneous space weather studies (Smith et al., 1998).

The observations of SWEPAM, MAG and the other instruments on ACE are used to enhance predictions of the space weather environment near Earth.

3.2. Deep Space Climate Observatory (DSCOVR)

DSCOVR, originally built in the 1990s, was stored at NASA Goddard Flight Center until it was launched on February 11, 2015 from Cape Canaveral. The spacecraft is designed to monitor space weather and perform Earth observations from it's Lissajous orbit near L_1, which was reached at June 8, 2015. The spacecraft position is ideal to monitor the solar wind (providing a 15 to 60 minute warning before a solar storm

reaches Earth) and to observe phenomena on the Earth (e.g. dust, vegetation cover, climate) (Burt and Smith, 2012). The science instruments of DSCOVR are:

1. Solar Wind Plasma Sensor and Magnetometer (PlasMag),
2. National Institute of Standards and Technology Advanced Radiometer (NISTAR),
3. Earth Polychromatic Imaging Camera (EPIC),
4. Electron Spectrometer (ES),
5. Pulse Height Analyzer (PHA)

Solar Wind Plasma Sensor and Magnetometer (PlasMag)

PlasMag measures the solar wind parameters which are used for space weather predictions and also for accurate warnings of geomagnetic storms with lead times of up to one hour. PlasMag consists of a flux-gate vector magnetometer measuring the IMF, a Faraday Cup solar wind positive ion detector, and electron electrostatic analyzer to measure the three-dimensional velocity distribution of the solar wind electrons, protons, and alpha particles with high time resolution. Data provided by the magnetometer, the Faraday Cup, and the electron electrostatic analyzer allows us to investigate solar wind waves and gives insight into basic plasma properties (NOAA Satellite and Information Service, 2018).

3.3. Solar TErrestrial RElations Observatory (STEREO)

STEREO is a solar observation mission from NASA, launched on October 25, 2006, with the purpose to understand the origin and consequences of CMEs and to follow the propagation of CMEs through the inner heliosphere. STEREO measurements are used to study the mechanisms and sites of energetic particle acceleration and to develop three-dimensional models of the solar wind between Sun and Earth. The twin spacecraft are sent into an Earth-like heliocentric orbit of nearly 1 AU. STEREO-B(ehind) is in a slightly larger orbit than Earth causing the spacecraft to trail Earth. STEREO-A(head) on the other hand was put in a slightly closer heliocentric orbit making the spacecraft orbit the Sun faster than Earth. Hence, over the time the spacecraft separate approximately 44° per year as seen from the Sun. With an additional spacecraft in L_1 and a separation angle of 120° between the spacecraft, a 360° view of the Sun is possible (Kaiser et al., 2008). Both STEREO spacecraft have mounted the following instruments:

1. Sun Earth Connection Coronal and Heliospheric Investigation (SECCHI),
2. In-situ Measurements of Particles and CME Transients (IMPACT),
3. PLasma And Suprathermal Ion Composition (PLASTIC),
4. STEREO/WAVES (SWAVES).

In-situ Measurements of Particles and CME Transients (IMPACT)

IMPACT consists of seven different sensors and focuses on the solar energetic particle (SIT, SEPT, LET, HET), solar wind and suprathermal electron (STE, SWEA), and magnetic field measurements (MAG) needed to address STEREO's goals (Luhmann et al., 2005).

PLAsma and SupraThermal Ion Composition (PLASTIC)

PLASTIC is designed to study the in-situ bulk properties of the solar wind. The instrument is a mass spectrometer, with a nearly complete angular coverage, which measures the elemental composition, ionic charge states, and bulk flow parameters of major solar wind protons, alpha particles and ions (Galvin et al., 2008).

Sun Earth Connection Coronal and Heliospheric Investigation (SECCHI)

SECCHI is a suite of remote sensing instruments on the two STEREO spacecraft. It obtains full Sun EUV images of the chromosphere (EUVI), images of the corona and the inner heliosphere (COR1, COR2), and white light images (HI-1, HI-2). The detectors of EUVI are 2048 x 2048 pixel CCD with a field-of-view out to 1.7 $R_{\odot}$, which observe in four spectral channels spanning from 0.1 to 20 MK. SECCHI's purpose is to study the three-dimensional evolution of CMEs through the full journey from the Sun to Earth (Howard et al., 2002; Wuelser et al., 2004).

3.4. Solar Dynamics Observatory (SDO)

SDO was sent into a circular geosynchronous Earth orbit with an altitude of 35789 km, on February 11, 2010. It is the first part of NASA's Living With a Star (LWS) program to study the solar variability and its impacts on Earth. SDO's main goal is to observe and understand the solar dynamics, with special attention on solar flares, CMEs and the solar wind. The ultimate goal is to develop the ability to forecast space weather and it's influences on life on Earth (Pesnell et al., 2012). SDO includes three instruments:

1. The Helioseismic and Magnetic Imager (HMI) which is designed to measure the full-disk vector magnetic field, continuum and Doppler shift at the photosphere of the Sun using the 6173 Å Fe I absorption line (Schou et al., 2012).
2. The Extreme Ultraviolet Variability Experiment (EVE) measures fluctuations in the Sun's ultraviolet output in several wavelength bands (Woods et al., 2012).
3. The Atmospheric Imaging Assembly (AIA) is an array of four telescopes that observes the surface and atmosphere of the Sun (Lemen et al., 2012).

Atmospheric Imaging Assembly (AIA)

AIA is an array of four telescopes that observes the surface and atmosphere of the Sun. It provides multiple simultaneous high-resolution full-disk images of the corona and the transition region up to 0.5 $R_\odot$ above the limb. AIA provides narrow-band images of seven extreme ultraviolet (EUV) band passes centered on specific lines:

- 94 Å (Fe XVIII) to study the flaring corona,
- 131 Å (Fe VIII, XXI) for the transition region and the flaring corona,
- 171 Å (Fe IX) for the quiet corona and the transition region,
- 193 Å (Fe XII, XXIV) for the corona and hot flare plasma,
- 211 Å (Fe XIV) for active region corona,
- 304 Å (He II) for the chromosphere and the transition region,
- and 335 Å (Fe XVI) to study the active region corona.

The temperature range captured by AIA lies between $6 \cdot 10^4$ K and $2 \cdot 10^7$ K. AIA is also equipped with a telescope that takes continuum images enabling the coalignment with images from other spacecraft (Lemen et al., 2012).

3.5. Solar and Heliospheric Observatory (SoHO)

The Solar and Heliospheric Observatory (SoHO), launched on December 2, 1995 and sent in a Lissajous orbit near L_1, was developed in collaboration of ESA and NASA. SOHO has three principal areas of scientific investigation: (i) Probing the solar interior using helioseismology, (ii) determining the heat mechanism of the solar corona, and (iii) studying the solar wind and its acceleration process (Domingo et al., 1995). The instruments according to the principal areas:

1. **Helioseismology:** Global Oscillations at Low Frequencies (GOLF), Variability of solar IRradiance and Gravity Oscillations (VIRGO), Michelson Doppler Imager (MDI)
2. **Solar atmosphere remote sensing:** Solar Ultraviolet Measurement of Emitted Radiation (SUMER), Coronal Diagnostic Spectrometer (CDS), Extreme ultraviolet Imaging Telescope (EIT), UltraViolet Coronagraph Spectrometer (UVCS), Large Angle and Spectrometric Coronagraph (LASCO), Solar Wind Anisotropies (SWAN)
3. **Solar wind "in-situ":** Charge Element and Isotope Analysis System (CELIAS), Comprehensive SupraThermal and Energetic Particle analyser collaboration (COSTEP), Energetic and Relativistic Nuclei and Electron experiment (ERNE)

Extreme ultraviolet Imaging Telescope (EIT)

EIT provides full-disk images which are used to study the evolution of chromospheric and coronal structures. A Ritchey-Chrétien telescope obtains images of the solar atmosphere in four selected bandpasses in the EUV:

- 171 Å (Fe IX-X) to study the corona/transition region boundary,
- 195 Å (Fe XII) for the quiet corona outside CHs,
- 284 Å (Fe XV) for active regions,
- and 304 Å (H II) to study the chromospheric network and CHs.

The temperature range of the solar structures that can be measured reaches from $6 \cdot 10^4$ K and $3 \cdot 10^6$ K (Delaboudinière et al., 1995).

4. Data and Methods

The data set covered in this study spans from January 2008 to December 2012. The time range includes the minimum phase of solar cycle 23 (low solar activity) and the increase to the maximum phase of solar cycle 24 (high solar activity). The main reason for selecting this period of time was the position of the STEREO-B spacecraft. In January 2008 STEREO-B was azimuthally behind Earth with an separation angle of roughly 22° which increased to approximately 130° in December 2012 . In Figure 4.1 the separation of STEREO-B over time with respect to Earth can be seen. It also shows the position of Earth (green point) and STEREO-A (red point) in December 2012. When having a close look, also the slightly different orbits compared to Earth can be seen. STEREO-B is located further out than Earth, resulting in slightly slower orbit. STEREO-A, on the other hand, orbits closer to the Sun, which makes the orbital motion faster compared to Earth. As a consequence, the two STEREO spacecraft separate from Earth. In fall 2009 the separation angle of STEREO-B was roughly 60°, making it perfect to explore a possible L_5 mission.

To get the Earth view in-situ measurements, the *SolarSoft* SSC_get_winddata was used. It returns the SWEPAM and MAG data from ACE, combined with the equivalent data from DSCOVR/PlasMag in a 1 minute temporal cadence. Before the analysis, the in-situ measurements as well as the model results were linearly interpolated onto a 6 hour time grid.

4.1. Verification of the Solar Wind Parameters

In order to compare the solar wind parameters obtained by the different models we focus on two approaches. First continuous variables, which can take on any real value, and second binary variables that are restricted to two possible values such as yes/no or event/no event. The latter are capable to match special events in the solar wind by comparing observational data and forecast. When studying the background solar wind it is of particular interest to have an estimate of the average error of the predicted wind parameters (forecast) and the measured solar wind parameter (observation). On the other hand, we also want to know if the model is able to predict, e.g. enhanced solar wind speed (HSS), which is called event-based verification. It should be noted, that CMEs cause transient peaks in the in-situ measured solar wind. Hence, at times of CMEs it is expected that empirical models (described in Section 5.1) are not able to predict these transient peaks. As a consequence we make two separate analyses where we include and exclude CMEs according to the lists of Richardson & Cane for ACE (194 CMEs for 2008–2012; see Richardson and Cane 2010 for a description of the

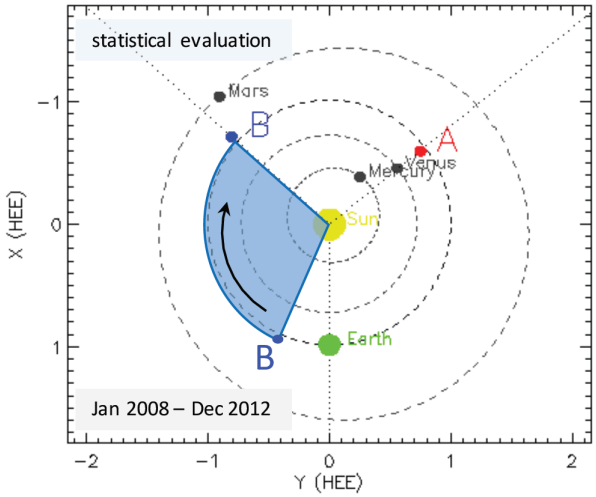

Figure 4.1.: Positions of the STEREO spacecraft (A in red, B in blue) and Earth position (in green). STEREO-B separates from ∼22° in January 2008 to ∼130° in December 2012, indicated by the blue area. From Temmer et al. (2018).

catalog) and for STEREO-B from L. Jian (189 CMEs for 2008–2012; see Jian et al. 2006 for a description of the catalog). When excluding the times of CMEs, not only the peaks are rejected, but these times are also not considered when calculating the continuous variables. The definitions of the continuous variables and the event-based verification follow the work of Reiss et al. (2016).

4.1.1. Continuous Variables

To get an first impression of the predicted parameters and the observed values it is reasonable to calculate the arithmetic mean of the individual time series. It is given by:

$$mean = \frac{1}{n}\sum_{i=1}^{n} x_i \tag{4.1}$$

and is the most commonly used and readily understood measure of central tendency. Another important error measure is the mean error (ME) which is a measure for forecast accuracy:

$$ME = \frac{1}{n}\sum_{i=1}^{n}(f_i - o_i) = \bar{f}_i - \bar{o}_i, \tag{4.2}$$

where f_i is the ith element of the forecast and o_i is the ith element of the observation. It is given by the difference of the average of the forecast and the average of the observation and usually refers to the average of all the errors. An "error" is in this context the difference in the predicted and the observed value. The next measure

used in this study is the mean absolute error:

$$MAE = \frac{1}{n}\sum_{i=1}^{n} \mid f_i - o_i \mid . \tag{4.3}$$

It uses absolute values of errors in the forecast and the observations, resulting in an average error. MAE is the average vertical distance between each point and the Y=X line and is the arithmetic mean of the absolute differences between the forecast and the observation pairs. The last measure used is the root-mean-square error:

$$RMSE = \sqrt{\frac{1}{n}\sum_{i=1}^{n}(f - o_i)^2}. \tag{4.4}$$

It is a frequently used measure of the differences between values predicted by a model and the values actually observed. The $RMSE$ represents the sample standard deviation of the differences between prediction and observation. In any case where the observation is equal to the forecast the ME, MAE, and $RMSE$ are consequently zero. The error measures increase as the forecast deviates more and more from the observation. The continuous variables are useful when one is interested in the average error of the forecast and the observation (Reiss et al., 2016).

4.1.2. Event-based Verification

In comparison to continuous variables, the binary variables only have two possible values. The problem with having just a single number is that there are circumstances where point-by-point time series comparing techniques (i.e. MAE) can be misleading. This happens if peaks in the predicted time series (i.e. enhanced solar wind speed) are generally well modeled but the arrival time is slightly different in the observations (Owens et al., 2005). The event-based verification was already utilized in several studies (e.g., Owens et al. 2005; MacNeice 2009; Reiss et al. 2016). This technique has three important steps (see Reiss et al. 2016):

1. Definition and detection of an event in forecast and observations.
2. Association of the detected events in forecast and observations.
3. Computation of quantitative measures to compare model results.

In this study a "peak event" is found if the minimum solar wind speed reaches at least 400 km/s before and after the decrease and has a peak prominence of at least 60 km/s (see Reiss et al. 2016). In addition to the peaks, we are also interested in how well the base level of the modeled solar wind matches the observations. For the "base level", i.e. the low solar wind speed, we set a threshold of 400 km/s according to Schwenn (2006b). To obtain the timing and the solar wind speed, first the minima in the time series is detected. Second, all the values around the minima, which lie below the threshold, are taken into account. Third, the mean of the velocities and the mean of the times of the values below the threshold are calculated, giving only

Table 4.1.: Contingency table for predicted and observed events. From Woodcock (1976).

Predicted	Observed: Event	No Event
Event	True Positive (TP)	False Positive (FP)
No Event	False Negative (FN)	True Negative (TN)

one mean velocity at a certain time for the whole base level surrounding a minimum. To be considered as a base level, the solar wind has to stay below the threshold for at least two days. Is a CME occurring during the time when a base level is detected, this base level is split into two separate base levels. Again, the condition that the two individual base levels have to last at least for two days must be fulfilled. Once the events ("peak", "base level") have been detected in the forecast and the observations, they can be associated to each other. A "hit" is defined if a predicted event overlaps within a time window of ± 2 days with a detected event in the observations. A "false alarm" is given when an event is predicted but not detected, whereas a "miss" is a detected event which has no predicted event associated (for a detailed description see Reiss et al., 2016). The event association is performed in such a way that always the closest events are associated even though multiple associations are possible.

Contingency tables (also called crosstabs or two-way tables) are used in statistics to summarize the relationship between several categorical variables. In this case the categorical variables are the events in the predicted and the observed time series. Table 4.1 contains the number of "hits" (True Positives), "false alarms" (False Positives), "misses" (False Negatives), and correct rejections (True Negatives). In this study we are interested in the events and therefore ignore the True Negatives which is the number of no event is predicted and no event is observed. Based on the contingency table the following measures can be derived (Woodcock, 1976):

$$\mathsf{Probability\,Of\,Detection\,(POD)} = \frac{\mathsf{TP}}{\mathsf{TP+FP}} \tag{4.5}$$

$$\mathsf{False\,Alarm\,Ratio\,(FAR)} = \frac{\mathsf{FP}}{\mathsf{TP+FP}} \tag{4.6}$$

$$\mathsf{Threat\,Score\,(TS)} = \frac{\mathsf{TP}}{\mathsf{TP+FP+FN}} \tag{4.7}$$

$$\mathsf{Bias\,(BS)} = \frac{\mathsf{TP+FP}}{\mathsf{TP+FN}} \tag{4.8}$$

The Threat Score (TS), a measure of the overall model performance, and the POD range from 0.0 to 1.0, where the model performs best when they are 1.0 and worst having a value of 0.0. On the other hand, a model is considered best when the false alarm ratio (FAR) is 0.0 (again ranging from 0.0 to 1.0). The Bias (BS) does not provide any quantification of the correspondence between the prediction and

the observation, but indicates whether the number of observations is underestimated (BS < 1) or overestimated (BS > 1). In addition, we also calculate for each "hit", if the solar wind parameter is either over or underestimated and give the Ratio of Underestimated Speed (RUS), where $1-$RUS gives the ratio of overestimation. Also the mean and standard deviation of time difference (dt) and the speed difference (dv) of the hits are calculated.

5. Solar Wind Forecast Models

In this chapter the different solar wind forecast models are presented. The empirical models, Persistence model 27d, Persistence model STEREO and Persistence model STEREO+CH, are based on in-situ measurements and remote sensing data and utilize multi-viewpoint satellite data. The numerical forecast models ENLIL and EUHFORIA make use of a semi-empirical model for the inner boundary, based on a single-viewpoint magnetogram, and then solve MHD equations to model the solar wind conditions in the heliosphere. In contrast to measurements of the solar wind parameters, which are only available for a few points in the heliosphere, numerical models provide three-dimensional solar wind information of the heliosphere.

5.1. Empirical Forecast Models

5.1.1. Persistence model 27d

It has been shown that not only CMEs are responsible for geomagnetic storms on Earth, but also the ambient solar wind can be geoeffective in its own. Geomagnetic storms can also happen when HSS interact with the relatively slow solar wind, where a compression region forms (e.g., Richardson et al. 2002). The ambient solar wind evolves slowly over the course of several Carrington rotations. In times of the solar minimum or in the decline phase of a solar cycle co-rotating interaction region (CIR, e.g. Gosling and Pizzo 1999) can be formed. As a consequence, the pattern of the solar wind measured in-situ, for instance by ACE at L_1, repeats approximately every synodic solar rotation, roughly every 27.27 days. Hence, the solar wind conditions can be predicted with a 27 day lead time when assuming that the conditions for the upcoming period will be identical to those observed at the current time (Owens et al., 2013). The in-situ measurements for the Persistence model 27d were obtained by the ACE spacecraft and shifted by 27.27 days to get a forecast.

5.1.2. Persistence model STEREO

The quality of the performance of the Persistence model 27d, described in the previous section, is not constant over time (Owens et al., 2013). During times of low solar activity, this model gives best results, because CMEs are less frequent and coronal features, which alter the solar wind one synodic period later, are less dynamic (e.g., McComas et al., 2003; Yashiro et al., 2004). The advantage of the Persistence model

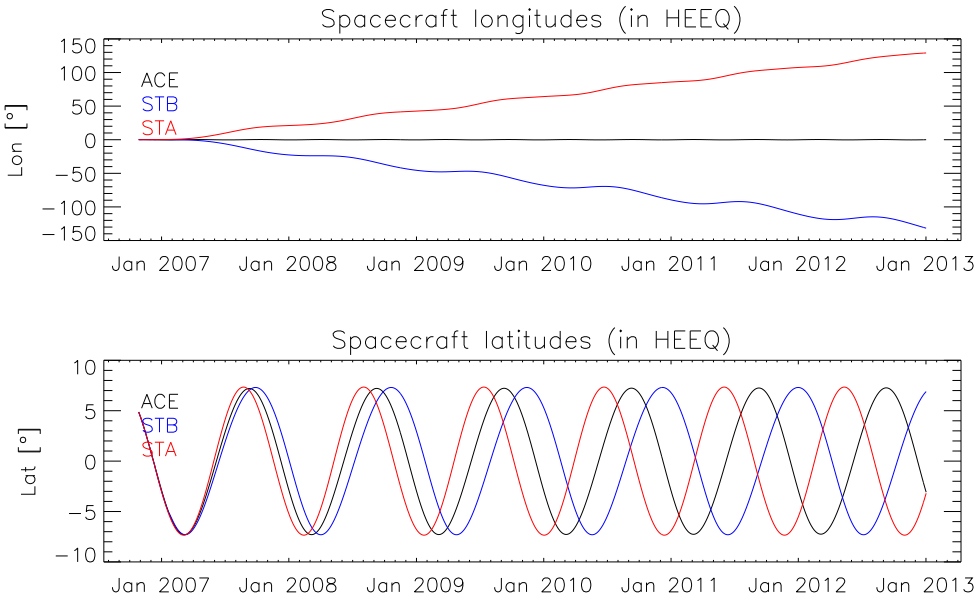

Figure 5.1.: Longitude (top panel) and latitude (bottom panel) for ACE (black), STEREO-B (blue), and STEREO-A (red) spacecraft in HEEQ coordinate system.

27d is the lead time, with the shortcoming that any disturbance within these 27 days leads to a poor forecast.

Another approach to predict the solar wind conditions is to measure the solar wind parameters at different longitudes in interplanetary space. This means that the lead time of the forecast depends on the heliographic longitudinal separation between the two positions of the measurements, i.e. the spacecraft positions. Such spacecraft predestined for this purpose are the STEREO spacecraft, since they show varying longitudinal separation from Earth with time (∼22° per year). This can be seen in Figure 5.1 where the longitude and latitude of ACE (black), STEREO-B (blue), and STEREO-A (red) are given in Heliocentric Earth Equatorial (HEEQ[4]). In this coordinate system the Z-coordinate is the solar rotation axis and the X-coordinate is given by the intersection of solar equator and solar central meridian as seen from Earth. In January 2008 STEREO-B was azimuthally behind Earth with an separation angle of roughly 22° and in December 2012 the separation angle was approximately 130°. Therefore, over time the forecast lead time increased from about 1.5 days in 2008 to about 10 days in 2012. The drawback of longer lead times is that the solar wind may evolve in the meantime which is very likely related to a decrease in the forecast performance. One has also to keep in mind, that the STEREO spacecraft show an periodic variation in heliographic latitude compared to ACE (see bottom panel Figure 5.1). This is due to the tilt of the solar rotation axis with respect to the ecliptic. Hence, the two spacecraft may measure different solar wind streams, having an effect on the forecast performance (Gómez-Herrero

[4] https://stereo-ssc.nascom.nasa.gov/coordinates_explanation.shtml [March 15, 2018]

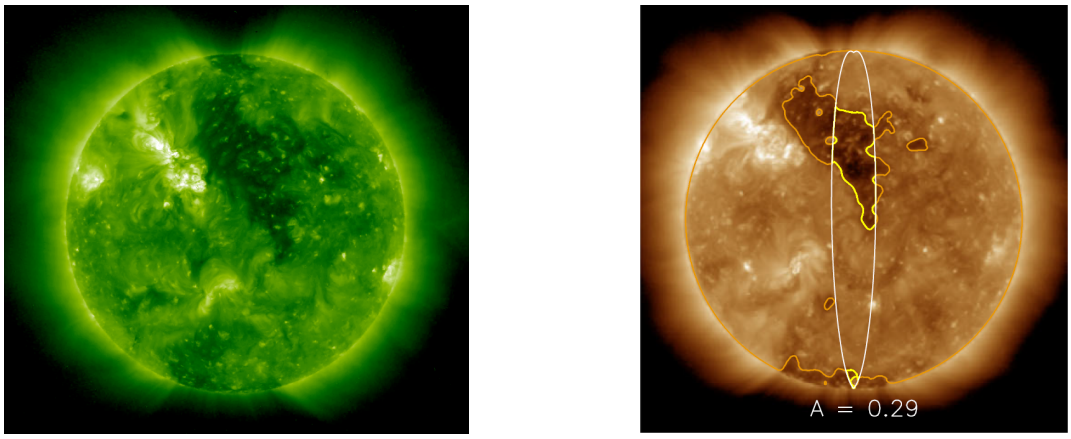

Figure 5.2.: Left: STEREO-B/SECCHI/EUVI 195 Å image on February 22, 2011. A CH can be seen in the northern hemisphere. From JHelioviewer[6]. Right: SDO/AIA 193 Å image on February 28, 2011, with the same CH observed 6 days later. The white lines indicate the considered meridional slice (±7.5° around the central meridian) and the yellow lines mark the CH within the meridional slice. In this example the CHs cover 29% of the fractional area. From Rotter et al. (2015).

et al., 2011; Kohutova et al., 2016). An advantage of a persistence model based on STEREO in-situ measurements lies in a better overall forecast performance, since the time (according to the spacecraft positions) during which the solar wind conditions have to be stable reduces. On the other hand the lead time of the forecast decreases. The STEREO in-situ bulk properties of the solar wind were obtained by PLASTIC and the magnetic field data by IMPACT. The STEREO level 2 data was downloaded from the UCLA[5] interface with a temporal cadence of 1 minute. The time series was then shifted in time according to the separation angle of STEREO-B and Earth.

5.1.3. Persistence model STEREO+CH

An even more sophisticated approach to forecast the solar wind parameters is to take the conditions on the solar surface into account. Especially the size of CHs, emanating the fast solar wind, is decisive. Vršnak et al. (2007) found a high degree of correlation between the area of CH and the solar wind speed with a time-lag of about 3–4 days. This corresponds to the time the solar wind needs to travel from Sun to 1 AU. Gómez-Herrero et al. (2011) showed that an expansion of a CH results in an increase in the solar wind speed. Based on that, Temmer et al. (2018) developed the

[5] http://aten.igpp.ucla.edu/forms/stereo/level2_plasma_and_magnetic_field.html

Persistence model STEREO+CH which uses EUV data from different viewpoints to assess the evolution of a CH and adjusts the speed measured by STEREO accordingly. The evolution is tackled by comparing the fractional areas of the CHs in EUV data from STEREO and EUV data from Earth view. Since the solar surface features are related to a solar wind speed that is measured 4 days later, also the lead time of the Persistence model STEREO+CH is limited to 4 days.

For this model an extraction technique of the fractional areas, which has already been applied in the empirical solar wind forecast (ESWF[7]) model, is applied. The CHs are detected using a histogram-based segmentation method where the fractional area is given by $\pm 7.5°$ around the central meridian (for a detailed description see Rotter et al. 2012 and Reiss et al. 2016). The left panel in Figure 5.2 shows an EUVI 195 Å image obtained by STEREO-B on February 22, 2011. The dark area in the northern hemisphere is the CH. The right panel shows the same CH about six days later but this time observed by SDO/AIA in the 193 Å wavelength. The boarders of the CH are given by the orange line. The white lines indicate the considered meridional slice and the yellow lines mark the CH within the meridional slice. In this example the CH covers 29% of the fractional area. The same method is also applied to the STEREO-B images. The fractional areas from STEREO and ACE observations are then related to each other. One can then define a "CH evolution ratio" r_{CH} which is given by:

$$r_{CH} = \frac{A_{ST}}{(A_{Earth} + A_{ST})}, \tag{5.1}$$

where A_{ST} is the fractional CH area derived from STEREO and A_{Earth} is the fractional CH area derived from Earth view (Temmer et al., 2018). A cutoff for the CH evolution ratio of $A < 0.02$ is used to suppress small variations of the CH. In addition, the median of the CH evolution ratio, $r_{CH_{med}}$, is calculated. r_{CH} of 0.5 means that the fractional area of the CH is still the same from Earth view as it was observed from STEREO. A growth of the fractional area is given when $r_{CH} < 0.5$ whereas $r_{CH} > 0.5$ means that the CH fractional area decreased. It is assumed that the predicted solar wind speed is underestimated in cases of expanding CHs. To account for that, the solar wind bulk velocity measured by STEREO is used and modified accordingly.

For the year 2008 it is expected, that the evolution of the CH occurs slowly since the separation angle of STEREO-B and ACE is small and the solar activity is low. To take the change in separation angle and the solar activity into account the coronal evolution ratio $r_{CH_{med}}$ is calculated for each year from 2008 to 2012. $r_{CH_{med}}$ increases from 2008 to 2012 indicating that CHs are rather decaying than expanding. A detailed description can be found in Section 3 in Temmer et al. (2018).

When comparing the difference in solar wind speed measured at ACE and STEREO-B ($v = v_{ACE} - v_{STEREO}$) to the CH evolution ratio (r_{CH}) one finds that the expanding

[6]https://helioviewer.org/ [March 15, 2018]
[7]http://swe.uni-graz.at/index.php/services/solar-wind-forecast

CHs show a weak trend of increasing solar wind speed. On the other hand, no trend can be found for decaying CHs that are related to solar wind speed decrease (see Figure 3 in Temmer et al., 2018). In order to have a robust measure three different persistence levels, based on the mean absolute deviation (MAD), are defined:

1. High persistence: $r_{CH_{med}} - 0.7 r_{CH_{MAD}} \leq r_{CH} < r_{CH_{MAD}}$
2. Medium persistence: $r_{CH_{med}} - 1.4 r_{CH_{MAD}} \leq r_{CH} < r_{CH_{med}} - 0.7 r_{CH_{MAD}}$
3. Low persistence: $r_{CH_{med}} - 1.4 r_{CH_{MAD}} \leq r_{CH}$

High persistence means that the fractional area is more or less constant and low persistence corresponds to a large change in the CH fraction area. According to the persistence levels, the measured solar wind speed at STEREO is increased by $+0.5 v_{MAD}$ for high persistence, $+1.0 v_{MAD}$ for medium persistence, and $+1.5 v_{MAD}$ for low persistence. These are the default values and correspond to the values used in the study of Temmer et al. (2018). The uncertainties represent an upper limit of the predicted solar wind speed, therefore the arithmetic mean between the increased speed and the original STEREO wind speed is calculated. No clear trend was found for decaying CHs to be associated with a decrease in solar wind speed. Hence, the measured speed at STEREO is not changed for times when $r_{CH_{med}} < r_{CH}$. In Section 6, the results with the default values, but also the results with different values defining the persistence levels are shown which is done to give an estimate how different definitions of the persistence levels effect the results. At times of data gaps in the EUV data, simply the original STEREO solar wind speed was used. This leads finally to a solar wind speed forecast that is updated with information of the evolution of the CH. Figure 4 and 5 in Temmer et al. (2018) show the solar wind speed derived using the Persistence model STEREO+CH for the years 2008 and 2012, respectively.

The EUV data needed to derive the fractional area of a CH was obtained by STEREO/SECCHI/EUVI and for the Earth view by SoHO/EIT or SDO/AIA. Here the 1024x1024 full-disk data in the 195 Å band (from STEREO/SECCHI/EUVI, 1 hour temporal cadence), the 195 Å band (from SoHO/EIT for 2008–2010, 6 hours temporal cadence), and the 193 Å band (from SDO/AIA for 2010–2012, 6 hours temporal cadence) was utilized. CHs are detected using a histogram-based segmentation method (e.g., Krista and Gallagher 2009; Rotter et al. 2012) and applying a threshold value of

$$TH = f \times (\text{median on-disk intensity}) \tag{5.2}$$

for areas within 60° heliospheric latitude and longitude. The factor f was adjusted to the corresponding instruments for STEREO $f = 0.32$, for AIA $f = 0.35$, and for EIT $f = 0.47$ (Temmer et al., 2018). Regarding areas beyond 60° and additional multiplication factor of 1.6 is applied, since the CHs appear less dark on the limb (Reiss et al., 2016). The measured solar wind speed by STEREO-B was then adjusted according to the persistence levels mentioned above.

5.2. Numerical Forecast Models

5.2.1. EUropean Heliospheric FORecasting Information Asset (EUHFORIA)

EUHFORIA (EUropean Heliospheric FORecasting Information Asset) is a new physics-based forecasting-targeted inner heliosphere model within the CCSOM[8] (Constraining CMEs and Shocks by Observations and Modelling) project. It is designed in particular for space weather forecasting purposes and is still in the process of development and fine tuning. EUHFORIA consists of a non-potential time-dependent model of the coronal magnetic field and a magnetohydrodynamic (MHD) heliosphere model with CMEs. This is done under the premise that at a certain distance (the boundary is set to $R_b = 1$ AU) the solar wind is supersonic and super-Alfvénic, meaning that no information is traveling towards the Sun. Due to the division in these two domains the heliosphere model is independent of the coronal model and makes it possible to use any available coronal model (Pomoell and Poedts, 2018). The coronal model used in this study is explained in the following.

Coronal domain:

This spatial domain of EUHFORIA extends from the photosphere or the low corona up to the heliocentric distance of $r = R_b = 0.1$ AU. The coronal model conditions are needed by the heliosphere model and should therefore provide realistic values for the MHD variables that represent the prevailing large-scale solar wind streams and the transient disturbances due to propagating CMEs. In EUHFORIA the solar wind model is based on semi-empirical relationships between topological properties of the coronal magnetic field and the measured solar wind parameters, since comparative studies (e.g., Owens et al. 2008; Gressl et al. 2014) have shown that this approach performs well compared to physics-based coronal models and need less computational effort. The empirical model used for EUHFORIA is based on the Wang-Sheeley (WS) model (Wang and Sheeley, 1990) the DCHB model (Riley et al., 2001) as well as the Wang-Sheeley-Arge (WSA) model (Arge et al., 2003). Also the magnetic field model consists of two parts: The magnetic field in the lower corona ($r \in [R_\odot, R_i]$) is given by the Potential Field Source Surface (PFSS) model (Altschuler and Newkirk, 1969). It is assumed to be current-free and is set to be purely radial at a given source surface radius $R_{SS} \geq R_i$. In the upper corona ($r \in [R_i, R_b]$) the magnetic field is given by the Schatten Current Sheet (SCS) model (Schatten et al., 1969). The SCS model is used to extend the magnetic field in a nearly radial fashion but retaining a thin layer for the heliospheric current sheet. R_i and R_{SS} are set to 2.3 $R_\odot$ and 2.6 $R_\odot$, respectively, otherwise the magnetic field lines would not make a smooth transition at the boundary of the two models. Once the three-dimensional magnetic field is determined, the large-scale topology of the coronal magnetic field is characterized and regions in the low corona that are open to the solar wind (i.e. CHs)

[8] http://sidc.be/ccsom/

are located. The ambient solar wind is determined empirically and characterizes the plasma parameters at the boundary (0.1 AU) for the heliospheric MHD model. The hourly updated standard synoptic magnetograms required by the PFSS are provided by the Global Oscillation Network Group (GONG) (Pomoell and Poedts, 2018).

Inner heliosphere domain:

The inner heliosphere model starts from $R_b = 0.1$ AU going outwards and consists of a MHD simulation. This three-dimensional time-dependent simulation self-consistently models the propagation, evolution and interaction of the solar wind streams and CMEs. Solved are the equations of the ideal MHD with an additional gravity term in the HEEQ coordinate system:

$$\frac{\partial \rho}{\partial t} = -\nabla \cdot (\rho \mathbf{v}) \tag{5.3}$$

$$\frac{\partial (\rho \mathbf{v})}{\partial t} = -\nabla \cdot \left[\rho \mathbf{v}\mathbf{v} + \left(P + \frac{B^2}{2\mu_0} \right) I - \frac{1}{\mu_0} \mathbf{B}\mathbf{B} \right] + \rho \mathbf{g} \tag{5.4}$$

$$\frac{\partial \mathbf{B}}{\partial t} = \nabla \times (\mathbf{v} \times \mathbf{B}) \tag{5.5}$$

$$\frac{\partial E}{\partial t} = -\nabla \cdot \left[\left(E + P - \frac{B^2}{2\mu_0} \right) \mathbf{v} + \frac{1}{\mu_0} \mathbf{B} \times (\mathbf{v} \times \mathbf{B}) \right] + \rho \mathbf{v} \cdot \mathbf{g} \tag{5.6}$$

where ρ, v, B, E, P, g are the mass density, velocity, magnetic field, total energy density, thermal pressure of the plasma, and gravitational acceleration, respectively. The total energy density is given by $E = \frac{P}{\gamma - 1} + \frac{1}{2}\rho v^2 + \frac{B^2}{2\mu_0}$, with the reduced polytropic index γ set to 1.5 (Pomoell and Poedts, 2018).

5.2.1.1. Obtaining an EUHFORIA time series

EUHFORIA provides model outputs from hourly updated standard synoptic GONG magnetograms from which daily model runs are performed. The simulated background solar wind at 1 AU distance range is then covering a time span of over 10 days ($-66°$ to $+66°$ in longitude, see gray slice in Figure 5.3a) with a temporal resolution of 10 minutes. The central region of the Sun is supposed to be based on magnetic field information having the least projection effects, and is therefore most reliable. Because of that, we developed a method to combine individual runs with the main information coming from the central region of the Sun. This is schematically drawn in Figure 5.3. The main focus lies in the central region around $0°$ with a range of ± 1 days (indicated by the black slices). When combining model outputs from consecutive days the individual curves overlap. In order to obtain a smooth time series, each curve is weighted (with a Gaussian distribution) with the central part receiving the strongest weight (see Figure 5.3b).

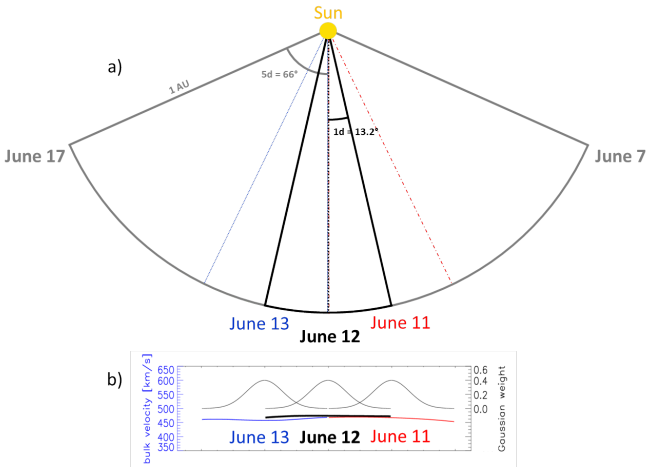

Figure 5.3.: Schematic representation of combining EUHFORIA model output for consecutive days. a) Different colors represent the selected range (±13.2° from the solar central region) for each day. Indicated in gray is the full range (±66°) provided by the model. b) Gaussian weight used for the model properties shown for three individual days.

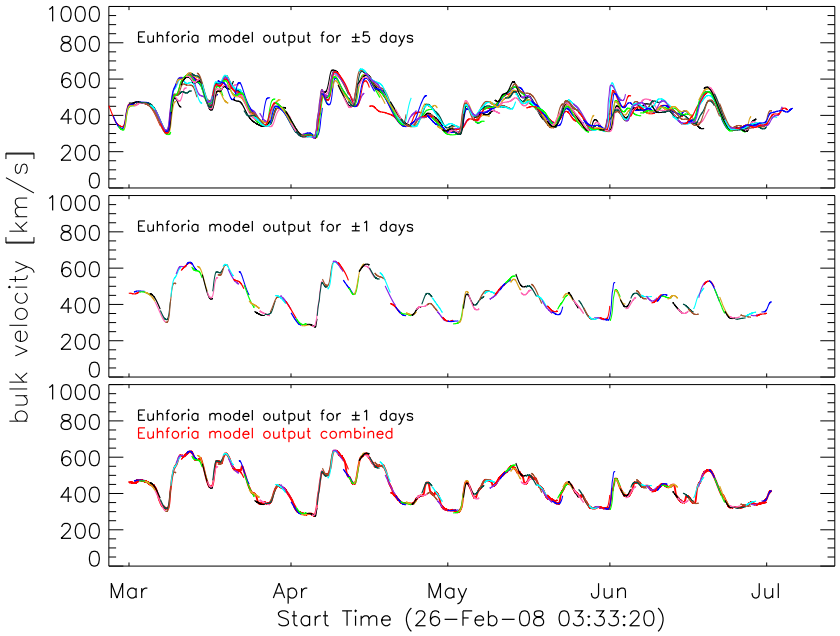

Figure 5.4.: Solar wind speed for March to June 2008. Top panel: Full EUHFORIA model output (±5 days). Middle panel: EUHFORIA model output limited to ±1 day. Bottom panel: Model output (different colors for each daily run) and resulting time series (thick red).

Exemplary we present how the method is applied. The top panel in Figure 5.4 shows the solar wind speed modeled by EUHFORIA for the full model output (±5 days). Different colors represent results for different days (i.e. individual magnetograms). As can be seen, the simulated solar wind speeds for consecutive days may show essential offsets. Therefore, the results are limited to ±1 day (middle panel in Figure 5.4) and combined using the Gaussian distribution as indicated in Figure 5.3b. The resulting time series can be seen in the bottom panel of Figure 5.4 indicated by the thick red curve.

Also other properties are used to determine the effect of the weighting on the obtained time series. The top panel in Figure 5.5 shows the EUHFORIA model output with the default settings of ±1 day and using the central region around 0° (identical to the red curve in the bottom panel of Figure 5.4). In the middle panel EUHFORIA outputs with other time ranges (from ±1 day to ± 5 days) and weightings (Gaussian and linear) are shown. It can be seen, that the curves with Gaussian weighting all show a similar trend and are qualitatively comparable. The time series gets smoother as the selected time range increases, hence small peaks are suppressed. The curve with the linear weighting (red curve in the bottom panel of Figure 5.5) is not smooth, since the jumps of the individual daily outputs are not smoothed by the Gaussian.

In a next test, we evaluate how the resulting time series for the simulated solar wind speed are affected when shifting the central region. With this we take into account that not the central region of the magnetogram but eastern or western regions influence the simulated solar wind more strongly. The bottom panel of Figure 5.5 shows EUHFORIA time series where the central region is shifted. The different colors represent different shifts, where −3 (light blue) means that the central region is shifted to 3 days before the magnetogram date (e.g. time of the magnetogram is June 15 then the central region is shifted to June 12 and the resulting individual curve is taken from June 11 to June 13). One can see in the bottom panel of Figure 5.5 that shifting the central region has more influence on the resulting time series than using a longer time range. Especially in mid-June the curves show essential differences. For the curve shown in cyan (0 GW) the same properties are used as for the time series shown in the top panel. In Section 6 we compare the EUHFORIA time series obtained with the default properties (time range ±1 day and central region around 0°) to in-situ measurements. In addition, EUHFORIA time series with other properties (different weighting and selected time range) are compared to in-situ measurements in order to determine the effect on the results.

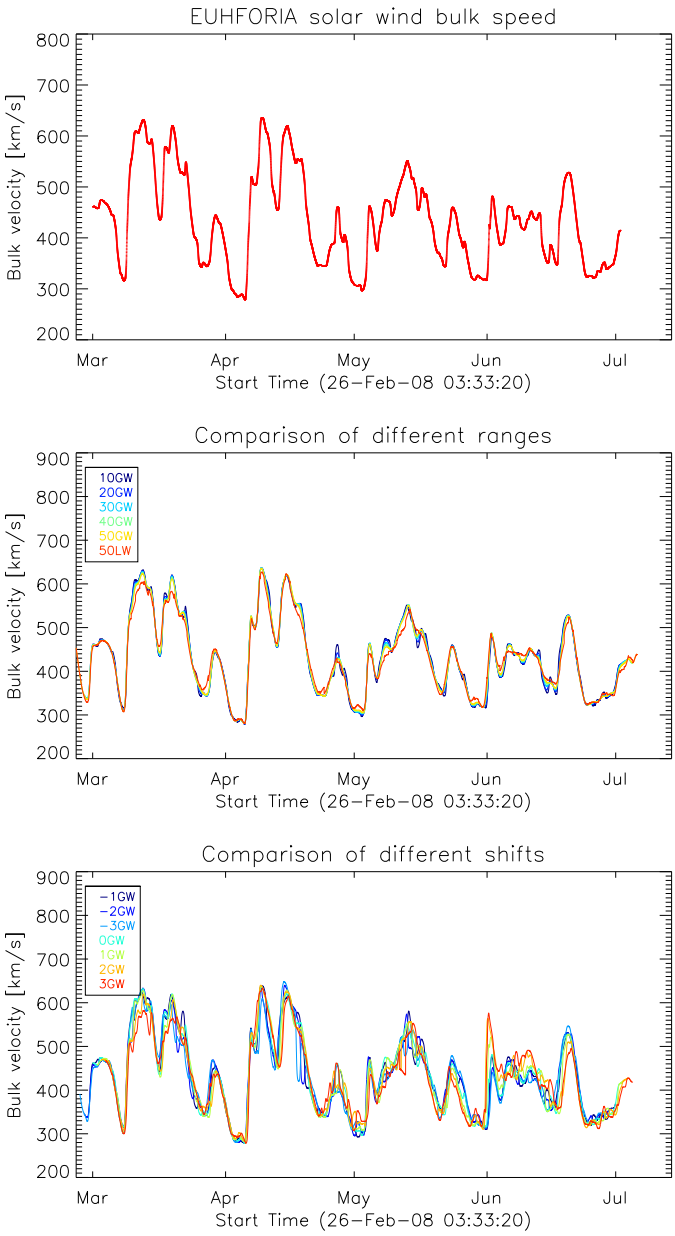

Figure 5.5.: Top panel: Time series obtained using a time range of the individual curves that is limited to ±1 day and a central region set to 0°. Middle panel: EUHFORIA time series with different selected time ranges. Dark purple: using a time range of ±1 day with Gaussian weighting (the same as the red curve in the top panel), Dark blue: time range ±2 days with Gaussian weighting, Light blue: ±3 days with Gaussian weighting, Green: time range ±4 days with Gaussian weighting, Yellow: time range ±5 days with Gaussian weighting, Red: time range ±5 days with linear weighting. Bottom panel: Comparison of the time series obtained by using a time range of ±1 day. The different colors represent time series where not the time of the magnetogram is given as the central part, but the central part is shifted by −3 days (light blue) to +3 days (red).

5.2.2. ENLIL Model of the Heliosphere

ENLIL is an already existing time-dependent three-dimensional MHD model, mainly developed by D. Odstrčil, to simulate the structure and the evolution of the solar wind (Odstrcil et al., 2002). Model runs can be requested online using the web page of the Community Coordinated Modeling Center (CCMS[9]). ENLIL uses an ideal fluid approximation and solves the MHD equations by using a Total Variation-Diminishing Lax-Friedrich (TVDLF) scheme (Tóth and Odstrčil, 1996) to numerically model the properties of the heliosphere. ENLIL neglects macroscopic processes and assumes equal densities and temperatures for the ions and electrons. The following parameters are used to describe the plasma:

- velocity,
- density,
- pressure,
- temperature,
- total energy density,
- magnetic field.

ENLIL provides simulations for the inner and middle heliosphere, reaching out up to 10 AU. To track the plasma and the interplanetary magnetic field polarity outwards, two continuity equations have to be solved in addition to the MHD equations (Odstrcil, 2003):

$$\frac{\partial}{\partial t}(\rho_c) + \nabla \cdot (\rho_c V) = 0, \tag{5.7}$$

$$\frac{\partial}{\partial t}(\rho_p) + \nabla \cdot (\rho_p V) = 0, \tag{5.8}$$

where V is the mean flow velocity, ρ_c, and ρ_p are the quantities for tracing the interplanetary magnetic field property and for tracing the injected mass, respectively. ENLIL can be coupled to either the Magnetohydrodynamics Around Sphere (MAS) model or the Wang-Sheeley-Arge (WSA) model. Those are coronal models and provide the inner boundary conditions for ENLIL, which then simulates the propagation of the solar wind outwards into the heliosphere.

The ENLIL model runs were performed at CCMC at the NASA Goddard Space Flight Center. On the one hand, ENLIL can be used to simulate transient disturbances in the heliosphere (CME interaction with the ambient solar wind) with the so-called ENLIL with cone model, but it can also be used to model the solar wind background. For this study, we utilize the solar wind background with the WSA coronal model to generate a stationary solar wind solution. The WSA model needs as input a synoptic line-of-sight magnetogram of the Sun. In our case they are provided by GONG as they are also used for EUHFORIA. The model runs were requested

[9]https://ccmc.gsfc.nasa.gov/

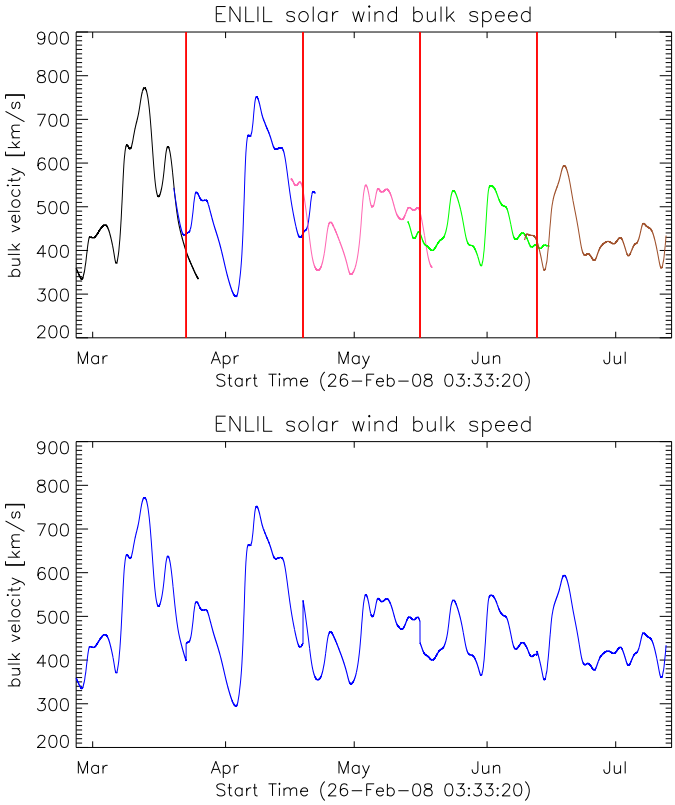

Figure 5.6.: Top panel: ENLIL solar wind bulk velocity for different Carrington rotations in different colors. The vertical red lines lie in the center of the overlap and indicate where the individual ENLIL runs are truncated. Bottom panel: Resulting time series for the solar wind bulk velocity of the individual ENLIL runs.

for 10 Carrington rotations (2067–2071 for the year 2008 and 2120–2124 for the year 2012), covering the same time range as EUHFORIA, using the ENLIL version 2.8 with a grid resolution of 256×30×90 and an outer boundary set to 2 AU. The obtained time series have a temporal resolution of about 6 minutes. It should be mentioned that the ENLIL runs using GONG are still in trial mode.

Figure 5.6 shows the solar wind bulk velocity modeled by ENLIL. Since the individual runs (top panel in Figure 5.6) show some overlap, we truncate the curves at the center of the overlap, indicated by the vertical red lines. The resulting solar wind speed can be found in the bottom panel of Figure 5.6. This may seem to be a very crude method to combine the individual runs. Regarding the times end of March and mid of June 2008, it may be appropriate since the individual runs are quite similar. For mid of April, however, the two consecutive runs seem to be shifted in time. As a result of this method a jump in the solar wind speed is produced, but still the peak is retained and the overall solar wind speed profile is represented in a reasonable manner.

Wang-Sheeley-Arge (WSA) Model of the Corona

The Wang-Sheeley-Arge (WSA) (Arge et al., 2003) model provides the input for the inner boundary of ENLIL. It uses an empirical relation that connects the expansion factor of flux tubes (compact regions of confined magnetic field) to solar wind velocities at 1 AU. Levine et al. (1977) found that HSS are correlated with the low magnetic flux tube expansions between the photosphere and the corona. WSA is based on a PFSS model of the steady state corona (Altschuler and Newkirk, 1969; Schatten et al., 1969). Carrington maps of the radial photospheric field are created by using photospheric magnetic field maps. These serve then as an input to the PFSS in order to determine the coronal field out to 2.5 $R_{\odot}$. The output of the PFSS is then used as input to the Schatten Current Sheet (SCS) (Schatten et al., 1969), giving more realistic results of the magnetic topology of the upper corona. The solar wind speed is then estimated by following an empirical relation (Owens et al., 2008):

$$V(f_s, \Theta_b) = 265 + \frac{1.5}{(1+f_s)^{1/3}} \left\{ 5.8 - 4.4 exp\left[1 - (\Theta_b / 7.5°)^3 \right] \right\}^{3.5} \text{km/s}, \qquad (5.9)$$

where f_s is the flux tube expansion factor and Θ_b is the minimum angular separation (at the photosphere) between an open field foot point and its nearest CH boundary. This model was further improved by Arge and Pizzo (2000) who included a correction of the input magnetic field maps and implemented a continuous empirical function for the relation of the flux tube expansion factor and the solar wind speed at Earth location.

6. Results

In this Chapter the comparison between different model results and the actual solar wind measurements are presented. First, a statistical study including 5 years (January 2008 to December 2012) verifying three empirical models (Persistence model 27d, Persistence model STEREO, Persistence model STEREO+CH) is presented. This is followed by the comparison of two numerical models (EUHFORIA and ENLIL) with in-situ measurements for four months (March to June) in 2008 and three months (March to May) in 2012. In this chapter only selected results of the different forecast models are shown. Hence, we added an Appendix A, where all the figures of the forecast models with different settings in comparison to the in-situ measurements can be found. Also the tables containing the continuous variables and the event-based statistics of all the models with different settings can be found in Appendix B.

6.1. Statistical results of the empirical models

Here we present the performance of the Persistence model 27d, Persistence model STEREO and Persistence model STEREO+CH in comparison to ACE in-situ measurements. We therefore use the event-based and the continuous forecast validation approach to obtain statistical results for the time range January 2008 to December 2012.

Figure 6.1 shows the Persistence model 27d (blue curve) with in-situ measurements obtained by ACE (orange curve) using the peak detection algorithm described in Section 4.1.2. This model uses as forecast the in-situ measurements of one prior Carrington rotation. Hence, also the times of CME occurrence (according to the list maintained by Richardson and Cane, 2010) are shifted by 27.27 days. The number of identified peaks in the speed profiles, together with the number of hits, false alarms, and misses are given in the plot legend. The black dots that are put below or above a hit (blue crosses), indicate whether the peak speed was under- or overestimated by the forecast. Since CMEs are transient events, times of CME occurrences are excluded in this figure. In addition we want to asses the model performance for the base levels of the solar wind as described in Section 4.1.2. Figure 6.2 shows the detected base levels for the Persistence model 27d. The figures where the times of CMEs are not excluded can be found in the Appendix A (Figure A.1 and Figure A.2).

The event-based verification applied to the peak and base level detection for ACE in-situ measurements and Persistence model STEREO can be seen in Figure 6.3 and Figure 6.4. The green vertical bars represent times of CME occurrence at STEREO-B according to the catalog of L. Jian (for a description of the catalog see Jian et al.,

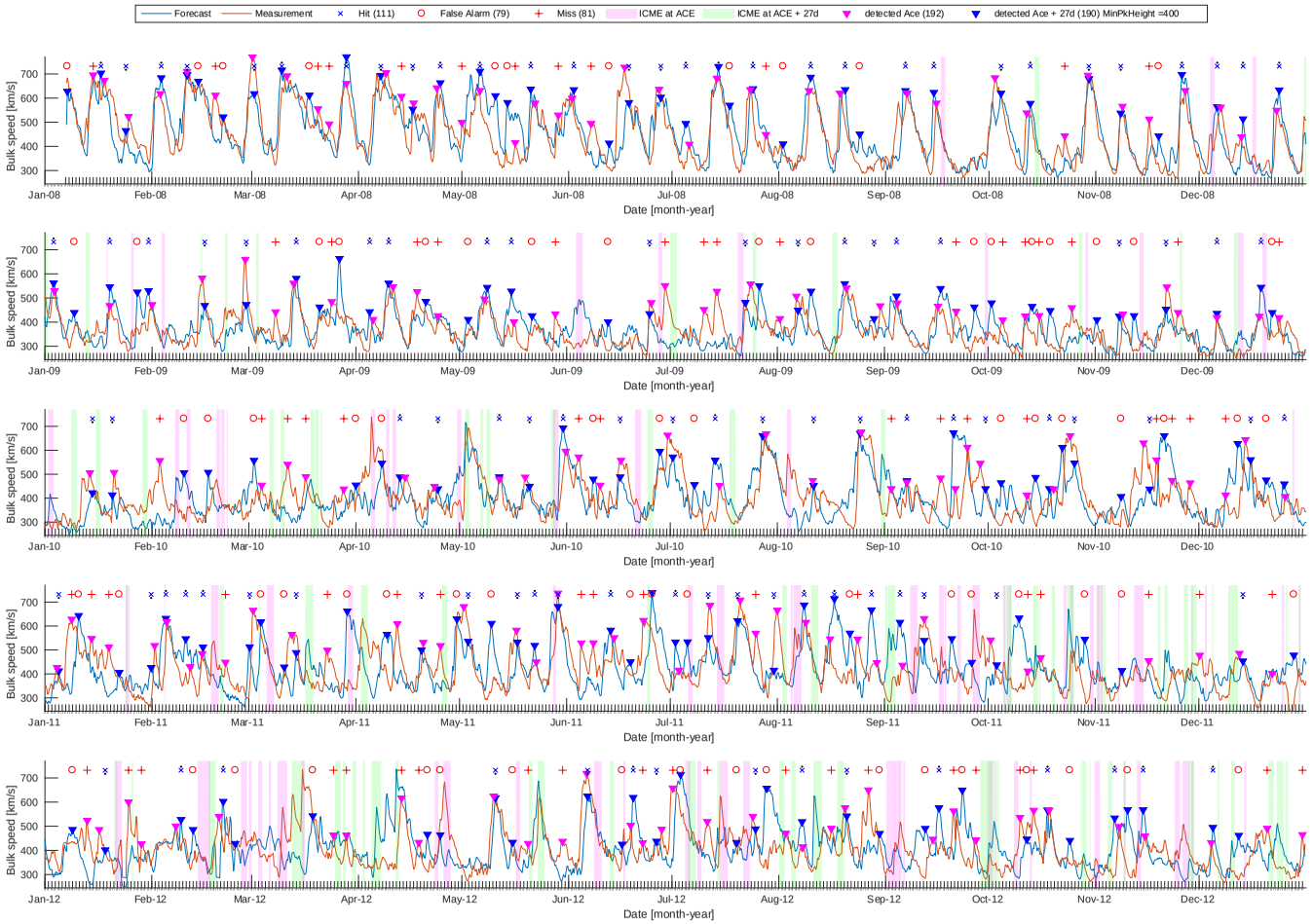

Figure 6.1.: Solar wind speed measured by ACE (orange curve) from January 2008 to December 2012 in comparison to the predicted solar wind by the Persistence model 27d (blue curve). The red vertical bars indicate the times of CMEs according to the catalog of Richardson & Cane. For this model the ACE data is shifted 27d to the future, hence also the times of the CMEs are shifted correspondingly, indicated by the green vertical bars. The blue and pink triangles indicate detected peaks in the forecast and measurements, respectively. A hit is shown by a blue cross, where the black point indicates if the measured speed was over or underestimated by the forecast. A red circle represents a false alarm, whereas a red plus sign denotes a miss. In the top of the number of hits, false alarms, misses and the total number of detected peaks in the measurement and the forecast are given.

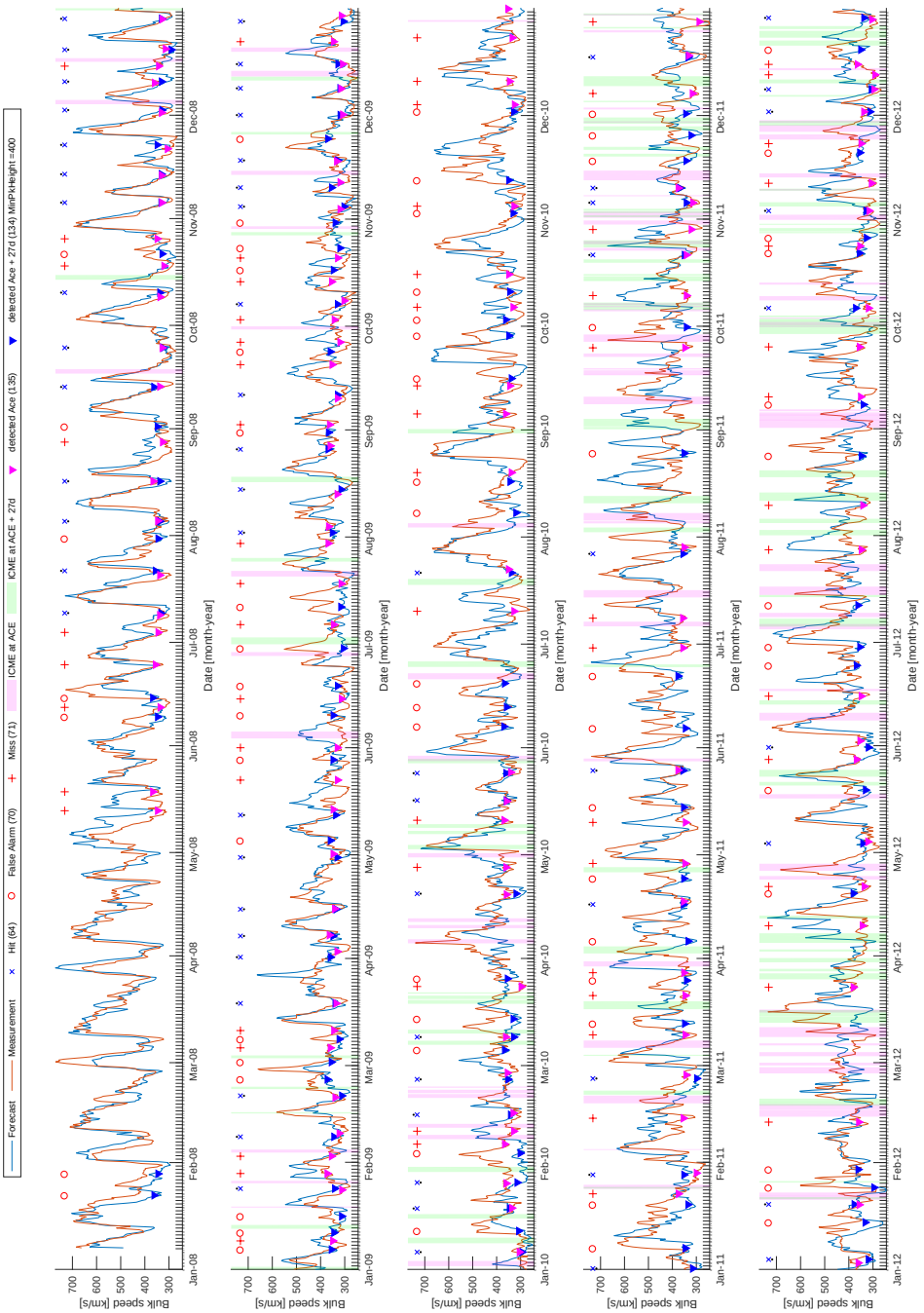

Figure 6.2.: Persistence model 27d. Same as in Figure 6.1 but for the base level.

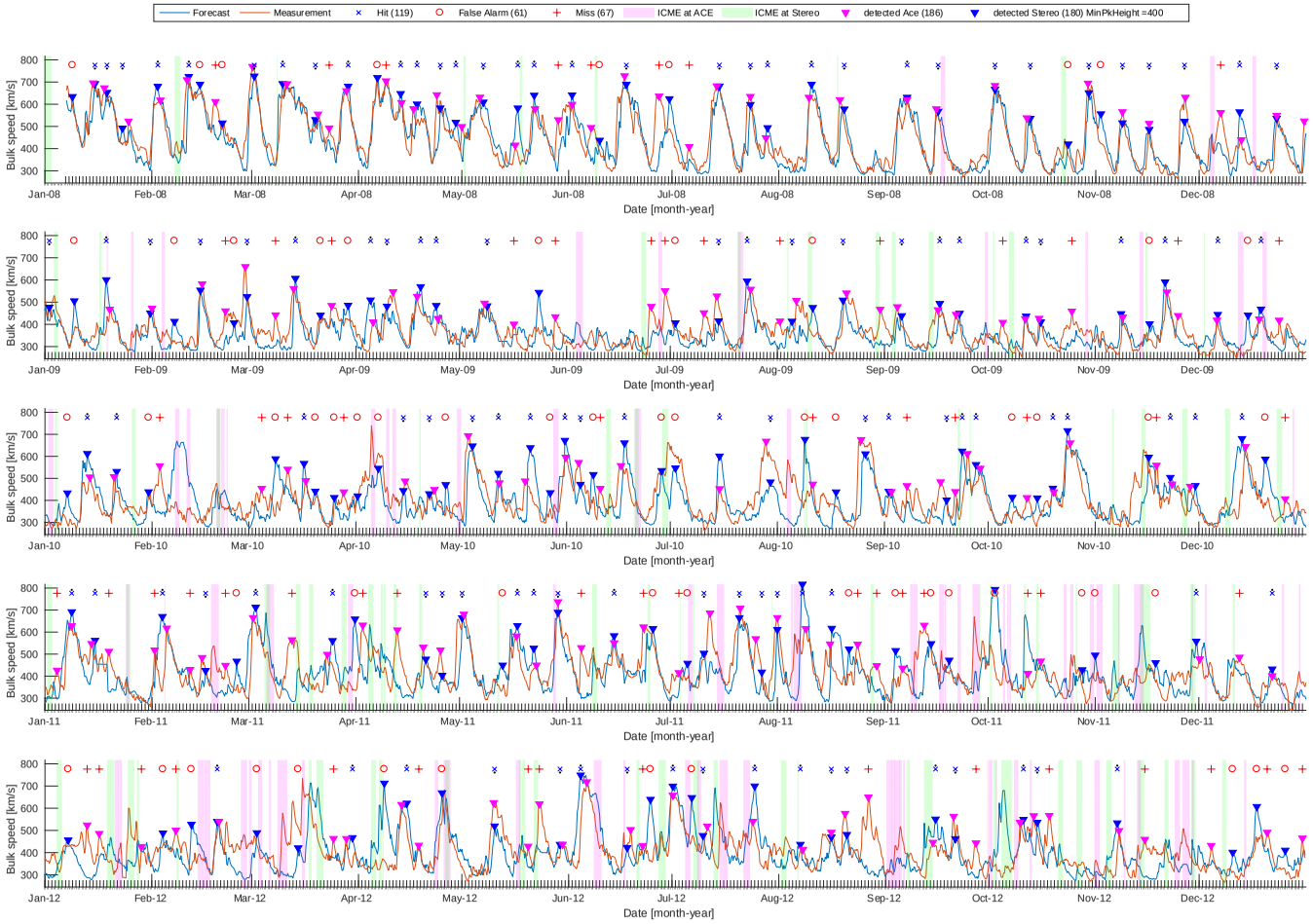

Figure 6.3.: Solar wind speed measured by ACE (orange curve) from January 2008 to December 2012 in comparison to the predicted solar wind by the Persistence model STEREO (blue curve) using peak detection. The red vertical bars indicate the times of CMEs at ACE according to the catalog of Richardson & Cane and the green vertical bars indicate the times of CMEs at STEREO-B according to the catalog of L. Jian. For a detailed description of the symbols see Figure 6.1.

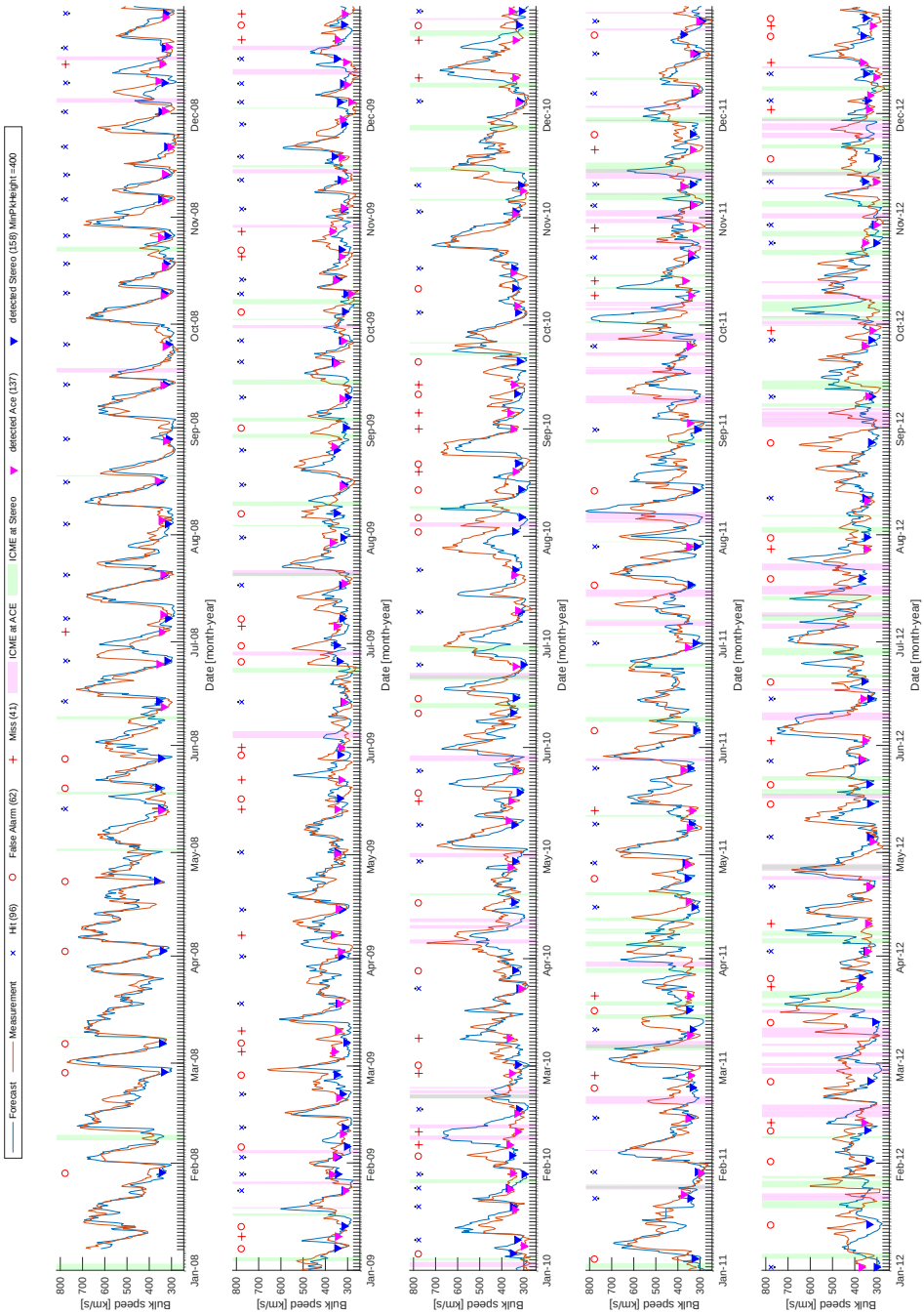

Figure 6.4.: Persistence model STEREO. Same as in Figure 6.3 but for the base level.

Table 6.1.: Definition of the persistence levels and the factors to update the solar wind speed for the Persistence model STEREO+CH.

Version	Persistence Level			Wind speed factor		
	High	Medium	Low	High	Medium	Low
V1	$(0.0–0.7)r_{CH_{MAD}}$	$(0.7–1.4)r_{CH_{MAD}}$	$> 1.4r_{CH_{MAD}}$	$0.5v_{MAD}$	$1.0v_{MAD}$	$1.5v_{MAD}$
V2	$(0.0–1.0)r_{CH_{MAD}}$	$(1.0–2.0)r_{CH_{MAD}}$	$> 2.0r_{CH_{MAD}}$	$0.5v_{MAD}$	$1.0v_{MAD}$	$1.5v_{MAD}$

Table 6.2.: Statistical results of the continuous variables for the solar wind speed [km/s] covering the time range January 2008 to December 2012. "ST" stands for STEREO and "ST+CH_V1" for STEREO+CH_V1. NO means that CMEs are excluded from the statistical analysis. ME is the mean error, MAE the mean average error and RMSE is the root-mean-square error. Mean M is the mean speed measured and Std M the standard deviation measured, hence Mean F and Std F are the mean and standard deviation of the forecast.

Persistence model	ME	MAE	RMSE	Mean M	Std M	Mean F	Std F
27d/NO (eg. Fig. 6.1)	−2.36	66.03	88.31	411.97	94.83	414.33	96.22
ST/NO (eg. Fig. 6.3)	9.79	57.15	79.28	411.94	95.08	402.15	99.71
ST+CH_V1/NO (eg. Fig. 6.5)	−3.86	57.99	79.62	411.94	95.08	415.80	103.05

2006). One has to keep in mind, that over time STEREO-B separates more and more from Earth (22° separation angle in January 2008 and 130° in December 2012) causing an increased forecast lead time, but also the time for CHs to possibly undergo some changes increases.

In Figure 6.5 and Figure 6.6 the comparison of the Persistence model STEREO+CH can be found for the peaks and the base levels, respectively. The values defining the persistence level and to update the solar wind speed are listed in Table 6.1. The figures for the Persistence model STEREO and Persistence model STEREO+CH with different definitions of the persistence levels and speed factors, and the figures including times of CMEs are shown in the Appendix A (Figures A.3–A.10).

To make the results of the different models better comparable, the continuous variables of the best performing empirical models are summarized in Table 6.2. Listed are the mean error (ME), the mean absolute error (MAE), and the root-mean-square error (RMSE). In addition, the mean and standard deviation of the measured and predicted solar wind speeds are given. The event-based results are presented in Table 6.3. They contain the number of hits, false alarms and misses as well as FAR, TS, BS, POD and RUS. For each hit we obtain the time difference (dt) and the speed difference (dv) between the forecast and the measurement and calculate the mean and standard deviation for both. The tables containing the results for all studied empirical models and different variants with the times of the CMEs excluded and included can be found in Appendix B (Table B.1 and Table B.2).

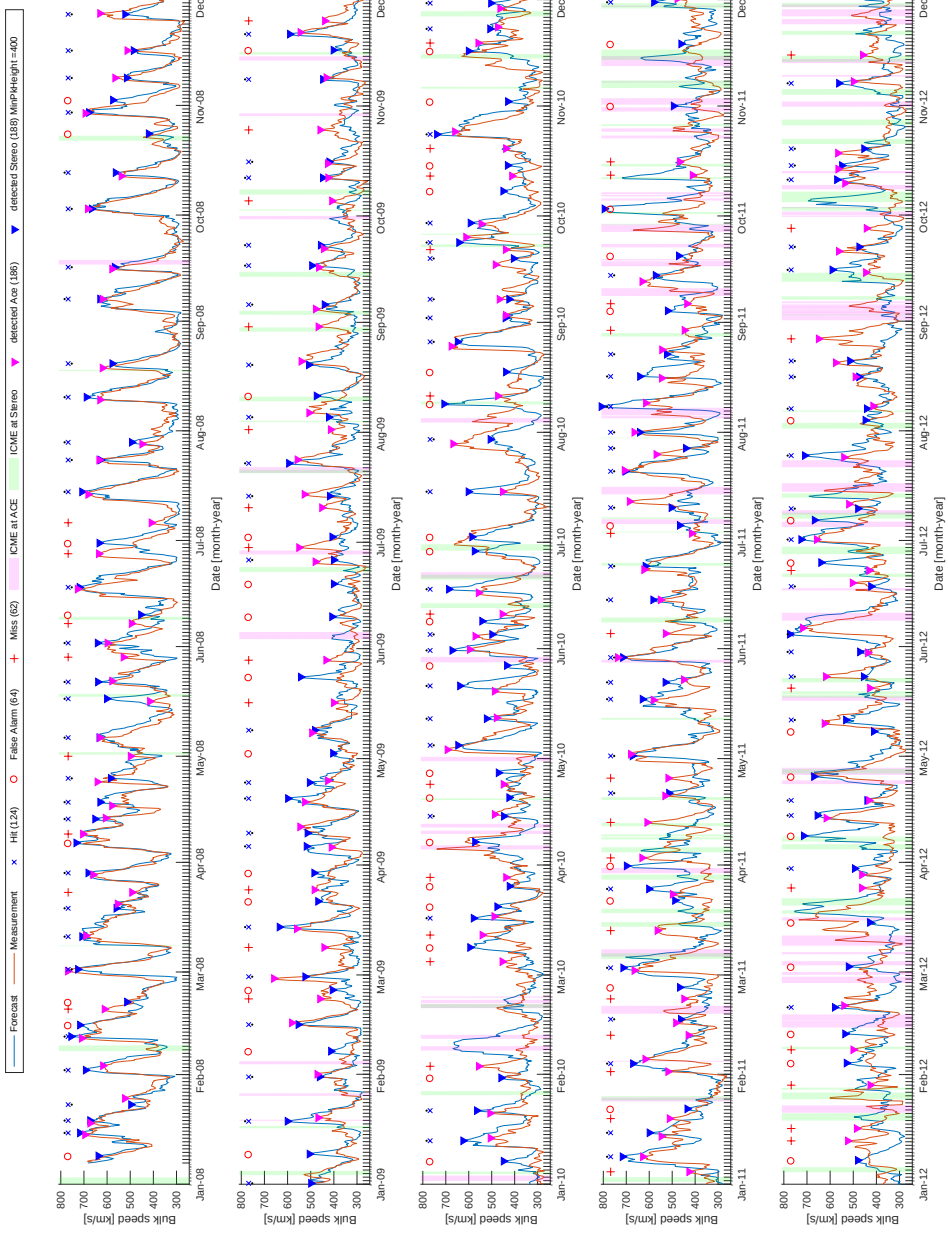

Figure 6.5.: Solar wind speed measured by ACE (orange curve) from January 2008 to December 2012 in comparison to the predicted solar wind by the Persistence model STEREO+CH_V1 (blue curve) using peak detection. For a detailed description of the symbols see Figure 6.1.

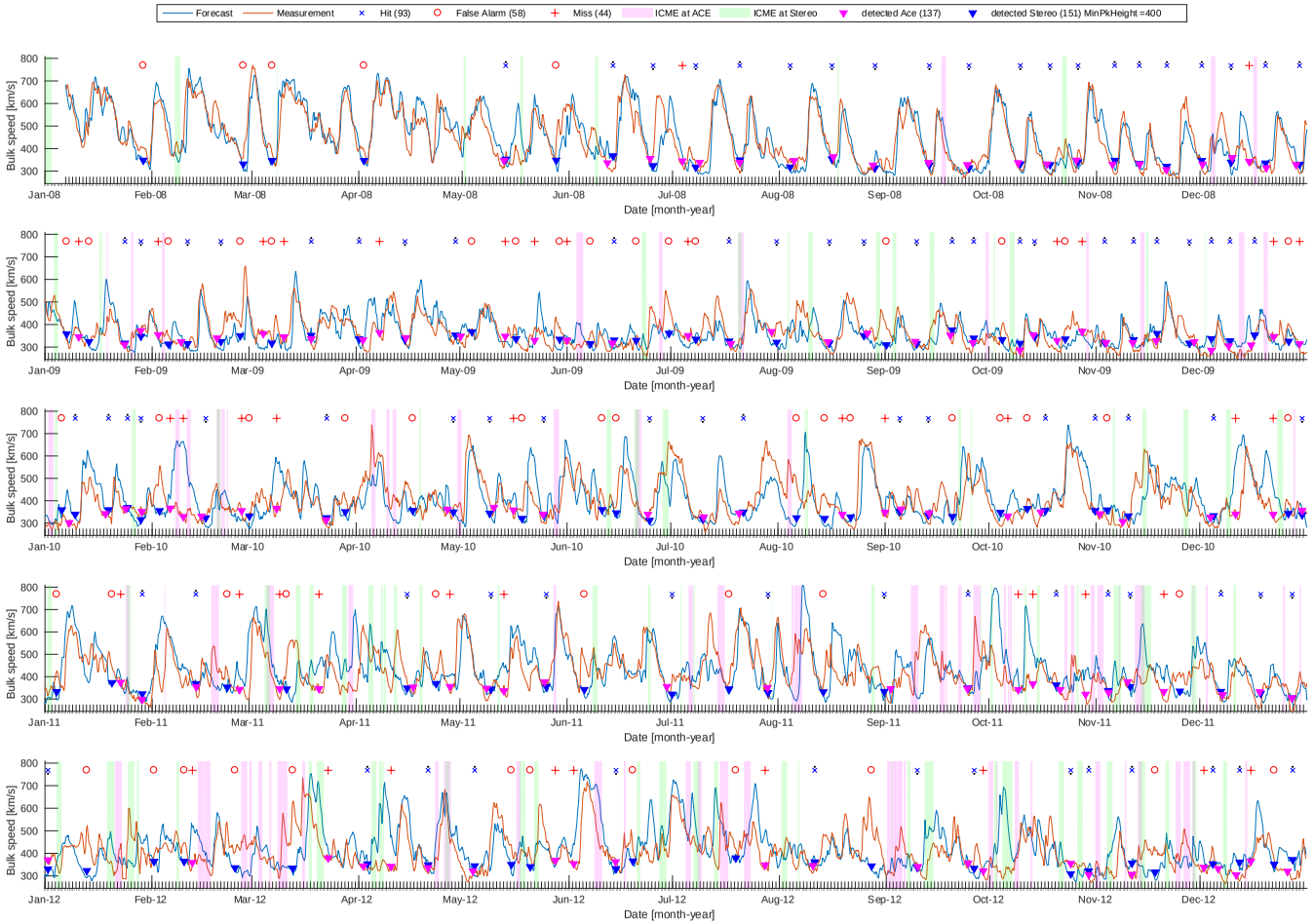

Figure 6.6.: Persistence model STEREO+CH_V1. Same as in Figure 6.5 but for the base level.

Table 6.3.: Event-based statistics for the peaks and the base levels detected in the time range January 2008 to December 2012. "ST" stands for STEREO and "ST+CH_V1" for STEREO+CH_V1. NO means that CMEs are excluded. TP are the hits, FP the false alarms and FN the misses. FAR is the false alarm ratio, TS the threat score (best: TS = 1, worst: TS = 0), BS the bias (BS < 1 underestimation, BS > 1 overestimation) and POD the probability of detection. RUS gives the ratio of underestimated speed. Mean *dt* and Std *dt* represent the mean and standard deviation of the time difference (*dt*) in the forecast and the measurement [hours] calculated only for hits. Likewise the mean and standard deviation of the speed differences (*dv*) in the measured and predicted solar wind speed [km/s] are calculated.

Persistence model	TP	FP	FN	FAR	TS	BS	POD	RUS	Mean dt	Std dt	Mean dv	Std dv
Peak detection												
27d/NO (Fig. 6.1)	111	79	81	0.42	0.41	0.99	0.58	0.46	-0.00	0.93	0.46	86.60
ST/NO (Fig. 6.3)	119	61	67	0.36	0.48	0.97	0.66	0.45	0.07	0.89	3.72	69.41
ST+CH_V1/NO (Fig. 6.5)	124	64	62	0.33	0.50	1.01	0.66	0.42	0.11	0.86	13.50	71.35
Base level detection												
27d/NO (Fig. 6.2)	64	70	71	0.53	0.31	0.99	0.48	0.48	-0.17	0.81	−0.47	23.13
ST/NO (Fig. 6.4)	96	62	41	0.30	0.48	1.15	0.61	0.60	0.20	0.84	−5.77	21.93
ST+CH_V1/NO (Fig. 6.6)	93	58	44	0.32	0.48	1.10	0.62	0.48	0.21	0.84	1.54	21.87

When comparing the persistence models, it should be mentioned that most of them perform better when times of CME occurrences are excluded from the analysis. This is expected, especially for the Persistence model 27d since CMEs represent transient disturbances in the solar wind background and can therefore not be considered as recurrent events. The statistical analysis of the empirical models is done using data from January 2008 to December 2012. Table B.1 in Appendix B lists the continuous variables for all three persistence models. YES indicates, that the times of the CMEs are included in the analysis while NO means that those times are not included. As a consequence, the mean and standard deviation of the measurements slightly differ. The table also includes different variants of the STEREO+CH forecast model. The models differ in the way the persistence levels are defined (see Table 6.1). The continuous variables in Table 6.2 are just given for the best performing models and indicate that the Persistence models STEREO and STEREO+CH_V1 are quite comparable (MAE ∼58 km/s and RMSE ∼80 km/s).

The event-based analysis of the best performing empirical models for the peaks and base levels can be found in Table 6.3. The Persistence model STEREO+CH_V1 produces 124 hits, 64 false alarms and 62 misses. Compared to the Persistence model 27d, the hit rate of the peak detection increases by about 12% whereas false alarms and misses are decreased by roughly 19% and 23%, respectively. The Persistence model STEREO+CH_V1 shows the smallest (0.33) false alarm ratio, while the probability of detection (POD = 0.66) and the threat score (TS = 0.50) are comparable to the

other models and variants. The ratio of underestimated speed (RUS = 0.42) indicates that in 42% the peak velocity was underestimated by the model. Consequently, in 58% the peak velocity was overestimated. Also the time differences (dt) between hits in the measurement and in the forecast are similar (Mean dt: 0.11 ± 0.86 hours), whereas the mean speed differences dv of the hits is 13.5 ± 71.4 km/s. The event-based analysis was also applied to the base levels (Table 6.3). The Persistence model STEREO performs slightly better than the STEREO+CH_V1, which provides 93 hits, 58 false alarms, and 44 misses (FAR: 0.32, TS: 0.48, BS: 1.10, POD: 0.62, RUS: 0.48, Mean dt: 0.21 ± 0.84 hours, Mean dv: 1.54 ± 21.9 km/s). Taking into account the Persistence model STEREO+CH_V1, the hit rate is increased approximately by 45% whereas the false alarm and miss rates are decreased by about 17% and 38% compared to the Persistence model 27d. Again, the table containing the results of all the empirical models with the CMEs included and excluded can be found in the Appendix B (Table B.2).

Based on these results, especially on the results for the peak detection, we conclude that the Persistence model STEREO+CH_V1 performs best for the years 2008 to 2012, leading to a larger amount of correctly predicted hits and less false alarms and misses.

6.2. Results for the numerical models

In this Section we present the result for the numerical forecast models. The solar wind forecasts of EUHFORIA and ENLIL (with WSA) are analyzed and compared to ACE in-situ measurements. EUHFORIA model outputs are only available for four months (March to June) in 2008 and three months (March to May) in 2012. Hence, only the ENLIL model runs for the corresponding Carrington rotations are considered. The continuous variables are calculated for the various modeled solar wind parameters (bulk velocity v_b, density n, pressure P, temperature T, total magnetic field B_t, B_z component of the magnetic field). In addition, the event-based verification is applied to the solar wind bulk velocity v_b.

6.2.1. Comparison of the modeled solar wind bulk velocity with in-situ measurements

The results for the peak detection of the EUHFORIA model output obtained with the default settings (± 1 day for the Gaussian weight with the central region at 0°) are shown in Figure 6.7. In Figure 6.8 the solar wind bulk velocity modeled by ENLIL in comparison to the in-situ measurements can be seen. As already described in Section 5.2.1.1, we want to evaluate how different setting for the generation of the EUHFORIA time series affect our results. We therefore change the time range used for the Gaussian weighting to ±2 days, ±3 days, and ±5 days. In addition, the central region was shifted using values from −2 days to +2 days. The analysis was again done for the detected peaks and base levels. Since there was no CME

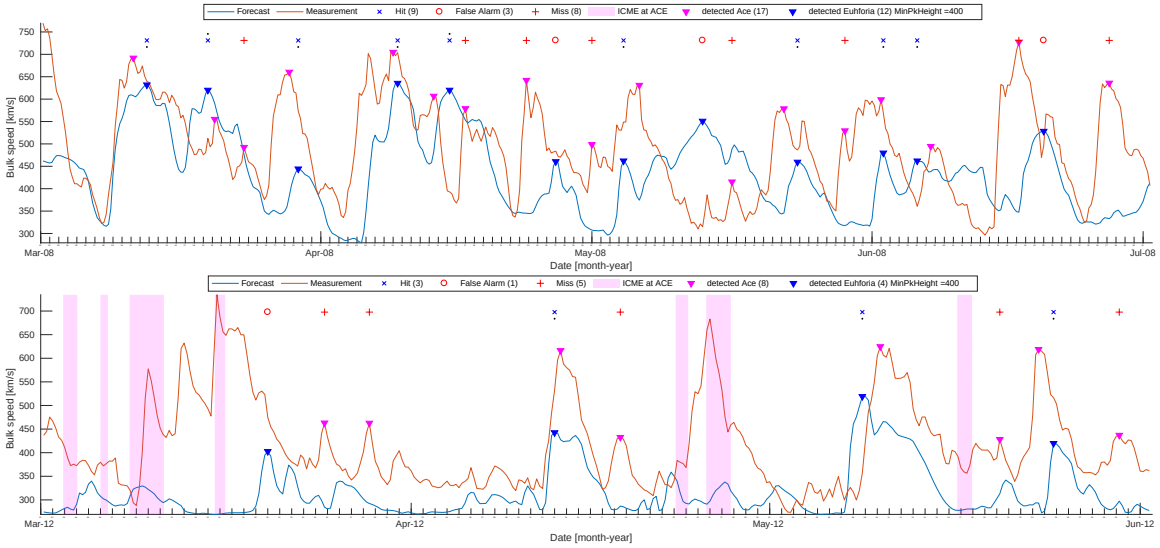

Figure 6.7.: Solar wind speed measured by ACE (orange curve) for 2008 (top) and 2012 (bottom) in comparison to the predicted solar wind by the EUHFORIA model output (blue curve), with the default settings (± 1 day for the Gaussian weight with the central region at 0°). For a detailed description see Figure 6.1.

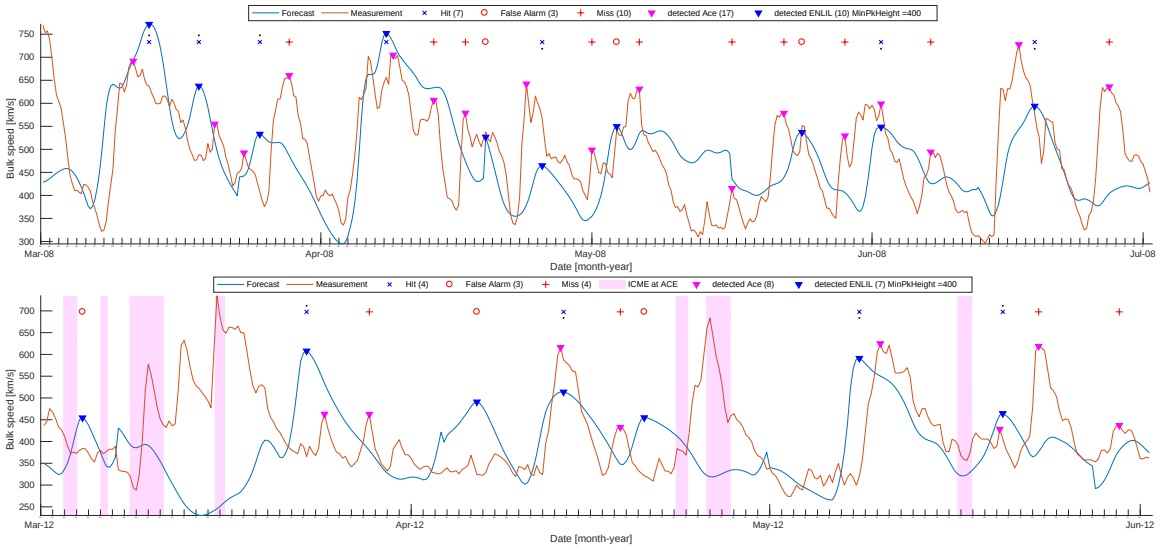

Figure 6.8.: Solar wind speed measured by ACE (orange curve) for 2008 (top) and 2012 (bottom) in comparison to the predicted solar wind by ENLIL (blue curve). For a detailed description see Figure 6.1.

Table 6.4.: Statistical results of the continuous variables for the solar wind speed [km/s] modeled by EUHFORIA and ENLIL for 2008 and 2012. EUH is the abbreviation for EUHFORIA. NO means that CMEs are excluded from the statistical analysis. For EUHFORIA default means that the time range used for the Gaussian weighting is set to ±1 day and the central region is not shifted, otherwise the exact time range [days] for the Gaussian weighting is given or the shift of the central region [days]. For a detailed description of the continuous variables see Table 6.2.

Model	ME	MAE	RMSE	Mean M	Std M	Mean F	Std F
			2008				
EUH (default) (Fig. 6.7)	57.86	106.43	135.36	492.40	104.95	434.54	89.23
EUH (shift: +2) (Fig. A.18)	59.03	103.98	132.03	492.40	104.95	433.38	86.56
ENLIL (Fig. 6.8)	6.71	81.60	101.78	492.40	104.95	485.70	100.39
			2012				
EUH/NO (default) (Fig. 6.7)	96.11	102.86	131.60	413.00	90.63	316.90	54.38
EUH/NO (shift: +1) (Fig. A.17)	93.64	98.67	127.12	413.00	90.63	319.37	53.16
ENLIL/NO (Fig. 6.8)	21.38	89.38	122.77	413.00	90.63	391.62	81.58

detected at the location of ACE in the four months in 2008, only one speed curve is shown for the EUHFORIA model. All the corresponding in-situ measured solar wind speed curves in comparison to the EUHFORIA modeled curves can be found in the Appendix A (Figures A.12–A.26).

In Table 6.4 we list the continuous variables of the best performing numerical models for the years 2008 and 2012, respectively. The tables containing the information of the EUHFORIA model with different settings and all the ENLIL model results can be found in Appendix B (Table B.3 and Table B.4). Tables 6.5–6.6 list the event-based results for the peaks and base levels of the numerical solar wind models for different EUHFORIA settings and for ENLIL, separately for 2008 and 2012.

Just like the empirical models, also the numerical models perform better when excluding the times of CME occurrences. All the EUHFORIA models with the different settings (ranges and shifts) show similar results (see Table B.3 and Table B.4). (shift: +2) means that the time range used for the Gaussian weighting is set to ±1 day and the central region is shifted to +2 days. Table 6.4 lists the results only for selected numerical models. EUHFORIA (shift: +2) is the best performing EUHFORIA model in 2008, having a MAE of 104 km/s and a RMSE of 132 km/s. In comparison, ENLIL gives better results considering the continuous variables (MAE: 82 km/s, RMSE: 102 km/s). For the three months in 2012, again EUHFORIA gives similar results for the different settings, with EUHFORIA (range: +1), meaning that the central region is shifted to +1 day, performing best (MAE: 99 km/s, RMSE: 127 km/s). For this time range, ENLIL gives slightly better results (MAE: 89 km/s, RMSE: 123 km/s).

The event-based results for selected numerical models considering the peaks in 2008 can be found in Table 6.5. The EUHFORIA model runs with different settings are

Table 6.5.: Event-based statistics for the peaks of the solar wind speed [km/s] modeled by EUHFORIA and ENLIL covering the time range March to June 2008. During these times no CMEs at ACE were detected. For EUHFORIA default means that the time range used for the Gaussian weighting is set to ±1 day and the central region is not shifted, otherwise the exact time range [days] for the Gaussian weighting is given or the shift of the central region [days]. For a detailed description of the event-based variables see Table 6.3.

Model	TP	FP	FN	FAR	TS	BS	POD	RUS	Mean dt	Std dt	Mean dv	Std dv
Peak detection												
EUH (default) (Fig. 6.7)	9	3	8	0.47	0.45	0.71	0.75	0.78	0.28	1.33	−78.45	88.05
ENLIL (Fig. 6.8)	7	3	10	0.59	0.35	0.59	0.70	0.43	0.64	1.47	−15.90	105.78
Base level detection												
EUHFORIA (default) (Fig. A.19)	0	9	4	1.00	0.00	2.25	0.00	NaN	NaN	NaN	NaN	NaN
ENLIL (Fig. A.34)	0	3	4	1.00	0.00	0.75	0.00	NaN	NaN	NaN	NaN	NaN

Table 6.6.: Event-based statistics for the peaks and the base levels of the solar wind speed [km/s] modeled by EUHFORIA and ENLIL covering the time range March to May 2012. NO means that CMEs are excluded from the statistical analysis. For EUHFORIA default means that the time range used for the Gaussian weighting is set to ±1 day and the central region is not shifted, otherwise the exact time range [days] for the Gaussian weighting is given or the shift of the central region [days] For a detailed description of the event-based variables see Table 6.3.

Model	TP	FP	FN	FAR	TS	BS	POD	RUS	Mean dt	Std dt	Mean dv	Std dv
Peak detection												
EUH/NO (default) (Fig. 6.7)	3	1	5	0.62	0.33	0.50	0.75	1.00	−0.25	1.39	−159.52	48.36
EUH/NO (shift: +2) (Fig. A.18)	5	0	3	0.38	0.62	0.62	1.00	0.80	0.35	1.28	−96.20	105.29
ENLIL/NO (Fig. 6.8)	4	3	4	0.50	0.36	0.88	0.57	0.50	−0.69	1.09	11.16	105.62
Base level detection												
EUH/NO (default) (Fig. A.19)	2	5	3	0.60	0.20	1.40	0.29	1.00	-1.69	0.27	-28.59	1.32
EUH/NO (range: ±2) (Fig. A.20)	2	4	3	0.60	0.22	1.20	0.33	1.00	-1.62	0.35	-24.55	1.79
EUH/NO (shift: +2) (Fig. A.26)	2	6	3	0.60	0.18	1.60	0.25	0.50	0.00	0.88	-5.10	21.03
ENLIL/NO (Fig. A.34)	2	5	3	0.60	0.20	1.40	0.29	1.00	-0.62	1.41	-8.60	4.53

quite comparable having a FAR of 0.47, POD of 0.75, TS of 0.45 and BS of 0.71. 9 hits, 3 false alarms and 8 misses were detected and most of the time the predicted solar wind bulk speed was underestimated (RUS: 0.78). dt and dv represent the time and the solar wind speed difference calculated for the hits only. For 2008, EUHFORIA provides $dt = 0.28 \pm 1.33$ hours and $dv = -78.5 \pm 88.1$ km/s. With 7 hits, 3 false alarms and 10 misses, a FAR of 0.59, POD of 0.70, TS of 0.35 and BS of 0.59, ENLIL is not able to reach the performance of EUHFORIA in 2008. Also $dt = 0.64 \pm 1.47$ hours and $dv = -15.9 \pm 105.8$ km/s are larger for ENLIL. Considering the event-based results for the base levels of 2008, neither EUHFORIA nor ENLIL produce a hit. As a consequence, FAR is 1.00 and POD is 0.00. Since RUS, mean dt, std dt, mean dv, std dv are only calculated for the hits, these values could not be calculated. It should be noted, however, that ENLIL gives only 3 false alarms, whereas EUHFORIA produces 8 false alarms.

The event-based results for the peaks and base levels in 2012 are listed in Table 6.6. During this time EUHFORIA (shift: +2) performs best for the peak detection, where 5 hits, no false alarm and 3 misses are obtained. FAR is given by 0.38 and POD is 1.00 since no false alarms are detected. BS is 0.62 and 80% (RUS = 0.80) of the peak solar wind speeds are underestimated. The timing of the predicted hits is given by $dt = 0.35 \pm 1.28$ hours and the speed difference by $dv = -96.2 \pm 105$ km/s. ENLIL, on the other hand, produces 4 hits, 3 false alarms and 4 misses, leading to a FAR of 0.50, POD of 0.57, TS of 0.36 and BS of 0.88. The speed of 50% of the detected hits is underestimated. The timing and especially the velocities of the hits are better predicted ($dt = -0.69 \pm 1.09$ hours, $dv = 11.2 \pm 105$ km/s). When considering the base levels in 2012 (see Table 6.6), EUHFORIA (range: ± 2) and EUHFORIA (shift: -2) give the best results, which are comparable to ENLIL (2 hits, 5 false alarms, 3 misses, FAR: 0.60, POD: 0.29, TS: 0.20, BS: 1.40, RUS: 1.00), but ENLIL is better able to simulate the speeds of the detected hits ($dv = -8.6 \pm 4.5$ km/s). The continuous variables and the peak and base level detection results for all forecast models can be found in Appendix B (Tables B.3–B.8).

Based on these results, it seems that ENLIL performs slightly better than EUHFORIA. When having a look at the top panel of Figure 6.7, one sees that beginning in May 2008 the solar wind bulk speed predicted by EUHFORIA differs from the ACE measurements considerably and is in general too low (year 2012). Interestingly, both EUHFORIA and ENLIL overestimate the solar wind speed in mid May 2008. A reason may be found in the GONG input magnetograms used by the numerical models and should be studied in detail. This, however, goes beyond the scope of this thesis.

6.2.2. Other solar wind parameters

EUHFORIA not only provides the bulk velocity, but also other solar wind parameters. In Figures 6.9–6.13 we show the EUHFORIA curves in comparison to the in-situ measurements for the density n, pressure P, temperature T, total magnetic field B_t, and the B_z component of the magnetic field. Since the EUHFORIA (shift: +2)

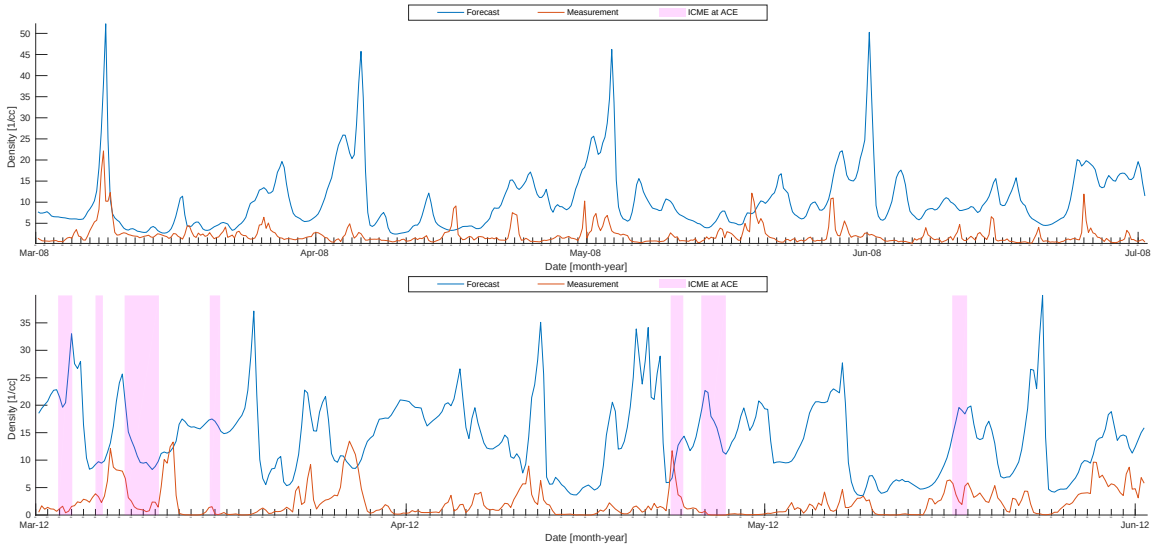

Figure 6.9.: Solar wind density obtained by ACE (orange curve) for 2008 (top) and 2012 (bottom) in comparison to the EUHFORIA solar wind density forecast. The red vertical bars indicate the times of CMEs.

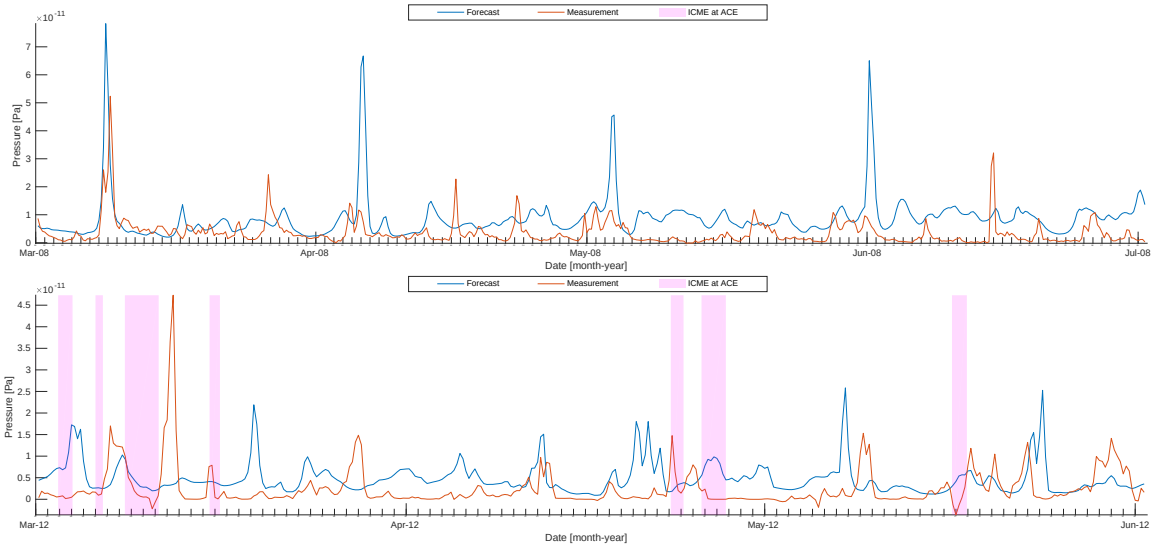

Figure 6.10.: Solar wind pressure obtained by ACE (orange curve) for 2008 (top) and 2012 (bottom) in comparison to the EUHFORIA solar wind pressure forecast. The red vertical bars indicate the times of CMEs.

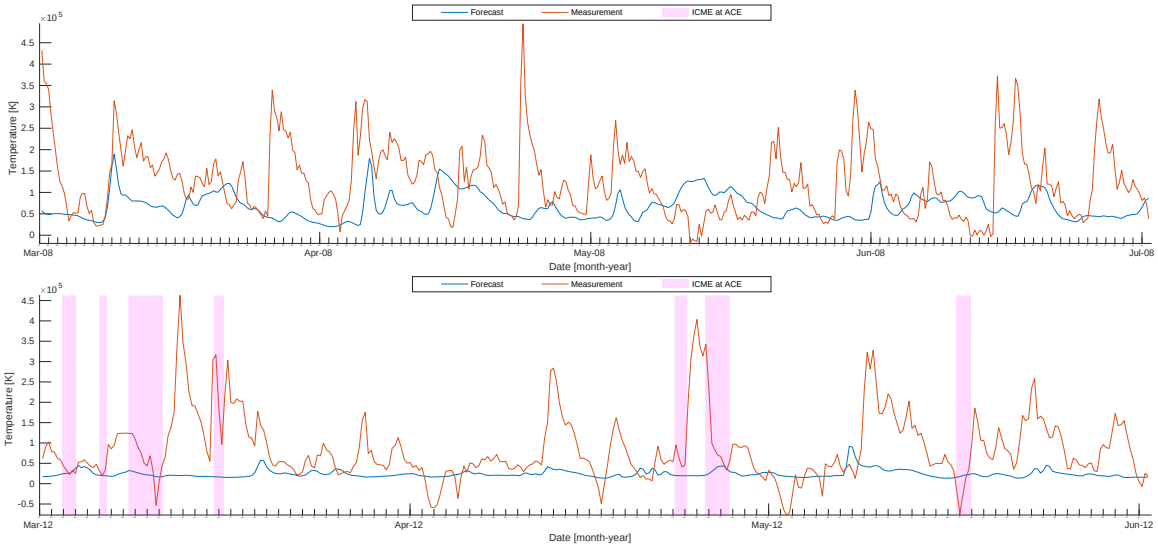

Figure 6.11.: Solar wind temperature obtained by ACE (orange curve) for 2008 (top) and 2012 (bottom) in comparison to the EUHFORIA solar wind temperature forecast. The red vertical bars indicate the times of CMEs.

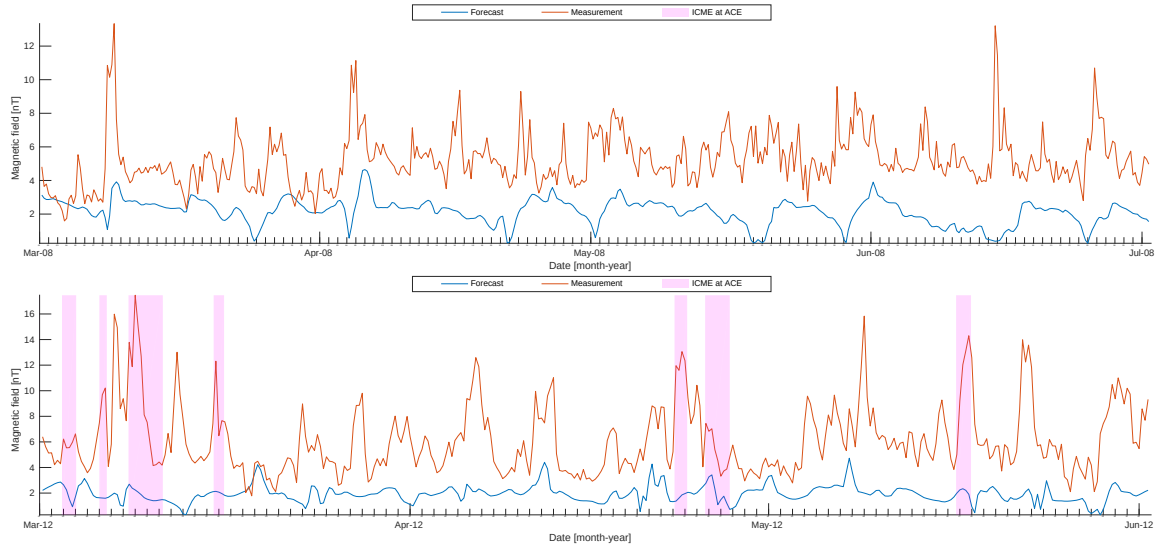

Figure 6.12.: Solar wind total magnetic field obtained by ACE (orange curve) for 2008 (top) and 2012 (bottom) in comparison to the EUHFORIA solar wind total magnetic field forecast. The red vertical bars indicate the times of CMEs.

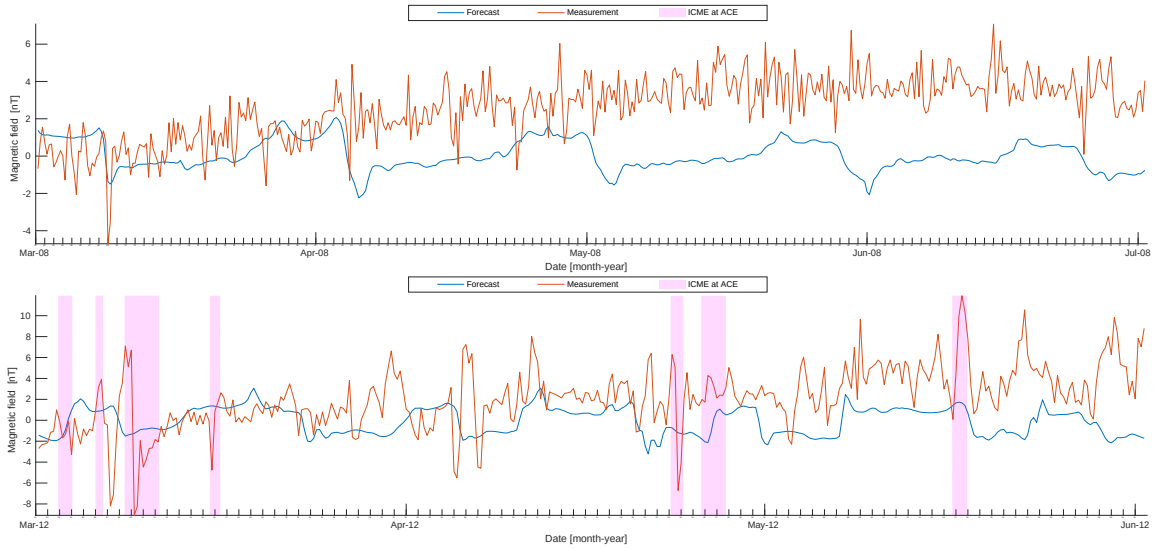

Figure 6.13.: Solar wind B_z obtained by ACE (orange curve) for 2008 (top) and 2012 (bottom) in comparison to the EUHFORIA solar wind B_z forecast. The red vertical bars indicate the times of CMEs.

Table 6.7.: Statistical results of the continuous variables for the solar wind parameters modeled by EUHFORIA and ENLIL covering the time range March to June 2008. For a detailed description see Table 6.4.

Parameter	ME	MAE	RMSE	Mean M	Std M	Mean F	Std F	Unit
EUH: v_b (shift: +2) (Fig. A.18)	59.03	103.98	132.03	492.40	104.95	433.38	86.56	[km s^{-1}]
ENLIL: v_b (Fig. 6.8)	6.71	81.60	101.78	492.40	104.95	485.70	100.39	[km s^{-1}]
EUH: n (shift: +2) (Fig. A.28)	−8.23	8.30	10.37	2.12	2.18	10.34	6.46	[cm^{-3}]
ENLIL: n (Fig. A.35)	−3.39	3.79	4.60	2.12	2.18	5.51	2.54	[cm^{-3}]
EUH: P (shift: +2) (Fig. A.29)	−4.97	6.00	8.35	3.57	4.65	8.54	6.31	[$10^{-12}\times$Pa]
ENLIL: P (Fig. A.36)	−1.15	3.17	4.93	3.57	4.65	4.72	2.55	[$10^{-12}\times$Pa]
EUH: T (shift: +2) (Fig. A.30)	58.97	77.11	101.76	125.69	81.27	66.71	29.90	[$10^{3}\times$K]
ENLIL: T (Fig. A.37)	60.39	70.73	97.21	125.69	81.27	65.30	21.63	[$10^{3}\times$K]
EUH: B_t (default) (Fig. 6.12)	3.05	3.06	3.54	5.19	1.60	2.14	0.75	[nT]
ENLIL: B_t (Fig. A.38)	2.48	2.60	2.99	5.19	1.60	2.71	1.19	[nT]
EUH: B_z (default) (Fig. 6.13)	2.56	2.79	3.20	2.60	1.65	0.03	0.80	[nT]
ENLIL: B_z (Fig. A.39)	0.22	1.42	1.81	2.60	1.65	2.37	0.83	[nT]

Table 6.8.: Statistical results of the continuous variables for the solar wind parameters modeled by EUHFORIA and ENLIL covering the time range March to May 2012. For a detailed description see Table 6.4.

Parameter	ME	MAE	RMSE	Mean M	Std M	Mean F	Std F	Unit
EUH/NO: v_b (shift: +2) (Fig. A.18)	93.03	99.10	128.90	413.00	90.63	319.98	52.61	[km s^{-1}]
ENLIL/NO: v_b (Fig. 6.8)	21.38	89.38	122.77	413.00	90.63	391.62	81.58	[km s^{-1}]
EUH/NO: n (default) (Fig. 6.9)	−11.87	11.95	13.99	2.23	2.65	14.10	6.89	[cm^{-3}]
ENLIL/NO: n (Fig. A.35)	−6.68	7.17	9.21	2.23	2.65	8.91	5.58	[cm^{-3}]
EUH/NO: P (default) (Fig. 6.10)	−2.10	4.46	6.44	2.65	4.75	4.75	3.64	[$10^{-12}\times$Pa]
ENLIL/NO: P (Fig. A.36)	−3.57	5.53	8.72	2.65	4.75	6.22	6.05	[$10^{-12}\times$Pa]
EUH/YES: T (default) (Fig. 6.11)	61.55	70.49	101.64	85.61	81.67	24.06	9.40	[$10^3\times$K]
ENLIL/YES: T (Fig. A.37)	37.62	61.97	93.25	85.61	81.67	48.00	18.92	[$10^3\times$K]
EUH/NO: B_t (default) (Fig. 6.12)	3.93	3.93	4.65	5.88	2.46	1.95	0.65	[nT]
ENLIL/NO: B_t (Fig. A.38)	3.27	3.69	4.45	5.88	2.46	2.60	1.79	[nT]
EUH/NO: B_z (default) (Fig. 6.13)	2.29	2.99	3.81	2.24	2.66	-0.05	1.31	[nT]
ENLIL/NO: B_z (Fig. A.39)	−0.03	2.28	2.98	2.24	2.66	2.27	1.41	[nT]

model performed best for the bulk velocity, all parameters were also calculated using a shift of the central region to +2 days. The corresponding figures can be found in the Appendix A (Figures A.27–A.32) together with the figures for ENLIL (Figures A.33–A.39). The event-based verification for these parameters were not performed since the numerical models show essential offsets to the in-situ measured parameters. Only the continuous variables are calculated and can be found in Table 6.7 and Table 6.8 for 2008 and 2012, respectively. For the year 2008 EUHFORIA (shift: +2) gives better results for all the parameters except for B_t and B_z compared to the EUHFORIA model output with the default settings. In addition, ENLIL performs better than EUHFORIA (shift: +2) for all parameters.

As mentioned already, the models seem to perform better for the solar wind bulk velocity when excluding CMEs. For the year 2012, EUHFORIA (default) seems to give better results compared to EUHFORIA (shift: +2) except for the solar wind speed, but the differences are very small. ENLIL again performs better for all the parameters. Interestingly, EUHFORIA and ENLIL seem to give better results for the solar wind temperature when including the times of CMEs. The tables with all the continuous variables for EUHFORIA and ENLIL including and excluding times of CMEs can be found in the Appendix B (Table B.9 and Table B.10).

The numerical models in general underestimate the solar wind bulk velocity v_b and on the other hand overestimate the solar wind density n, which can be seen when comparing the values of the measurement ($v_b = 492 \pm 105$ km/s, $n = 2.1 \pm 2.2$ cm^{-3}) and the values of the forecast (EUHFORIA: $v_b = 433 \pm 87$ km/s, $n = 10.3 \pm 6.5$ cm^{-3}, ENLIL: $v_b = 486 \pm 100$ km/s, $n = 5.5 \pm 2.5$ cm^{-3}) for the year 2008. The differences are even bigger for the year 2012 where the measurements are $v_b = 413 \pm 91$ km/s, $n = 2.2 \pm 2.7$ cm^{-3}, and the forecasts of the numerical models are given by EUHFORIA: $v_b = 320 \pm 53$ km/s, $n = 14.1 \pm 6.9$ cm^{-3}, ENLIL: $v_b = 392 \pm 82$ km/s, $n = 8.9 \pm 5.6$ cm^{-3}. Comparing the mean absolute error (MAE: ∼104 km/s) and

the root-mean-square error (RMSE: ∼132 km/s) for the year 2008 shows that for the bulk velocity these errors are about one-third of the mean speed. For the density, however, MAE and RMSE are in the order of the mean density of the measurement. Similar results were obtained for the pressure P. The temperature T, total magnetic field B_t, and the B_z component of the magnetic field, on the other hand, are underestimated by the model for the selected time ranges in 2008 and 2012.

From all the parameters modeled by EUHFORIA, the solar wind bulk velocity v_b gives the best results. However, ENLIL seems to perform better in comparison to EUHFORIA considering all the solar wind parameters.

When considering the results of solar wind bulk velocity, one can see that EUHFORIA needs further improvement, including the timing of the peaks (especially for May and June 2008). Also the speed difference between the predicted and the measured high-speed streams needs to be adjusted (see Figure 6.7).

7. Summary and Conclusion

In this study a statistical analysis of the solar wind background speed modeled by different empirical models is presented. Considered is a time range, spanning for 5 years beginning in a solar minimum (January 2008) and reaching to a time of increased solar activity (December 2012). In addition, numerical solar wind forecast models are compared to in-situ measurements, where four months in the year 2008 and three months in 2012 are analyzed. We make use of ACE in-situ measurements which are compared to the different model forecasts.

The three empirical forecast models are: Persistence model 27d, Persistence model STEREO, and Persistence model STEREO+CH. The first model predicts the solar wind speed just by shifting the in-situ measurements one Carrington rotation ($\sim$27 days) in the future. The Persistence model STEREO is based on multi-viewpoint in-situ measurements obtained by STEREO, where the observed speeds are shifted in time according to the separation angle between STEREO and Earth view (e.g., ACE). Persistence model STEREO+CH, a newly developed forecast model by Temmer et al. (2018), is also based on STEREO in-situ measurements but additionally takes the evolution of CHs into account. Vršnak et al. (2007) showed that the solar wind parameters are closely related to the area and position of CHs. Gómez-Herrero et al. (2011) found that an expansion of a CH results in an increase in the in-situ measured solar wind speed, which was taken into account for the Persistence model STEREO+CH.

In Section 6.1 the statistical results of the empirical models are shown. It should be noted, that they give better results when excluding the times of CME occurrences. To find those times we use ready catalogs maintained by Richardson & Cane for CMEs at ACE and L. Jian for CMEs at STEREO (for a detailed description of the catalogs see Richardson and Cane, 2010 and Jian et al., 2006, respectively). We find that in general the Persistence model STEREO+CH performs best for the 5 years. When taking the evolution of the CH into account, we are able to predict about 12% more hits for the peaks and reduce the false alarm rate and the misses by roughly 19% and 23%, compared to the Persistence model 27d. In addition, the hits were predicted within less than one day ($dt = 0.11 \pm 0.86$ hours). The Persistence model STEREO+CH provides even better results compared to the Persistence model 27d for the base level detection. Approximately 45% more hits, 19% less false alarms and 23% less misses are produced.

Owens et al. (2013) already performed a statistical analysis on the Persistence model 27d for in-situ data ranging from 1995 to 2003 and illustrated how this tool can be used as an benchmark for more sophisticated forecast models. Kohutova et al. (2016) then studied the solar wind parameters (v, n, T, $|B|$, B_x, B_y and B_z) from

2007 to 2013 using data from STEREO-B. They also note, that the Persistence model STEREO performs best when excluding CME events. Based on the results found in the study of Temmer et al. (2018) for the time range where STEREO-B was east of Earth, also an operational Persistence model STEREO+CH was implemented (Solar Wind Forecast (STEREO+CH), University of Graz[10]), which uses STEREO-A in-situ measurements with CME times included. To exclude times of CME occurrences an automatic detection from in-situ data would be advantageous (Vennerstrom and Leer, 2015). The two STEREO spacecraft are very useful to predict the solar wind speeds at different longitudes. However, since they orbit around the Sun, the separation angle between the spacecraft and Earth constantly changes. Therefore, a future operational space weather monitor at L_5 is desired which would give predictions of the solar wind parameters with a constant lead time of about 4.5 days. This mission of course would need in-situ plasma and magnetic field instruments, but also EUV and magnetic imagers to study features in the solar atmosphere. One has to keep in mind, that the persistence models presented in this study rely on in-situ measurements obtained at just one point in interplanetary space and slightly different latitudes between the spacecraft may have essential impact on the forecast.

An additional study including the forecast of various solar parameters predicted by numerical models is performed. The big advantage of numerical models is that the solar wind parameters are predicted for the whole heliosphere usually up to 2 AU, making them a powerful tool to represent the general structure of the interplanetary space. We present the results of the newly developed EUHFORIA (EUropean Heliospheric FORecasting Information Asset) model, still under development within the CCSOM[11] project, in comparison to ACE in-situ measurements. Also the results of the already operational ENLIL model (provided by CCMS[12]) are compared to in-situ measurements. For EUHFORIA only a low number of model runs are available during four months (March to June) in 2008 and three months (March to May) in 2012 making it difficult to perform a statistical study. In addition, only the corresponding time ranges (CR 2067–2071 for the year 2008 and CR 2120–2124 for the year 2012) for the ENLIL model were used. Gressl et al. (2014) showed in their comparative study, that ENLIL runs using different input magnetograms result in different model outputs. Since EUHFORIA uses hourly updated synoptic GONG magnetograms, we decided to run the ENLIL also with GONG magnetograms, even though they are still in trial mode.

There exist already a couple of studies comparing ENLIL to in-situ measurements. Owens et al. (2008) used WSA/ENLIL and MAS/ENLIL models over the time period 1995 to 2002, ranging from low solar activity to high solar activity. The authors find a good model performance for the large scale structures with a systematic time offset of about two days. Also Lee et al. (2009) performed a study during the time of the

[10]http://swe.uni-graz.at/index.php/services/solar-wind-forecast-stereo-ch
[11]http://sidc.be/ccsom/
[12]https://ccmc.gsfc.nasa.gov/

declining phase of Solar Cycle 23 on the solar wind parameters modeled by 3D MHD models (MAS/ENLIL, WSA/ENLIL). They find an overall agreement between the observations and the model results for the general large-scale solar wind structures. They conclude that ENLIL can be used as a tool to analyze, and to some extent predict, the solar wind structure for the quiet solar periods.

EUHFORIA provides daily model runs, that span over 10 days. As a result, the outputs from consecutive days overlap (see Figure 5.4). In order to obtain a distinct time series, the individual curves have to be combined. We assume that the magnetic field information from the central region of the Sun has the least projection effects and are therefore most reliable. So by default, the time range used for the Gaussian weighting is set to ± 1 day and the central region is not shifted. However, we also want to evaluate how different settings affect the results. Therefore, the settings where the Gaussian weighting is extended to ± 2, ± 3, and ± 5 days is represented by: EUHFORIA (range: ± 2, ± 3, ± 5). EUHFORIA (shift: -2, -1, $+1$, $+2$) indicates that the central region is shifted according to -2 days, -1 day, $+1$ day, and $+2$ days.

The results obtained in this study show, that the EUHFORIA (shift: $+2$) model performs best for the continuous variables and the event-based values of solar wind speed. For all the other parameters (n, P, T, B_t, B_z) the EUHFORIA model with the default values seems to give the best results considering the year 2012. It should be noted, however, that the difference of the EUHFORIA models with the different settings are quite small. Regarding the solar wind speed continuous variables, we find that ENLIL performs better compared to EUHFORIA (shift: $+2$). This is true for the year 2012 ($\mathrm{RMSE}_{ENLIL} = 123$ km/s, $\mathrm{RMSE}_{EUHFORIA} = 129$ km/s) and especially for the year 2008 ($\mathrm{RMSE}_{ENLIL} = 102$ km/s, $\mathrm{RMSE}_{EUHFORIA} = 132$ km/s). In addition, less false alarms are found for the base level detection algorithm. ENLIL also gives better results for the density n, pressure P, temperature T, total magnetic field B_t, and the B_z component of the magnetic field. On the other hand, EUHFORIA gives better results for the peak detection for both time ranges in 2008 and 2012. The parameter which is best predicted by both numerical models is the solar wind bulk velocity v_b. For v_b the RMSE is about 30% of the mean solar wind speed (mean measurement). For all the other parameters, RMSE is in the order of the mean measurement or even higher. However, EUHFORIA generally underestimates the solar wind speed, whereas the density is overestimated. For future runs of the EUHFORIA model, these parameters should be adjusted and thoroughly tested to improve the forecasts. Interestingly, both EUHFORIA and ENLIL overestimate the solar wind speed in mid May 2008, which may be related to the input magnetogram. A detailed study on this period of time would be desired but is beyond the scope of this thesis.

Acknowledgments: We acknowledge the support by the CCSOM project funded by BELSPO (BRAIN-be). We thank the ACE SWEPAM and MAG instrument team and the ACE Science Center for providing the ACE data. SDO data are courtesy of the NASA/SDO and the AIA science team, STEREO data are courtesy of the NASA/STEREO and the IMPACT, PLASTIC, and SECCHI science teams, and SoHO/EIT data are courtesy of the SoHO science team.

List of abbreviations

ACE ..... Advanced Composition Explorer

AIA ..... Atmospheric Imaging Assembly onboard SDO

AU ..... Astronomical Unit

BS ..... Bias

CCMS .... Community Coordinated Modeling Center

CCSOM .. Constraining CMEs and Shocks by Observations and Modelling

CH ..... Coronal Hole

CIR ..... Co-rotating Interaction Region

CME ..... Coronal Mass Ejection

DSCOVR Deep Space Climate Observatory

EIT ..... Extreme ultraviolet Imaging Telescope onboard SoHO

ESWF .... Empirical Solar Wind Forecast

EUHFORIA EUropean Heliospheric FORecasting Information Asset

EUV ..... Extreme UltraViolet

FAR ..... False Alarm Ratio

FN ..... False Negative, correct rejection

FN ..... False Negative, miss

FP ..... False Positive, false alarm

GONG ... Global Oscillation Network Group

HEEQ .... Heliocentric Earth Equatorial

HSS ..... High-Speed Streams

ICME .... Interplanetary Coronal Mass Ejection

IMF ..... Interplanetary Magnetic Field

IMPACT . In-situe Measurements of Particles and CME Transients onboard STEREO

MAD ..... Mean Absolute Deviation

MAE ..... Mean Absolute Error

MAG ..... MAGnetic field experiment onboard ACE

MAS ..... Magnetohydrodynamics Around Sphere

ME ..... Mean Error

MHD ..... MagnetoHydroDynamic

NASA .... National Aeronautics and Space Administration

NOAA ... National Oceanographic and Atmospheric Association

PFSS ..... Potential Field Source Surface

PlasMag . Solar Wind Plasma Sensor and Magnetometer onboard DSCOVR

PLASTIC PLAsma and SupraThermal Ion Composition onboard STEREO

POD ..... Probability Of Detection

RMSE .... Root Mean Square Error

RUS ..... Ratio of Underestimated Speed

SCS ..... Schatten Current Sheet

SDO ..... Solar Dynamcis Observatory

SECCHI . Sun Earth Connection Coronal and Heliospheric Investigation onboard STEREO

SIR ..... Stream Interaction Region

SoHO ..... Solar and Heliospheric Observatory

STEREO . Solar TErrestrial RElations Observatory

SWEPAM Solar Wind Electron, Proton and Alpha Monitor onboard ACE

SXR ..... Soft X-Ray

TP ..... True Positive, hit

TS ..... Thread Score

TVDLF .. Total Variation-Diminishing Lax-Friedrich

WSA ..... Wang-Sheeley-Arge

List of Figures

List of Tables

A. Appendix Figures of the modeled solar wind parameters

The figures for the modeled solar wind speeds in comparison to the in-situ measurements, with and without rejecting the times of CME occurrences according to the catalogs of Richardson & Cane for ACE and L. Jian for STEREO-B, are shown. The measurement is represented by the orange curve and the forecast by the blue curve. The total number of detected peaks or base levels in the measurements (pink triangle) and the forecasts (blue triangle) and also the number of hits (blue crosses), false alarms (red circles) and misses (red crosses) are listed. Black dots above or below the hits indicate whether the solar wind speed was under- or overestimated.

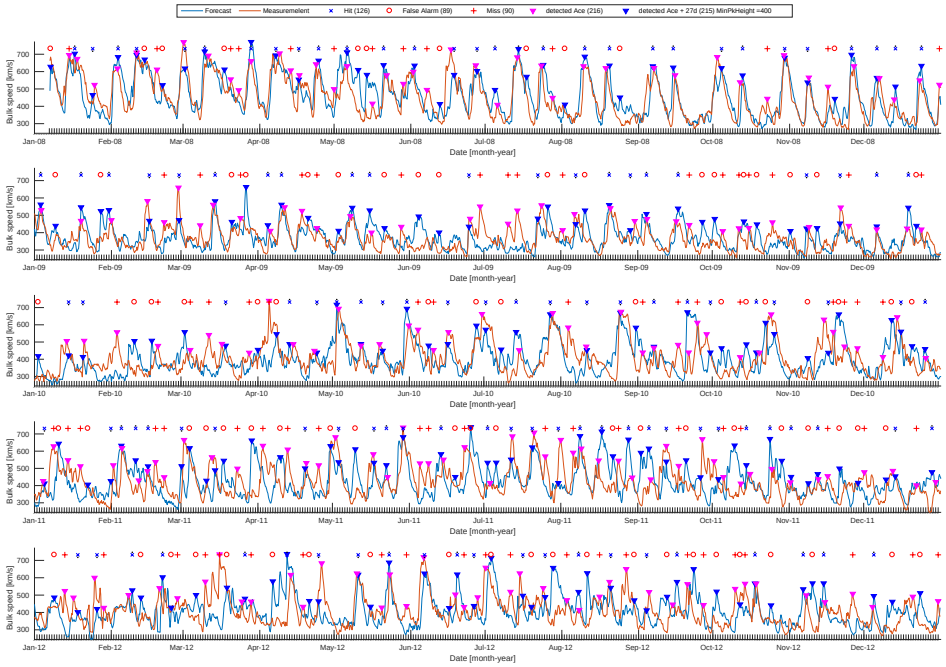

Figure A.1.: Persistence model 27d (CMEs rejected) for the peak detection.

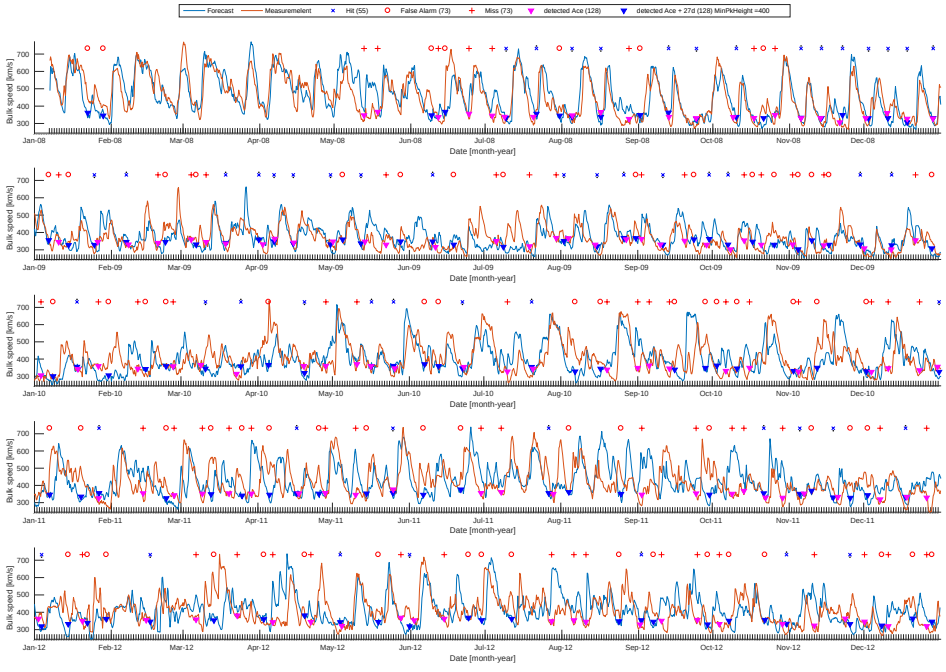

Figure A.2.: Persistence model 27d (CMEs rejected) for the base level detection.

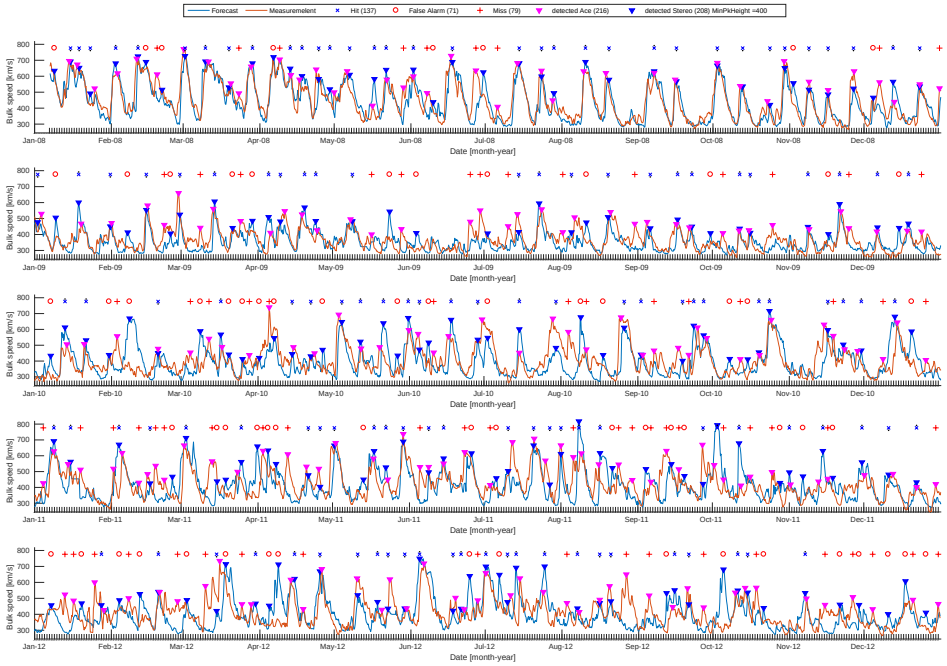

Figure A.3.: Persistence model STEREO (CMEs rejected) for the peak detection.

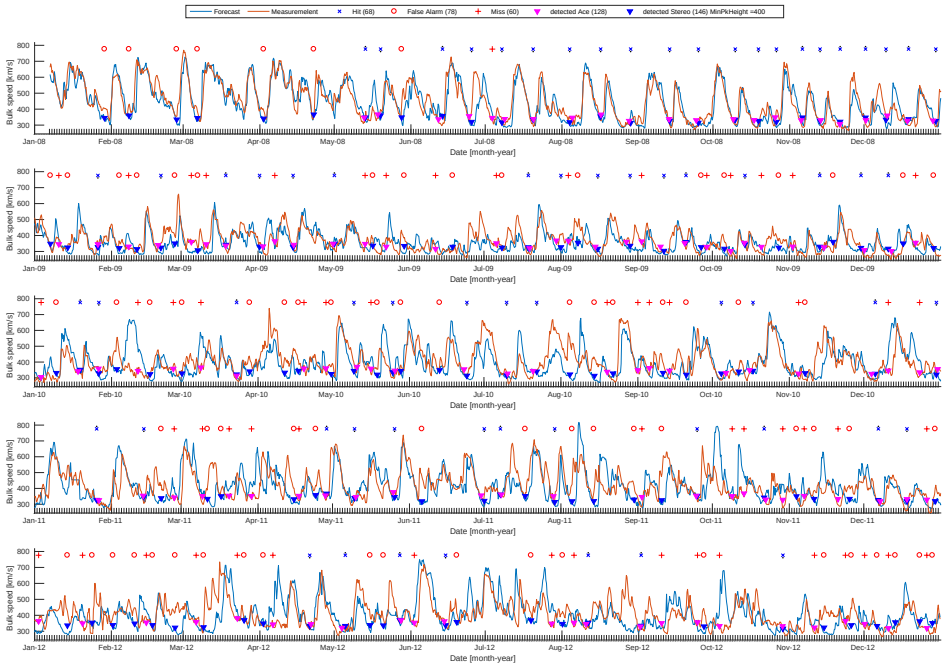

Figure A.4.: Persistence model STEREO (CMEs rejected) for the base level detection.

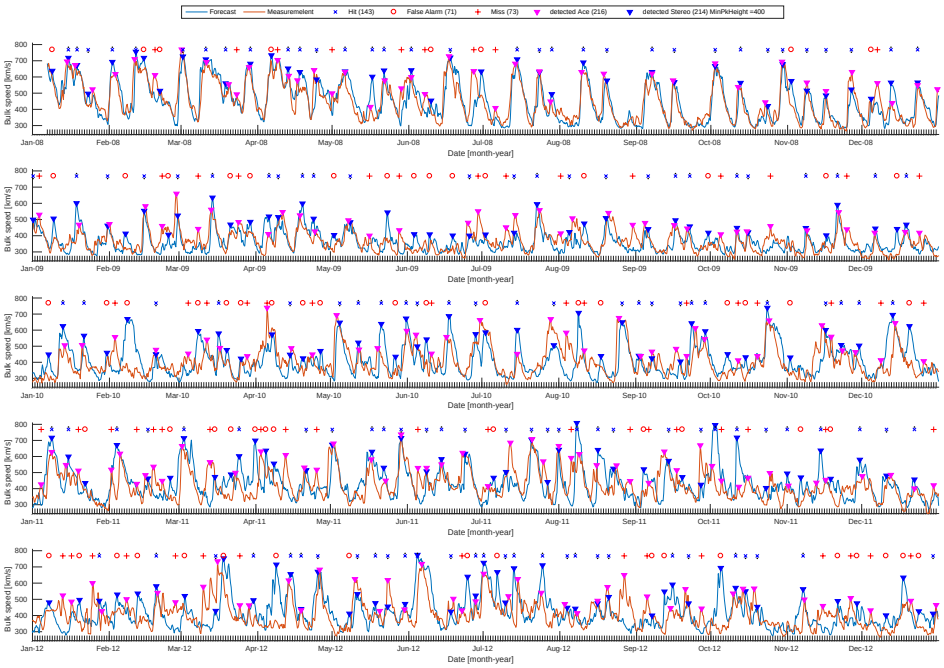

Figure A.5.: Persistence model STEREO+CH_V1 (CMEs rejected) for the peak detection.

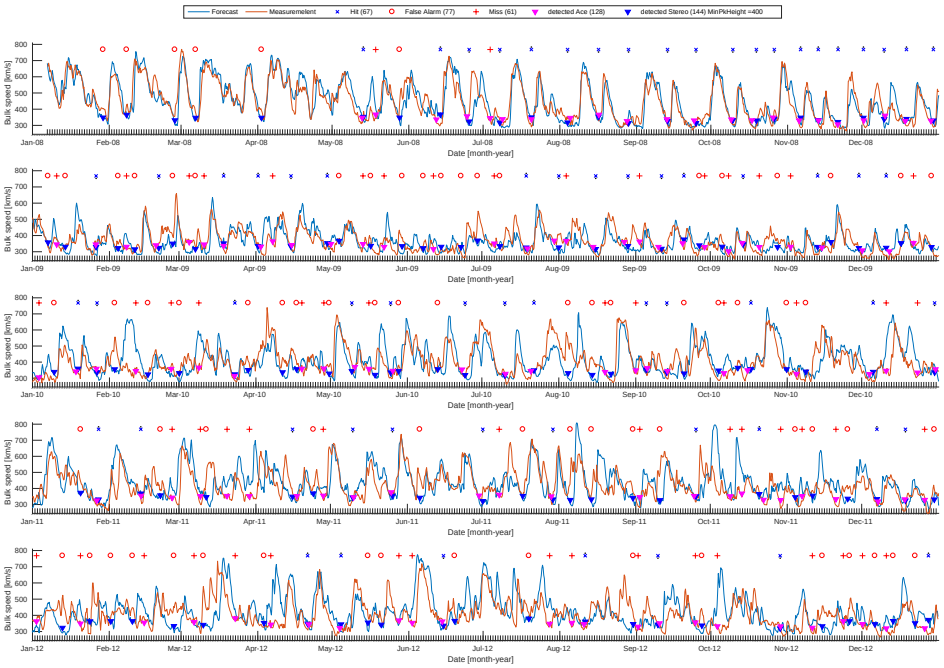

Figure A.6.: Persistence model STEREO+CH_V1 (CMEs rejected) for the base level detection.

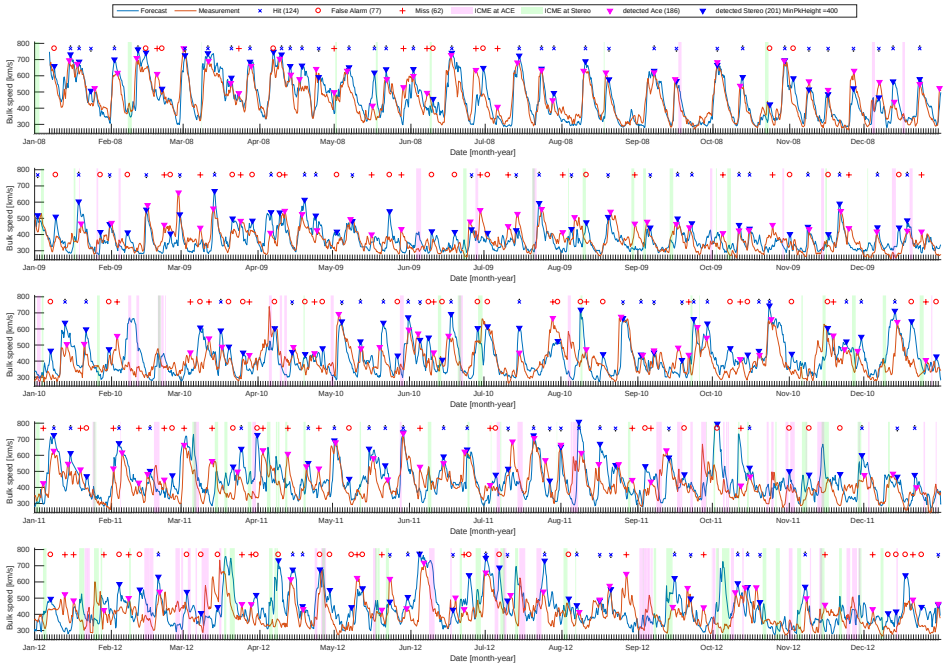

Figure A.7.: Persistence model STEREO+CH_V2 for the peak detection.

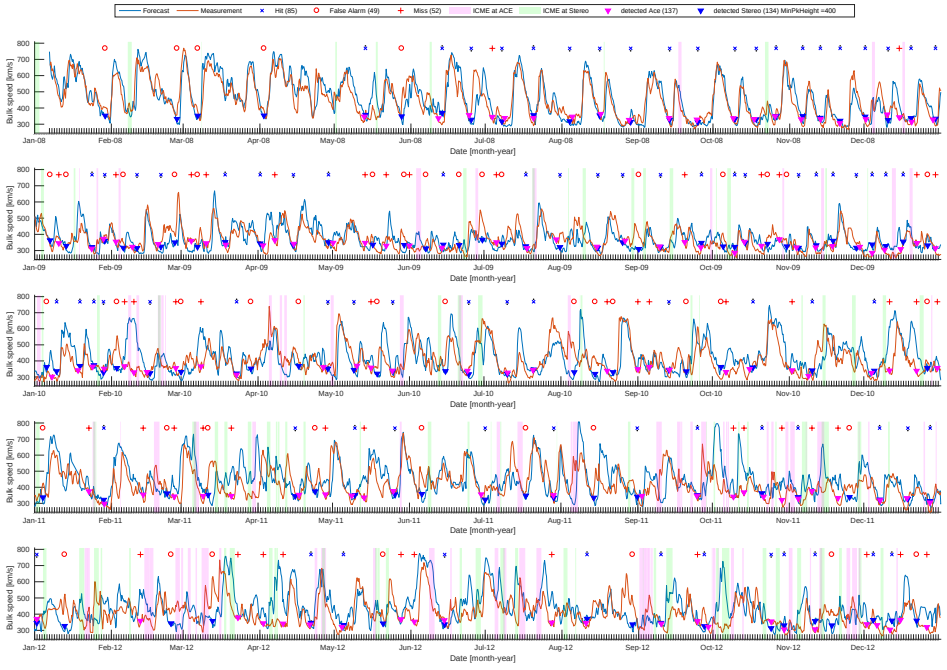

Figure A.8.: Persistence model STEREO+CH_V2 for the base level detection.

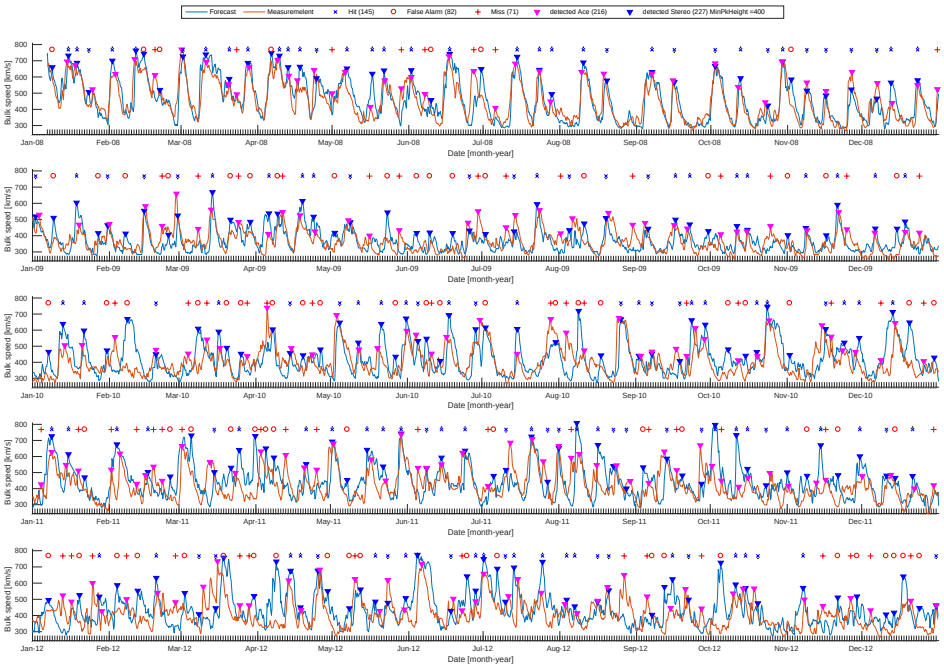

Figure A.9.: Persistence model STEREO+CH_V2 (CMEs rejected) for the peak detection.

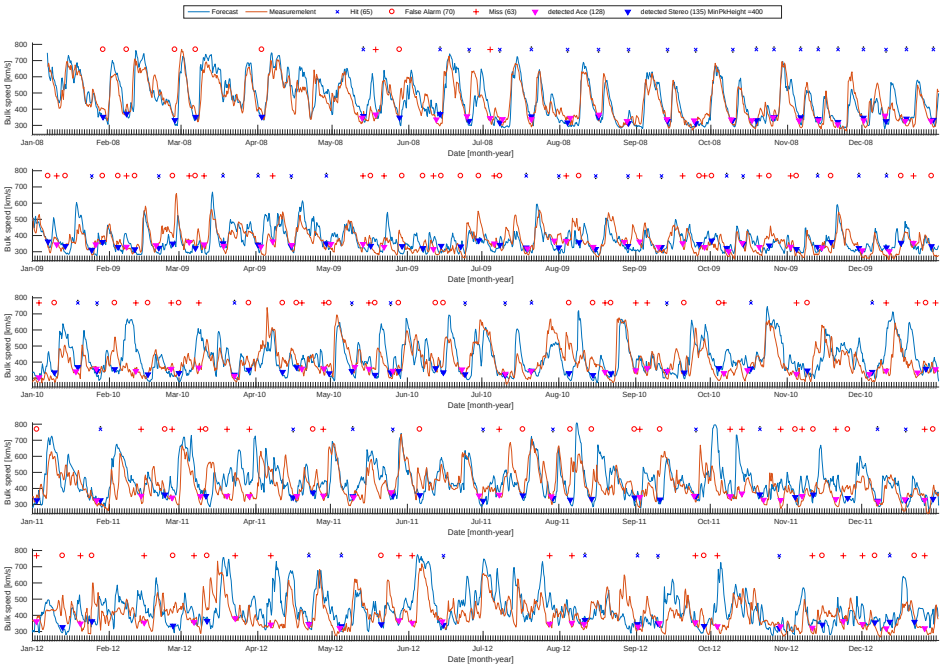

Figure A.10.: Persistence model STEREO+CH_V2 (CMEs rejected) for the base level detection.

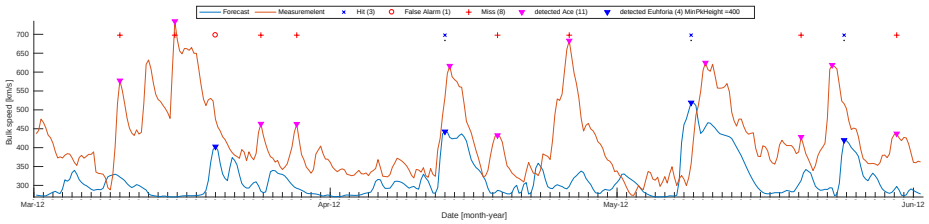

Figure A.11.: EUHFORIA model with the default settings and CMEs rejected for 2012.

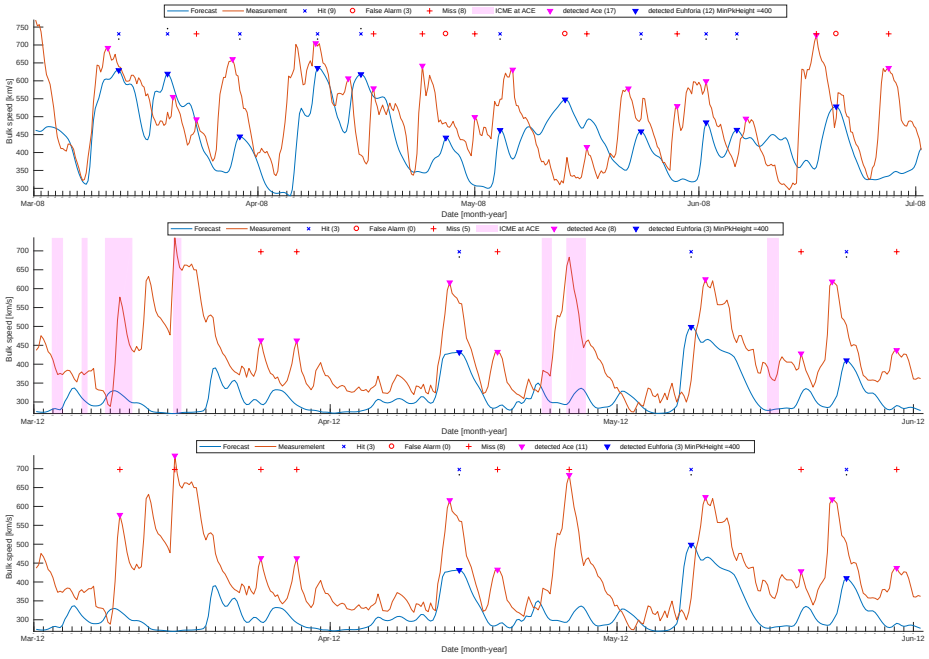

Figure A.12.: EUHFORIA model with a selected range for the Gaussian of ± 2 days for the peaks. Top panel: 2008, Middle panel: 2012 (CME rejected), Bottom panel: 2012 (CME not rejected).

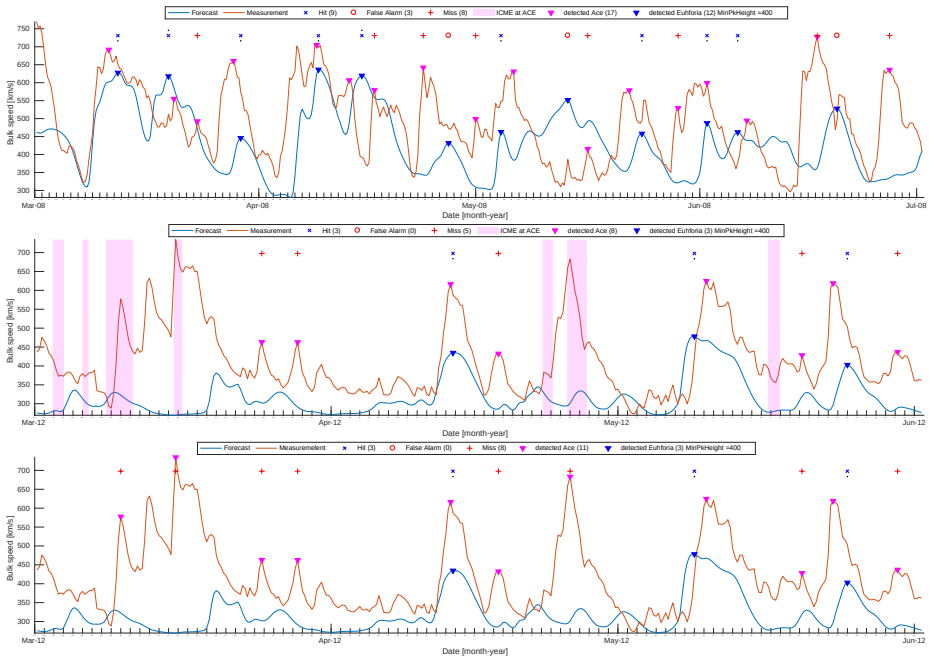

Figure A.13.: EUHFORIA model with a selected range for the Gaussian of ±3 days for the peaks. Top panel: 2008, Middle panel: 2012 (CME rejected), Bottom panel: 2012 (CME not rejected).

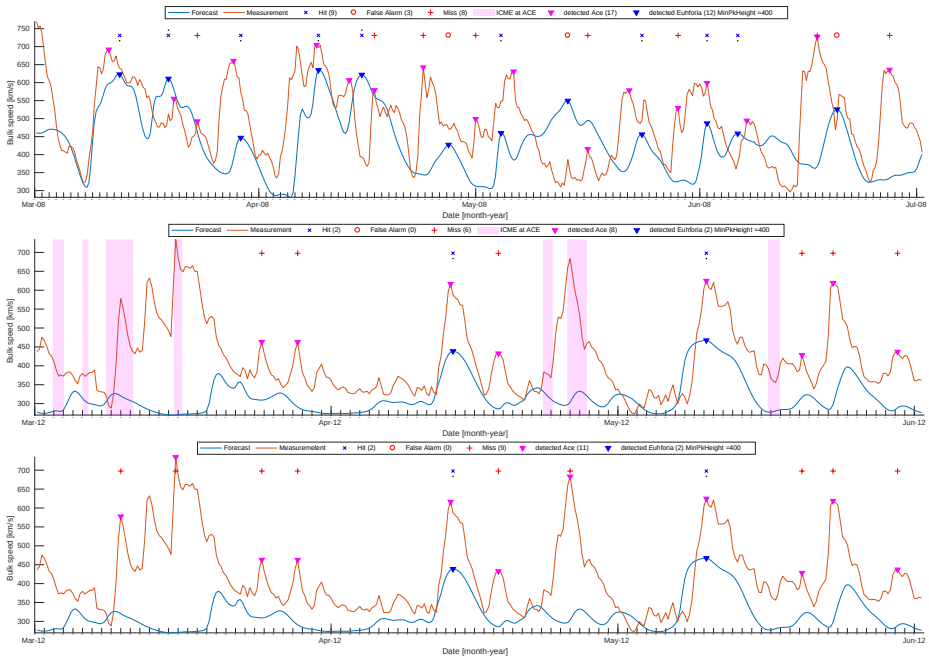

Figure A.14.: EUHFORIA model with a selected range for the Gaussian of ±5 days for the peaks. Top panel: 2008, Middle panel: 2012 (CME rejected), Bottom panel: 2012 (CME not rejected).

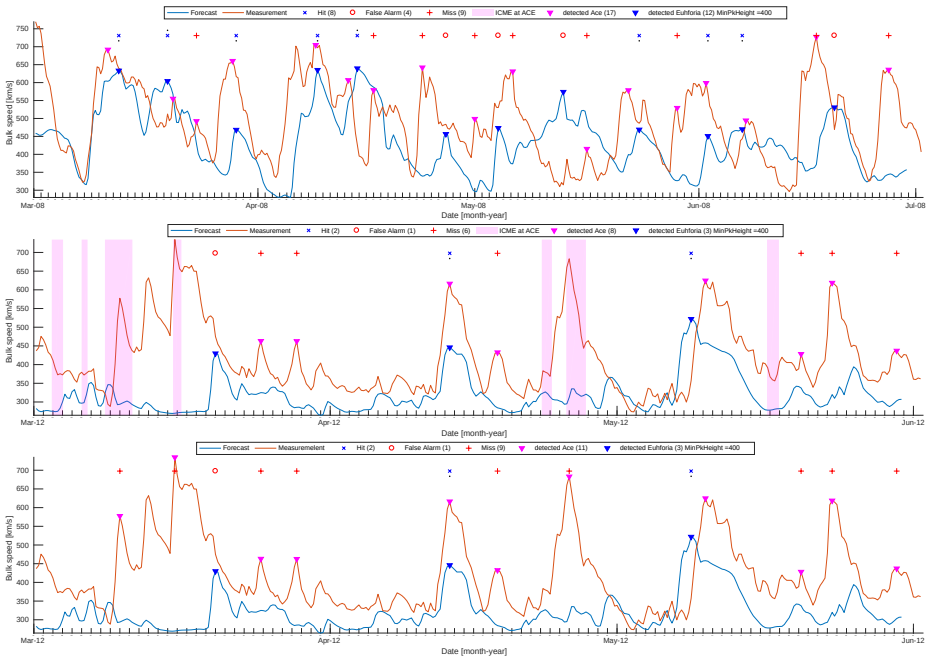

Figure A.15.: EUHFORIA model with the central region shifted to −2 days for the peaks. Top panel: 2008, Middle panel: 2012 (CME rejected), Bottom panel: 2012 (CME not rejected).

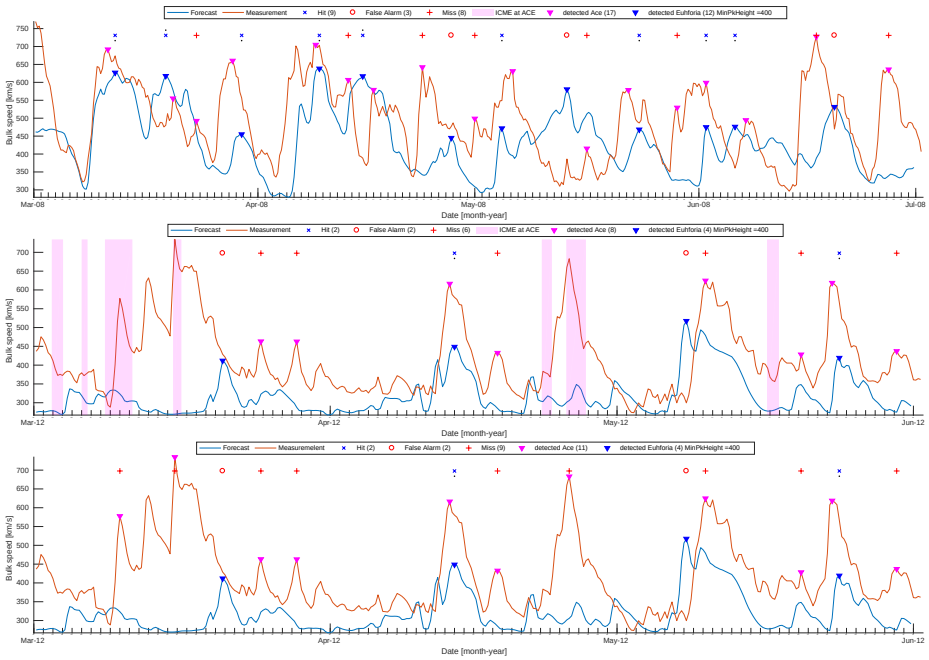

Figure A.16.: EUHFORIA model with the central region shifted to −1 days for the peaks. Top panel: 2008, Middle panel: 2012 (CME rejected), Bottom panel: 2012 (CME not rejected).

Figure A.17.: EUHFORIA model with the central region shifted to +1 days for the peaks. Top panel: 2008, Middle panel: 2012 (CME rejected), Bottom panel: 2012 (CME not rejected).

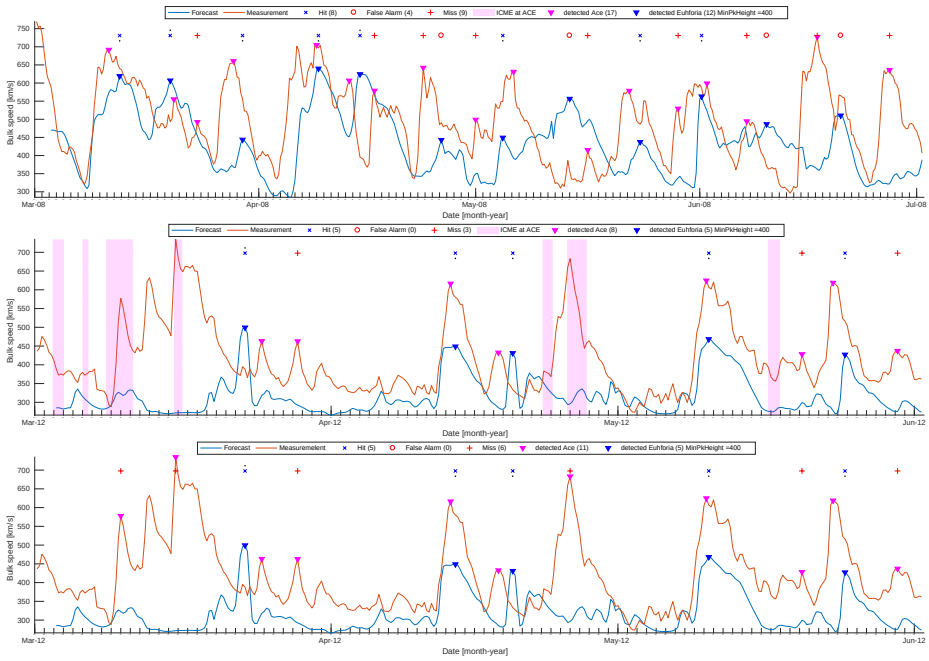

Figure A.18.: EUHFORIA model with the central region shifted to +2 days for the peaks. Top panel: 2008, Middle panel: 2012 (CME rejected), Bottom panel: 2012 (CME not rejected).

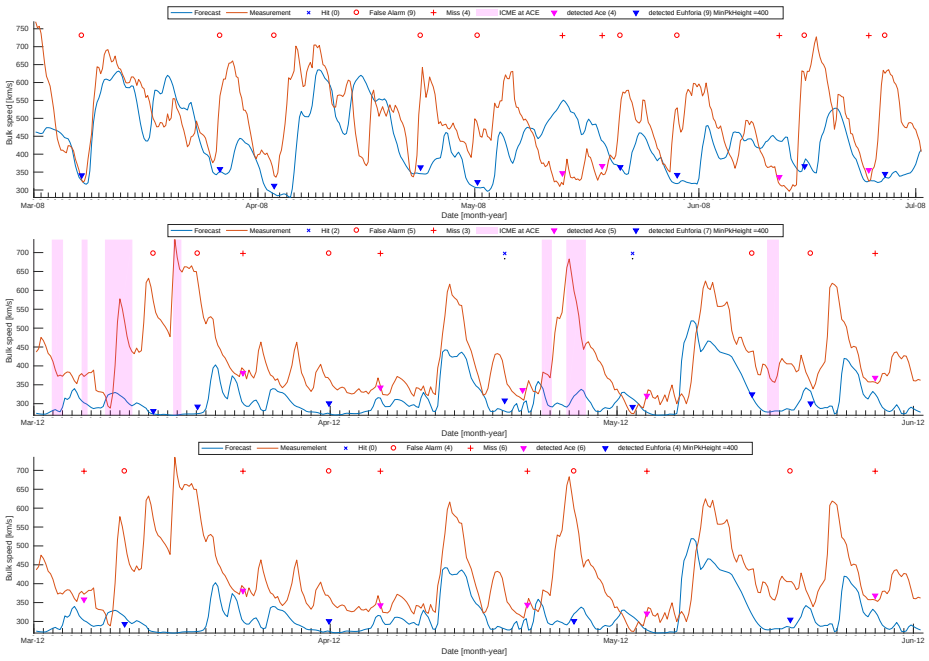

Figure A.19.: EUHFORIA model with a selected range for the Gaussian of ±1 days for the base levels. Top panel: 2008, Middle panel: 2012 (CME rejected), Bottom panel: 2012 (CME not rejected).

Figure A.20.: EUHFORIA model with a selected range for the Gaussian of ±2 days for the base levels. Top panel: 2008, Middle panel: 2012 (CME rejected), Bottom panel: 2012 (CME not rejected).

Figure A.21.: EUHFORIA model with a selected range for the Gaussian of ±3 days for the base levels. Top panel: 2008, Middle panel: 2012 (CME rejected), Bottom panel: 2012 (CME not rejected).

Figure A.22.: EUHFORIA model with a selected range for the Gaussian of ±5 days for the base levels. Top panel: 2008, Middle panel: 2012 (CME rejected), Bottom panel: 2012 (CME not rejected).

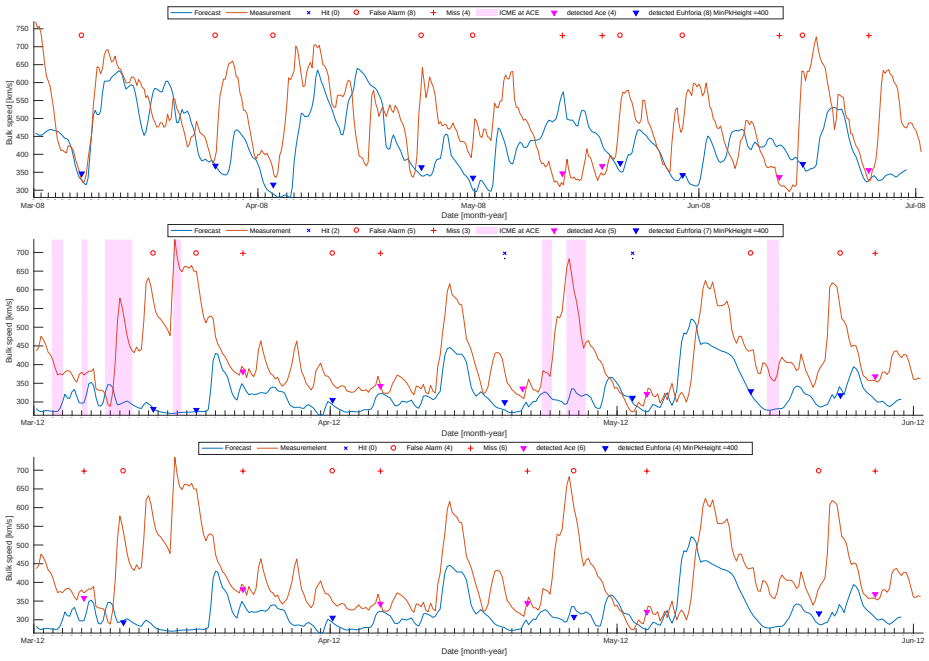

Figure A.23.: EUHFORIA model with the central region shifted to −2 days for the base levels. Top panel: 2008, Middle panel: 2012 (CME rejected), Bottom panel: 2012 (CME not rejected).

Figure A.24.: EUHFORIA model with the central region shifted to −1 days for the base levels. Top panel: 2008, Middle panel: 2012 (CME rejected), Bottom panel: 2012 (CME not rejected).

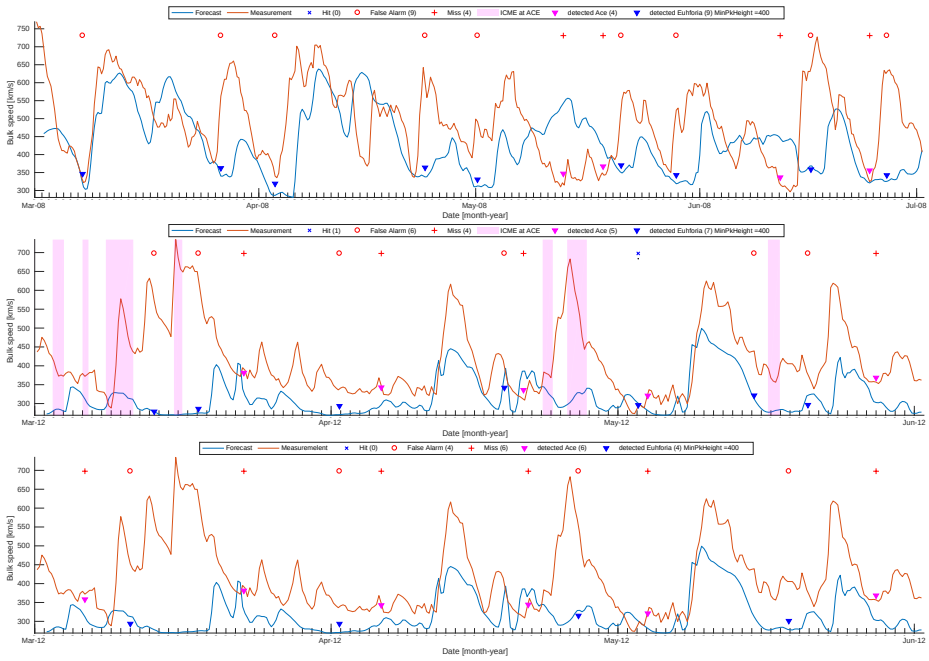

Figure A.25.: EUHFORIA model with the central region shifted to +1 days for the base levels. Top panel: 2008, Middle panel: 2012 (CME rejected), Bottom panel: 2012 (CME not rejected).

Figure A.26.: EUHFORIA model with the central region shifted to +2 days for the base levels. Top panel: 2008, Middle panel: 2012 (CME rejected), Bottom panel: 2012 (CME not rejected).

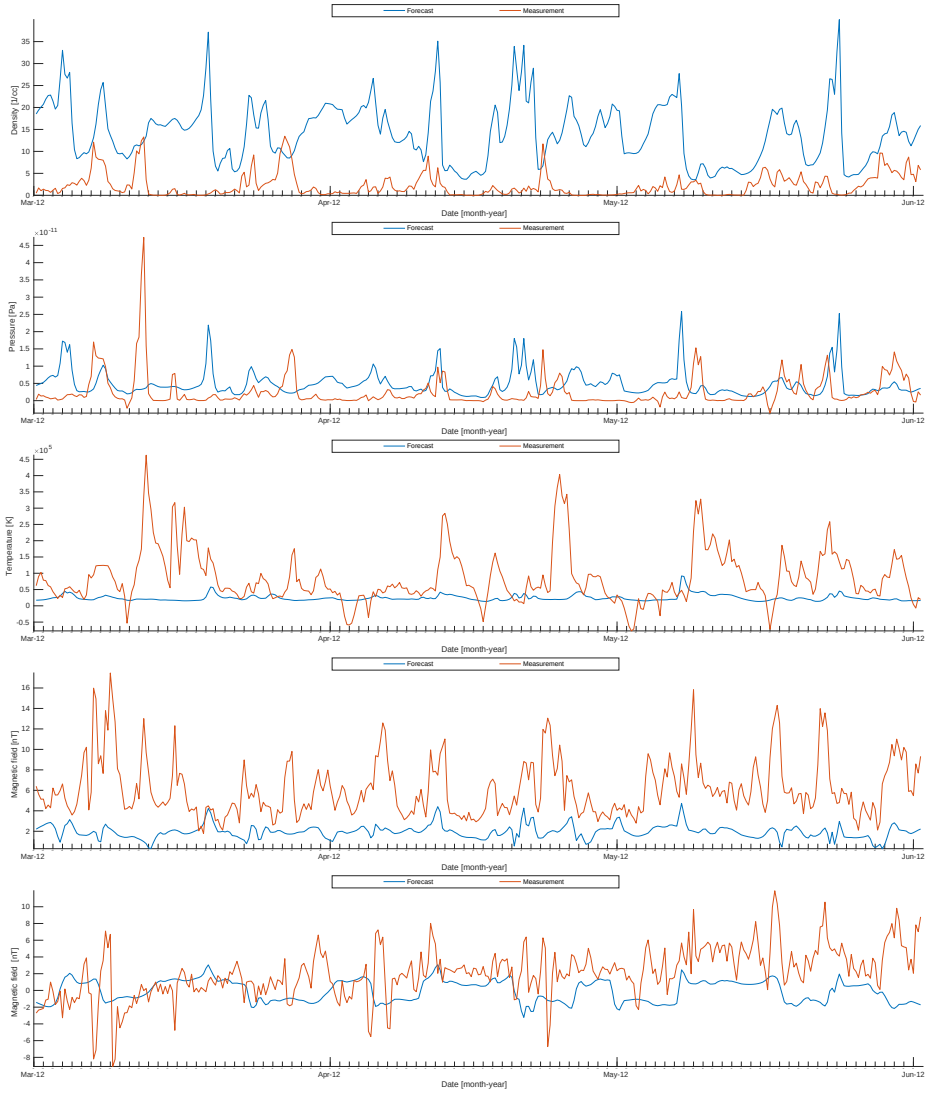

Figure A.27.: EUHFORIA modeled solar wind parameter (blue curve) compared to ACE in-situ measurements (orange curve) for 2012 with CMEs not rejected. From top to bottom: density, pressure, temperature, total magnetic field, B_z component of the magnetic field.

Figure A.28.: Solar wind density obtained by ACE (orange curve) for 2008 (top), 2012 (CME rejected, middle), and 2012 (CME not rejected, bottom) in comparison to the EUHFORIA density forecast where the central region is shifted to +2 days.

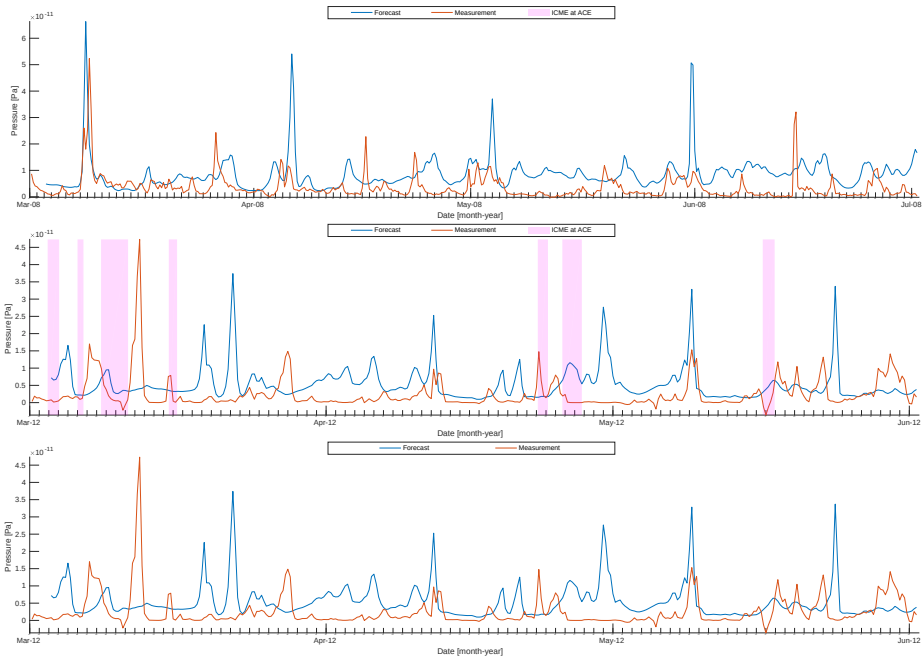

Figure A.29.: Solar wind pressure obtained by ACE (orange curve) for 2008 (top), 2012 (CME rejected, middle), and 2012 (CME not rejected, bottom) in comparison to the EUHFORIA pressure forecast where the central region is shifted to +2 days.

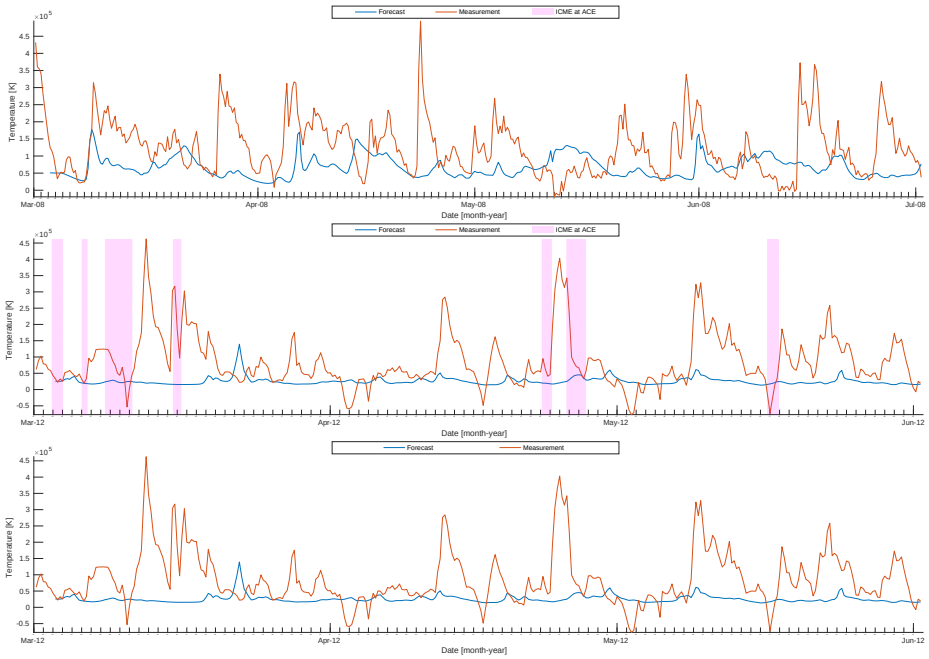

Figure A.30.: Solar wind temperature obtained by ACE (orange curve) for 2008 (top), 2012 (CME rejected, middle), and 2012 (CME not rejected, bottom) in comparison to the EUHFORIA temperature with the central region is shifted to +2 days.

Figure A.31.: Solar wind total magnetic field obtained by ACE (orange curve) for 2008 (top), 2012 (CME rejected, middle), and 2012 (CME not rejected, bottom) in comparison to the EUHFORIA total magnetic field forecast where the central region is shifted to +2 days.

Figure A.32.: Solar wind B_z obtained by ACE (orange curve) for 2008 (top), 2012 (CME rejected, middle), and 2012 (CME not rejected, bottom) in comparison to the EUHFORIA B_z forecast where the central region is shifted to +2 days.

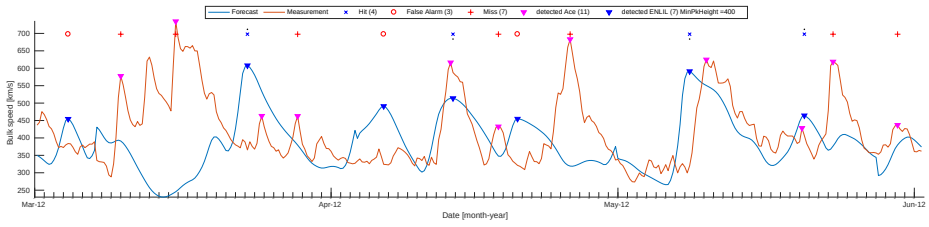

Figure A.33.: ENLIL model with the default settings and CMEs rejected for 2012.

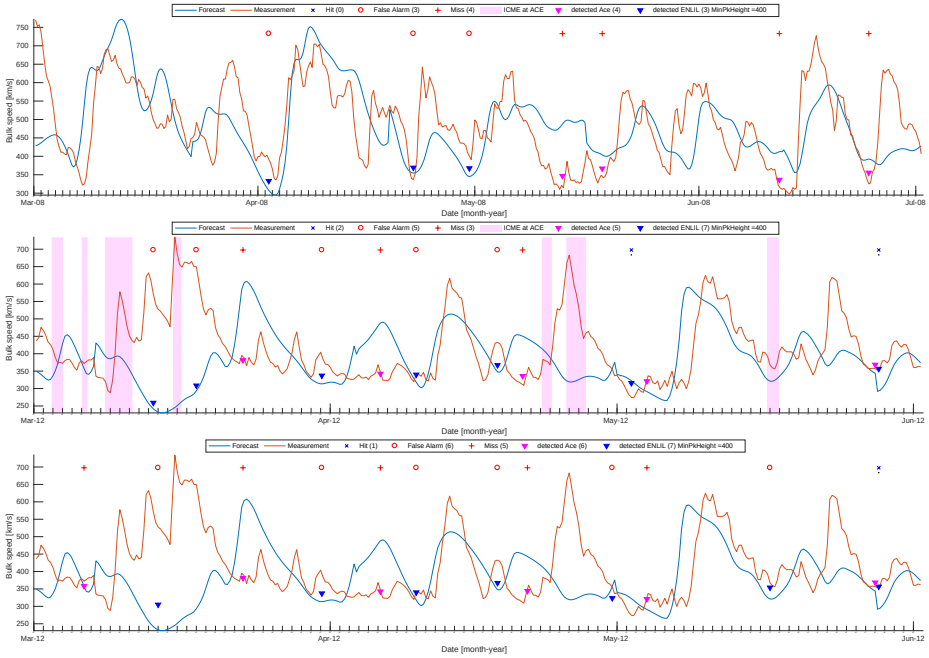

Figure A.34.: ENLIL model results for the base levels. Top panel: 2008, Middle panel: 2012 (CME rejected), Bottom panel: 2012 (CME not rejected).

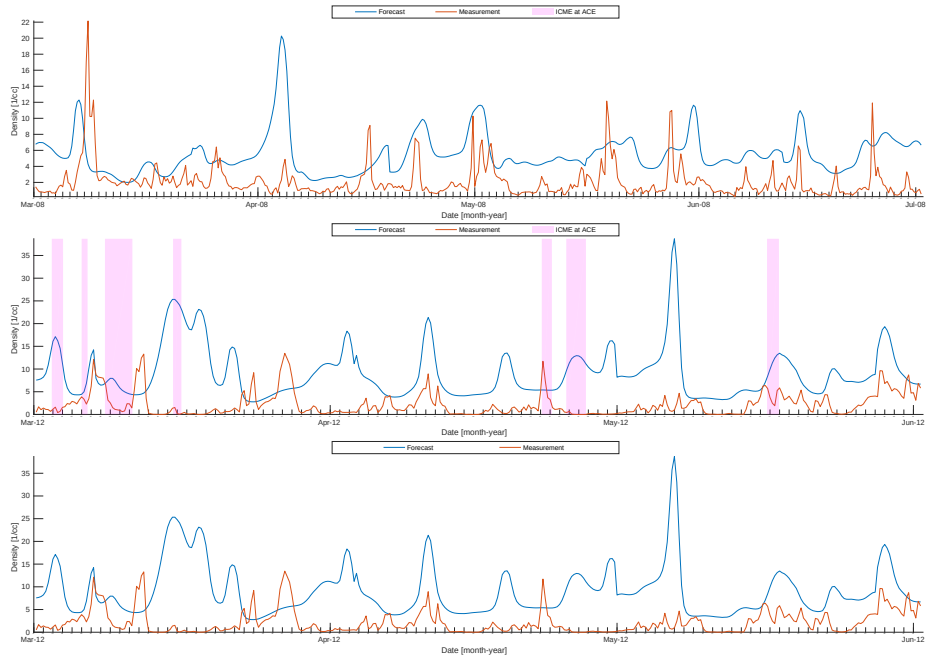

Figure A.35.: Solar wind density obtained by ACE (orange curve) for 2008 (top), 2012 (CME rejected, middle), and 2012 (CME not rejected, bottom) in comparison to the ENLIL solar wind density forecast.

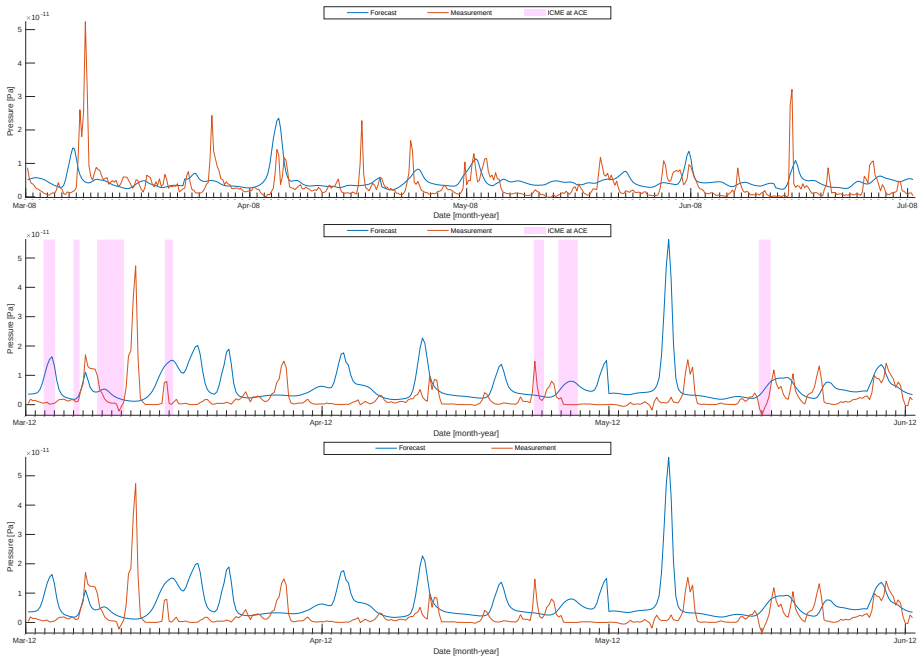

Figure A.36.: Solar wind pressure obtained by ACE (orange curve) for 2008 (top), 2012 (CME rejected, middle), and 2012 (CME not rejected, bottom) in comparison to the ENLIL solar wind pressure forecast.

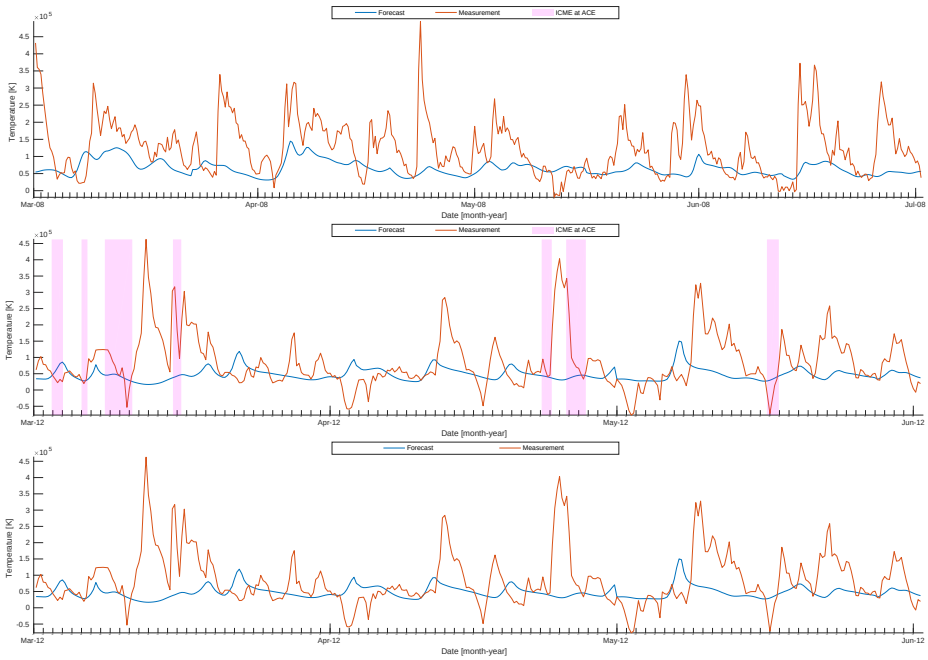

Figure A.37.: Solar wind temperature obtained by ACE (orange curve) for 2008 (top), 2012 (CME rejected, middle), and 2012 (CME not rejected, bottom) in comparison to the ENLIL solar wind temperature forecast.

Figure A.38.: Solar wind total magnetic field obtained by ACE (orange curve) for 2008 (top), 2012 (CME rejected, middle), and 2012 (CME not rejected, bottom) in comparison to the ENLIL solar wind total magnetic field forecast.

Figure A.39.: Solar wind B_z obtained by ACE (orange curve) for 2008 (top), 2012 (CME rejected, middle), and 2012 (CME not rejected, bottom) in comparison to the ENLIL solar wind B_z forecast.

B. Appendix Results tables

The tables containing the continuous variables and the event-based statistics are listed. YES means that the CMEs occurrences are included in the statistical analysis and NO means that CMEs are excluded from the statistical analysis. ME is the mean error, MAE the mean average error and RMSE is the root-mean-square error. Mean M is the mean and Std M the standard deviation calculated for the measured time series, and Mean F and Std F are the mean and standard deviation of the forecasts. TP are the hits, FP the false alarms and FN the misses. FAR is the false alarm ratio, TS the threat score (best: TS = 1, worst: TS = 0), BS the bias (BS $<$ 1 underestimation, BS $>$ 1 overestimation) and POD the probability of detection. RUS gives the ratio of underestimated speed. Mean dt and Std dt represent the mean and standard deviation of the time difference (dt) in the forecast and the measurement [hours] calculated for hits only. Also the mean and standard deviation of the speed differences (dv) in the measured and predicted solar wind speed [km/s] is calculated. For EUHFORIA default means that the time range used for the Gaussian weighting is set to $\pm$1 day and the central region is not shifted, otherwise the exact time range [days] for the Gaussian weighting is given or the shift of the central region [days].

Table B.1.: Statistical results of the continuous variables for the solar wind speed [km/s] covering the time range January 2008 to December 2012.

Persistence model	ME	MAE	RMSE	Mean M	Std M	Mean F	Std F
27d/YES (eg. Fig. A.1)	−1.84	67.32	90.23	411.08	93.67	412.92	94.53
27d/NO (eg. Fig. 6.1)	−2.36	66.03	88.31	411.97	94.83	414.33	96.22
STEREO/YES (eg. Fig. A.3)	8.69	59.46	82.71	411.08	93.67	402.39	99.02
STEREO/NO (eg. Fig. 6.3)	9.79	57.15	79.28	411.94	95.08	402.15	99.71
STEREO+CH_V1/YES (eg. Fig. A.5)	−5.12	60.45	83.25	411.08	93.67	416.20	102.31
STEREO+CH_V1/NO (eg. Fig. 6.5)	−3.86	57.99	79.62	411.94	95.08	415.80	103.05
STEREO+CH_V2/YES (eg. Fig. A.9)	−14.38	63.45	86.61	411.08	93.67	425.46	105.77
STEREO+CH_V2/NO (eg. Fig. A.7)	−12.92	61.02	82.92	411.94	95.08	424.85	106.48

Table B.2.: Event-based statistics for the peaks and base levels detected in the time range January 2008 to December 2012.

Persistence model	TP	FP	FN	FAR	TS	BS	POD	RUS	Mean dt	Std dt	Mean dv	Std dv
Peak detection												
27d/YES (Fig. A.1)	126	89	90	0.42	0.41	1.00	0.59	0.45	-0.04	0.95	−1.93	91.21
27d/NO (Fig. 6.1)	111	79	81	0.42	0.41	0.99	0.58	0.46	-0.00	0.93	0.46	86.60
STEREO/YES (Fig. A.3)	137	71	79	0.37	0.48	0.96	0.66	0.47	-0.02	0.93	2.65	84.39
STEREO/NO (Fig. 6.3)	119	61	67	0.36	0.48	0.97	0.66	0.45	0.07	0.89	3.72	69.41
STEREO+CH_V1/YES (Fig. A.5)	143	71	73	0.34	0.50	0.99	0.67	0.44	0.06	0.91	12.93	84.51
STEREO+CH_V1/NO (Fig. 6.5)	124	64	62	0.33	0.50	1.01	0.66	0.42	0.11	0.86	13.50	71.35
STEREO+CH_V2/YES (Fig. A.9)	145	82	71	0.33	0.49	1.05	0.64	0.36	0.00	0.90	25.62	85.90
STEREO+CH_V2/NO (Fig. A.7)	124	77	62	0.33	0.47	1.08	0.62	0.32	0.10	0.84	28.44	70.99
Base level detection												
27d/YES (Fig. A.2)	55	73	73	0.57	0.27	1.00	0.43	0.47	-0.09	1.06	0.78	20.99
27d/NO (Fig. 6.2)	64	70	71	0.53	0.31	0.99	0.48	0.48	-0.17	0.81	−0.47	23.13
STEREO/YES (Fig. A.4)	68	78	60	0.47	0.33	1.14	0.47	0.63	0.20	0.90	−7.49	15.94
STEREO/NO (Fig. 6.4)	96	62	41	0.30	0.48	1.15	0.61	0.60	0.20	0.84	−5.77	21.93
STEREO+CH_V1/YES (Fig. A.6)	67	77	61	0.48	0.33	1.12	0.47	0.55	0.17	0.92	−2.33	18.30
STEREO+CH_V1/NO (Fig. 6.6)	93	58	44	0.32	0.48	1.10	0.62	0.48	0.21	0.84	1.54	21.87
STEREO+CH_V2/YES (Fig. A.10)	65	70	63	0.49	0.33	1.05	0.48	0.49	0.15	0.95	−1.06	18.25
STEREO+CH_V2/NO (Fig. A.8)	85	49	52	0.38	0.46	0.98	0.63	0.45	0.19	0.83	3.70	21.32

Table B.3.: Statistical results of the continuous variables for the solar wind speed [km/s] modeled by EUHFORIA and ENLIL covering the time range March to June 2008.

Model	ME	MAE	RMSE	Mean M	Std M	Mean F	Std F
EUHFORIA (default) (Fig. 6.7)	57.86	106.43	135.36	492.40	104.95	434.54	89.23
EUHFORIA (range: ±2) (Fig. A.12)	57.99	106.33	135.21	492.40	104.95	434.42	88.76
EUHFORIA (range: ±3) (Fig. A.13)	58.13	106.26	135.01	492.40	104.95	434.27	88.17
EUHFORIA (range: ±5) (Fig.A.14)	58.56	105.96	134.34	492.40	104.95	433.85	86.61
EUHFORIA (shift: -2) (Fig. A.15)	57.98	106.13	134.94	492.40	104.95	434.43	86.94
EUHFORIA (shift: -1) (Fig. A.16)	57.21	106.88	134.87	492.40	104.95	435.19	89.52
EUHFORIA (shift: +1) (Fig. A.17)	59.25	106.03	135.14	492.40	104.95	433.16	88.87
EUHFORIA (shift: +2) (Fig. A.18)	59.03	103.98	132.03	492.40	104.95	433.38	86.56
ENLIL (Fig. 6.8)	6.71	81.60	101.78	492.40	104.95	485.70	100.39

Table B.4.: Statistical results of the continuous variables for the solar wind speed [km/s] modeled by EUHFORIA and ENLIL covering the time range March to June 2012.

Model	ME	MAE	RMSE	Mean M	Std M	Mean F	Std F
EUHFORIA/YES (default) (Fig. 6.7)	102.34	108.75	140.22	417.76	95.25	315.42	52.07
EUHFORIA/NO (default) (Fig. 6.7)	96.11	102.86	131.60	413.00	90.63	316.90	54.38
EUHFORIA/YES (range: ±2) (Fig. A.12)	101.67	107.27	138.83	417.76	95.25	316.09	50.04
EUHFORIA/NO (range: ±2) (Fig. A.12)	95.42	101.27	130.06	413.00	90.63	317.58	52.22
EUHFORIA/YES (range: ±3) (Fig. A.13)	101.09	106.16	137.89	417.76	95.25	316.67	48.65
EUHFORIA/NO (range: ±3) (Fig. A.13)	94.83	100.08	129.02	413.00	90.63	318.18	50.73
EUHFORIA/YES (range: ±5) (Fig. A.14)	100.32	104.77	136.98	417.76	95.25	317.45	47.00
EUHFORIA/NO (range: ±5) (Fig. A.14)	93.99	98.62	128.01	413.00	90.63	319.01	48.96
EUHFORIA/YES (shift: -2) (Fig. A.15)	97.67	106.01	138.90	417.76	95.25	320.09	51.00
EUHFORIA/NO (shift: -2) (Fig. A.15)	90.88	99.29	129.51	413.00	90.63	322.12	53.07
EUHFORIA/YES (shift: -1) (Fig. A.16)	99.05	107.40	139.08	417.76	95.25	318.71	51.48
EUHFORIA/NO (shift: -1) (Fig. A.16)	92.55	101.31	130.45	413.00	90.63	320.46	53.60
EUHFORIA/YES (shift: +1) (Fig. A.17)	99.80	104.67	136.16	417.76	95.25	317.96	50.92
EUHFORIA/NO (shift: +1) (Fig. A.17)	93.64	98.67	127.12	413.00	90.63	319.37	53.16
EUHFORIA/YES (shift: +2) (Fig. A.18)	99.31	104.88	137.76	417.76	95.25	318.45	50.54
EUHFORIA/NO (shift: +2) (Fig. A.18)	93.03	99.10	128.90	413.00	90.63	319.98	52.61
ENLIL/YES (Fig. 6.8)	30.36	93.91	130.73	417.76	95.25	387.40	79.37
ENLIL/NO (Fig. 6.8)	21.38	89.38	122.77	413.00	90.63	391.62	81.58

Table B.5.: Event-based statistics for the peaks of the solar wind speed [km/s] modeled by EUHFORIA and ENLIL covering the time range March to June 2008.

Model	TP	FP	FN	FAR	TS	BS	POD	RUS	Mean dt	Std dt	Mean dv	Std dv
EUHFORIA (default) (Fig. 6.7)	9	3	8	0.47	0.45	0.71	0.75	0.78	0.28	1.33	−78.45	88.05
EUHFORIA (range: ±2) (Fig. A.12)	9	3	8	0.47	0.45	0.71	0.75	0.78	0.28	1.32	−78.36	87.44
EUHFORIA (range: ±3) (Fig. A.13)	9	3	8	0.47	0.45	0.71	0.75	0.78	0.25	1.29	−78.22	86.68
EUHFORIA (range: ±5) (Fig. A.14)	9	3	8	0.47	0.45	0.71	0.75	0.78	0.28	1.32	−80.34	85.65
EUHFORIA (shift: −2) (Fig. A.15)	8	4	9	0.53	0.38	0.71	0.67	0.75	0.50	0.87	−65.06	83.90
EUHFORIA (shift: −1) (Fig. A.16)	9	3	8	0.47	0.45	0.71	0.75	0.78	-0.14	1.26	−71.95	88.62
EUHFORIA (shift: +1) (Fig. A.17)	8	3	9	0.53	0.40	0.65	0.73	0.75	0.53	1.18	−79.52	91.76
EUHFORIA (shift: +2) (Fig. A.18)	8	4	9	0.53	0.38	0.71	0.67	0.75	0.41	1.20	−80.42	94.06
ENLIL (Fig. 6.8)	7	3	10	0.59	0.35	0.59	0.70	0.43	0.64	1.47	−15.90	105.78

Table B.6.: Event-based statistics for the base levels of the solar wind speed [km/s] modeled by EUHFORIA and ENLIL covering the time range March to June 2008. For a detailed description of the event-based variables see Table B.5.

Model	TP	FP	FN	FAR	TS	BS	POD	RUS	Mean dt	Std dt	Mean dv	Std dv
EUHFORIA (default) (Fig. A.19)	0	9	4	1.00	0.00	2.25	0.00	NaN	NaN	NaN	NaN	NaN
EUHFORIA (range: ±2) (Fig. A.20)	0	9	4	1.00	0.00	2.25	0.00	NaN	NaN	NaN	NaN	NaN
EUHFORIA (range: ±3) (Fig. A.21)	0	9	4	1.00	0.00	2.25	0.00	NaN	NaN	NaN	NaN	NaN
EUHFORIA (range: ±5) (Fig. A.22)	0	9	4	1.00	0.00	2.25	0.00	NaN	NaN	NaN	NaN	NaN
EUHFORIA (shift: −2) (Fig. A.23)	0	8	4	1.00	0.00	2.00	0.00	NaN	NaN	NaN	NaN	NaN
EUHFORIA (shift: −1) (Fig. A.24)	0	8	4	1.00	0.00	2.00	0.00	NaN	NaN	NaN	NaN	NaN
EUHFORIA (shift: +1) (Fig. A.25)	0	9	4	1.00	0.00	2.25	0.00	NaN	NaN	NaN	NaN	NaN
EUHFORIA (shift: +2) (Fig. A.26)	0	9	4	1.00	0.00	2.25	0.00	NaN	NaN	NaN	NaN	NaN
ENLIL (Fig. A.34)	0	3	4	1.00	0.00	0.75	0.00	NaN	NaN	NaN	NaN	NaN

Table B.7.: Event-based statistics for the peaks of the solar wind speed [km/s] modeled by EUHFORIA and ENLIL covering the time range March to May 2012.

Model	TP	FP	FN	FAR	TS	BS	POD	RUS	Mean dt	Std dt	Mean dv	Std dv
EUHFORIA/YES (default) (Fig. 6.7)	3	1	8	0.73	0.25	0.36	0.75	1.00	−0.25	1.39	−159.52	48.36
EUHFORIA//NO (default) (Fig. 6.7)	3	1	5	0.62	0.33	0.50	0.75	1.00	−0.25	1.39	−159.52	48.36
EUHFORIA/YES (range: ±2) (Fig. A.12)	3	0	8	0.73	0.27	0.27	1.00	1.00	0.33	1.61	−173.25	42.50
EUHFORIA/NO (range: ±2) (Fig. A.12)	3	0	5	0.62	0.38	0.38	1.00	1.00	0.33	1.61	−173.25	42.50
EUHFORIA/YES (range: ±3) (Fig. A.13)	3	0	8	0.73	0.27	0.27	1.00	1.00	0.17	1.38	−181.39	34.63
EUHFORIA/NO (range: ±3) (Fig. A.13)	3	0	5	0.62	0.38	0.38	1.00	1.00	0.17	1.38	−181.39	34.63
EUHFORIA/YES (range: ±5) (Fig. A.14)	2	0	9	0.82	0.18	0.18	1.00	1.00	0.12	0.18	−167.63	14.44
EUHFORIA/NO (range: ±5) (Fig. A.14)	2	0	6	0.75	0.25	0.25	1.00	1.00	0.12	0.18	−167.63	14.44
EUHFORIA/YES (shift: −2) (Fig. A.15)	2	1	9	0.82	0.17	0.27	0.67	1.00	−0.75	1.06	−136.66	47.87
EUHFORIA/NO (shift: −2) (Fig. A.15)	2	1	6	0.75	0.22	0.38	0.67	1.00	−0.75	1.06	−136.66	47.87
EUHFORIA/YES (shift: −1) (Fig. A.16)	2	2	9	0.82	0.15	0.36	0.50	1.00	0.62	0.18	−183.56	22.41
EUHFORIA/NO (shift: −1) (Fig. A.16)	2	2	6	0.75	0.20	0.50	0.50	1.00	0.62	0.18	−183.56	22.41
EUHFORIA/YES (shift: +1) (Fig. A.17)	3	1	8	0.73	0.25	0.36	0.75	1.00	0.08	0.63	−164.46	35.97
EUHFORIA/NO (shift: +1) (Fig. A.17)	3	1	5	0.62	0.33	0.50	0.75	1.00	0.08	0.63	−164.46	35.97
EUHFORIA/YES (shift: +2) (Fig. A.18)	5	0	6	0.55	0.45	0.45	1.00	0.80	0.35	1.28	−96.20	105.29
EUHFORIA/NO (shift: +2) (Fig. A.18)	5	0	3	0.38	0.62	0.62	1.00	0.80	0.35	1.28	−96.20	105.29
ENLIL/YES (Fig. 6.8)	4	3	7	0.64	0.29	0.64	0.57	0.50	−0.69	1.09	11.16	105.62
ENLIL/NO (Fig. 6.8)	4	3	4	0.50	0.36	0.88	0.57	0.50	−0.69	1.09	11.16	105.62

Table B.8.: Event-based statistics for the base levels of the solar wind speed [km/s] modeled by EUHFORIA and ENLIL covering the time range March to May 2012.

Model	TP	FP	FN	FAR	TS	BS	POD	RUS	Mean dt	Std dt	Mean dv	Std dv
EUHFORIA/YES (default) (Fig. A.19)	0	4	6	1.00	0.00	0.67	0.00	NaN	NaN	NaN	NaN	NaN
EUHFORIA//NO (default) (Fig. A.19)	2	5	3	0.60	0.20	1.40	0.29	1.00	-1.69	0.27	-28.59	1.32
EUHFORIA/YES (range: ±2) (Fig. A.20)	1	2	5	0.83	0.12	0.50	0.33	1.00	-0.50	0.00	-82.79	0.00
EUHFORIA/NO (range: ±2) (Fig. A.20)	2	4	3	0.60	0.22	1.20	0.33	1.00	-1.62	0.35	-24.55	1.79
EUHFORIA/YES (range: ±3) (Fig. A.21)	1	2	5	0.83	0.12	0.50	0.33	1.00	-0.50	0.00	-82.28	0.00
EUHFORIA/NO (range: ±3) (Fig. A.21)	2	4	3	0.60	0.22	1.20	0.33	1.00	-1.62	0.35	-21.93	2.77
EUHFORIA/YES (range: ±5) (Fig. A.22)	1	2	5	0.83	0.12	0.50	0.33	1.00	-0.38	0.00	-80.70	0.00
EUHFORIA/NO (range: ±5) (Fig. A.22)	2	4	3	0.60	0.22	1.20	0.33	1.00	-1.62	0.35	-18.97	2.31
EUHFORIA/YES (shift: −2) (Fig. A.23)	0	4	6	1.00	0.00	0.67	0.00	NaN	NaN	NaN	NaN	NaN
EUHFORIA/NO (shift: −2) (Fig. A.23)	2	5	3	0.60	0.20	1.40	0.29	1.00	-1.69	0.27	-23.15	19.06
EUHFORIA/YES (shift: −1) (Fig. A.24)	0	4	6	1.00	0.00	0.67	0.00	NaN	NaN	NaN	NaN	NaN
EUHFORIA/NO (shift: −1) (Fig. A.24)	1	6	4	0.80	0.09	1.40	0.14	1.00	-1.50	0.00	-18.90	0.00
EUHFORIA/YES (shift: +1) (Fig. A.25)	0	4	6	1.00	0.00	0.67	0.00	NaN	NaN	NaN	NaN	NaN
EUHFORIA/NO (shift: +1) (Fig. A.25)	1	6	4	0.80	0.09	1.40	0.14	1.00	-1.00	0.00	-25.17	0.00
EUHFORIA/YES (shift: +2) (Fig. A.26)	0	5	6	1.00	0.00	0.83	0.00	NaN	NaN	NaN	NaN	NaN
EUHFORIA/NO (shift: +2) (Fig. A.26)	2	6	3	0.60	0.18	1.60	0.25	0.50	0.00	0.88	-5.10	21.03
ENLIL/YES (Fig. A.34)	1	6	5	0.83	0.08	1.17	0.14	1.00	0.38	0.00	-11.80	0.00
ENLIL/NO (Fig. A.34)	2	5	3	0.60	0.20	1.40	0.29	1.00	-0.62	1.41	-8.60	4.53

Table B.9.: Statistical results of the continuous variables for the solar wind parameters modeled by EUHFORIA and ENLIL covering the time range March to June 2008.

Parameter	ME	MAE	RMSE	Mean M	Std M	Mean F	Std F	Unit
EUHFORIA Bulk velocity v_b (default) (Fig. 6.7)	57.86	106.43	135.36	492.40	104.95	434.54	89.23	[km s^{-1}]
EUHFORIA Bulk velocity v_b (shift: +2) (Fig. A.18)	59.03	103.98	132.03	492.40	104.95	433.38	86.56	[km s^{-1}]
EUHFORIA Density n (default) (Fig. 6.9)	−8.30	8.39	10.76	2.12	2.18	10.42	7.19	[cm^{-3}]
EUHFORIA Density n (shift: +2) (Fig. A.28)	−8.23	8.30	10.37	2.12	2.18	10.34	6.46	[cm^{-3}]
EUHFORIA Pressure P (default) (Fig. 6.10)	−5.16	6.20	9.32	3.57	4.65	8.73	7.89	[$10^{-12}\times$Pa]
EUHFORIA Pressure P (shift: +2) (Fig. A.29)	−4.97	6.00	8.35	3.57	4.65	8.54	6.31	[$10^{-12}\times$Pa]
EUHFORIA Temperature T (default) (Fig. 6.11)	58.99	80.02	107.04	125.69	81.27	66.70	30.18	[$10^{3}\times$K]
EUHFORIA Temperature T (shift: +2) (Fig. A.30)	58.97	77.11	101.76	125.69	81.27	66.71	29.90	[$10^{3}\times$K]
EUHFORIA Total magnetic field B_t (default) (Fig. 6.12)	3.05	3.06	3.54	5.19	1.60	2.14	0.75	[nT]
EUHFORIA Total magnetic field B_t (shift: +2) (Fig. A.31)	3.04	3.09	3.54	5.19	1.60	2.15	0.76	[nT]
EUHFORIA Magnetic field B_z (default) (Fig. 6.13)	2.56	2.79	3.20	2.60	1.65	0.03	0.80	[nT]
EUHFORIA Magnetic field B_z (shift: +2) (Fig. A.32)	2.60	2.85	3.25	2.60	1.65	-0.00	0.83	[nT]
ENLIL Bulk velocity v_b (Fig. 6.8)	6.71	81.60	101.78	492.40	104.95	485.70	100.39	[km s^{-1}]
ENLIL Density n (Fig. A.35)	−3.39	3.79	4.60	2.12	2.18	5.51	2.54	[cm^{-3}]
ENLIL Pressure P (Fig. A.36)	−1.15	3.17	4.93	3.57	4.65	4.72	2.55	[$10^{-12}\times$Pa]
ENLIL Temperature T (Fig. A.37)	60.39	70.73	97.21	125.69	81.27	65.30	21.63	[$10^{3}\times$K]
ENLIL Total magnetic field B_t (Fig. A.38)	2.48	2.60	2.99	5.19	1.60	2.71	1.19	[nT]
ENLIL Magnetic field B_z (Fig. A.39)	0.22	1.42	1.81	2.60	1.65	2.37	0.83	[nT]

Table B.10.: Statistical results of the continuous variables for the solar wind parameters modeled by EUHFORIA and ENLIL covering the time range March to May 2012.

Parameter	ME	MAE	RMSE	Mean M	Std M	Mean F	Std F	Unit
EUHFORIA/YES Bulk velocity v_b (default) (Fig. 6.7)	102.34	108.75	140.22	417.76	95.25	315.42	52.07	[km s^{-1}]
EUHFORIA/NO Bulk velocity v_b (default) (Fig. 6.7)	96.11	102.86	131.60	413.00	90.63	316.90	54.38	[km s^{-1}]
EUHFORIA/YES Bulk velocity v_b (shift: +2) (Fig. A.18)	99.31	104.88	137.76	417.76	95.25	318.45	50.54	[km s^{-1}]
EUHFORIA/NO Bulk velocity v_b (shift: +2) (Fig. A.18)	93.03	99.10	128.90	413.00	90.63	319.98	52.61	[km s^{-1}]
EUHFORIA/YES Density n (default) (Fig. 6.9)	−12.01	12.12	14.08	2.22	2.63	14.23	6.78	[cm^{-3}]
EUHFORIA/NO Density n (default) (Fig. 6.9)	−11.87	11.95	13.99	2.23	2.65	14.10	6.89	[cm^{-3}]
EUHFORIA/YES Density n (shift: +2) (Fig. A.28)	−12.26	12.32	14.53	2.22	2.63	14.48	7.24	[cm^{-3}]
EUHFORIA/NO Density n (shift: +2) (Fig. A.28)	−12.17	12.19	14.51	2.23	2.65	14.39	7.41	[cm^{-3}]
EUHFORIA/YES Pressure P (default) (Fig. 6.10)	−2.29	4.51	6.42	2.53	4.63	4.83	3.60	[$10^{-12}\times$Pa]
EUHFORIA/NO Pressure P (default) (Fig. 6.10)	−2.10	4.46	6.44	2.65	4.75	4.75	3.64	[$10^{-12}\times$Pa]
EUHFORIA/YES Pressure P (shift: +2) (Fig. A.29)	−2.87	5.10	7.40	2.53	4.63	5.40	4.85	[$10^{-12}\times$Pa]
EUHFORIA/NO Pressure P (shift: +2) (Fig. A.29)	−2.74	5.07	7.53	2.65	4.75	5.39	5.02	[$10^{-12}\times$Pa]
EUHFORIA/YES Temperature T (default) (Fig. 6.11)	61.55	70.49	101.64	85.61	81.67	24.06	9.40	[$10^3\times$K]
EUHFORIA/NO Temperature T (default) (Fig. 6.11)	63.66	71.95	102.57	87.65	81.34	23.99	9.57	[$10^3\times$K]
EUHFORIA/YES Temperature T (shift: +2) (Fig. A.30)	59.91	71.15	102.69	85.61	81.67	25.71	11.94	[$10^3\times$K]
EUHFORIA/NO Temperature T (shift: +2) (Fig. A.30)	61.89	72.61	103.63	87.65	81.34	25.76	12.31	[$10^3\times$K]
EUHFORIA/YES Total magnetic field B_t (default) (Fig. 6.12)	4.20	4.21	5.02	6.15	2.75	1.95	0.64	[nT]
EUHFORIA/NO Total magnetic field B_t (default) (Fig. 6.12)	3.93	3.93	4.65	5.88	2.46	1.95	0.65	[nT]
EUHFORIA/YES Total magnetic field B_t (shift: +2) (Fig. A.31)	4.30	4.34	5.14	6.15	2.75	1.85	0.68	[nT]
EUHFORIA/NO Total magnetic field B_t (shift: +2) (Fig. A.31)	4.01	4.05	4.76	5.88	2.46	1.86	0.69	[nT]
EUHFORIA/YES Magnetic field B_z (default) (Fig. 6.13)	2.19	3.08	3.93	2.11	2.99	-0.08	1.30	[nT]
EUHFORIA/NO Magnetic field B_z (default) (Fig. 6.13)	2.29	2.99	3.81	2.24	2.66	-0.05	1.31	[nT]
EUHFORIA/YES Magnetic field B_z (shift: +2) (Fig. A.32)	2.26	3.21	4.04	2.11	2.99	-0.15	1.26	[nT]
EUHFORIA/NO Magnetic field B_z (shift: +2) (Fig. A.32)	2.37	3.14	3.95	2.24	2.66	-0.14	1.28	[nT]
ENLIL/YES: Bulk velocity v_b (Fig. 6.8)	30.36	93.91	130.73	417.76	95.25	387.40	79.37	[km s^{-1}]
ENLIL/NO Bulk velocity v_b (Fig. 6.8)	21.38	89.38	122.77	413.00	90.63	391.62	81.58	[km s^{-1}]
ENLIL/YES Density n (Fig. A.35)	−6.85	7.33	9.38	2.22	2.63	9.07	5.59	[cm^{-3}]
ENLIL/NO Density n (Fig. A.35)	−6.68	7.17	9.21	2.23	2.65	8.91	5.58	[cm^{-3}]
ENLIL/YES Pressure P (Fig. A.36)	−3.72	5.58	8.59	2.53	4.63	6.25	5.89	[$10^{-12}\times$Pa]
ENLIL/NO Pressure P (Fig. A.36)	−3.57	5.53	8.72	2.65	4.75	6.22	6.05	[$10^{-12}\times$Pa]
ENLIL/YES Temperature T (Fig. A.37)	37.62	61.97	93.25	85.61	81.67	48.00	18.92	[$10^3\times$K]
ENLIL/NO Temperature T (Fig. A.37)	39.06	62.91	93.93	87.65	81.34	48.59	19.45	[$10^3\times$K]
ENLIL/YES Total magnetic field B_t (Fig. A.38)	3.53	3.92	4.80	6.15	2.75	2.62	1.78	[nT]
ENLIL/NO Total magnetic field B_t (Fig. A.38)	3.27	3.69	4.45	5.88	2.46	2.60	1.79	[nT]
ENLIL/YES Magnetic field B_z (Fig. A.39)	−-0.18	2.50	3.30	2.11	2.99	2.29	1.41	[nT]
ENLIL/NO Magnetic field B_z (Fig. A.39)	−0.03	2.28	2.98	2.24	2.66	2.27	1.41	[nT]

Bibliography

Alfvén, H. (1977). Electric currents in cosmic plasmas. *Reviews of Geophysics and Space Physics*, 15:271–284.

Altschuler, M. D. and Newkirk, G. (1969). Magnetic Fields and the Structure of the Solar Corona. I: Methods of Calculating Coronal Fields. *Solar Phys.*, 9:131–149.

Arge, C. N., Odstrcil, D., Pizzo, V. J., and Mayer, L. R. (2003). Improved Method for Specifying Solar Wind Speed Near the Sun. In Velli, M., Bruno, R., Malara, F., and Bucci, B., editors, *Solar Wind Ten*, volume 679 of *American Institute of Physics Conference Series*, pages 190–193.

Arge, C. N. and Pizzo, V. J. (2000). Improvement in the prediction of solar wind conditions using near-real time solar magnetic field updates. *J. Geophys. Res.*, 105:10465–10480.

Aschwanden, M. J. (2005). *Physics of the Solar Corona. An Introduction with Problems and Solutions (2nd edition)*.

Bhatnagar, A. and Livingston, W. (2005). *Fundamentals of Solar Astronomy*.

Biermann, L. (1951). Kometenschweife und solare Korpuskularstrahlung. *Z. Astrophys.*, 29:274.

Burgess, D. and Scholer, M. (2015). *Collisionless Shocks in Space Plasmas: Structure and Accelerated Particles*. Cambridge Atmospheric and Space Science Series. Cambridge University Press.

Burt, J. and Smith, B. (2012). Deep space climate observatory: The dscovr mission. *2012 IEEE Aerospace Conference*, pages 1–13.

Chapman, S. and Zirin, H. (1957). Notes on the Solar Corona and the Terrestrial Ionosphere. *Smithsonian Contributions to Astrophysics*, 2:1.

Cranmer, S. R. (2002). Coronal Holes and the High-Speed Solar Wind. *Space Sci. Rev.*, 101:229–294.

Cranmer, S. R. (2004). Coronal Heating Versus Solar Wind Acceleration. In Walsh, R. W., Ireland, J., Danesy, D., and Fleck, B., editors, *SOHO 15 Coronal Heating*, volume 575 of *ESA Special Publication*, page 154.

Cranmer, S. R. (2009). Coronal Holes. *Living Reviews in Solar Physics*, 6:3.

Delaboudinière, J.-P., Artzner, G. E., Brunaud, J., Gabriel, A. H., Hochedez, J. F., Millier, F., Song, X. Y., Au, B., Dere, K. P., Howard, R. A., Kreplin, R., Michels, D. J., Moses, J. D., Defise, J. M., Jamar, C., Rochus, P., Chauvineau, J. P., Marioge, J. P., Catura, R. C., Lemen, J. R., Shing, L., Stern, R. A., Gurman, J. B., Neupert, W. M., Maucherat, A., Clette, F., Cugnon, P., and van Dessel, E. L. (1995). EIT: Extreme-Ultraviolet Imaging Telescope for the SOHO Mission. *Solar Phys.*, 162:291–312.

Domingo, V., Fleck, B., and Poland, A. I. (1995). The SOHO Mission: an Overview. *Solar Phys.*, 162:1–37.

Foukal, P. V. (2004). *Solar Astrophysics, 2nd, Revised Edition*.

Galvin, A. B., Kistler, L. M., Popecki, M. A., Farrugia, C. J., Simunac, K. D. C., Ellis, L., Möbius, E., Lee, M. A., Boehm, M., Carroll, J., Crawshaw, A., Conti, M., Demaine, P., Ellis, S., Gaidos, J. A., Googins, J., Granoff, M., Gustafson, A., Heirtzler, D., King, B., Knauss, U., Levasseur, J., Longworth, S., Singer, K., Turco, S., Vachon, P., Vosbury, M., Widholm, M., Blush, L. M., Karrer, R., Bochsler, P., Daoudi, H., Etter, A., Fischer, J., Jost, J., Opitz, A., Sigrist, M., Wurz, P., Klecker, B., Ertl, M., Seidenschwang, E., Wimmer-Schweingruber, R. F., Koeten, M., Thompson, B., and Steinfeld, D. (2008). The Plasma and Suprathermal Ion Composition (PLASTIC) Investigation on the STEREO Observatories. *Space Sci. Rev.*, 136:437–486.

Gómez-Herrero, R., Malandraki, O., Dresing, N., Kilpua, E., Heber, B., Klassen, A., Müller-Mellin, R., and Wimmer-Schweingruber, R. F. (2011). Spatial and temporal variations of CIRs: Multi-point observations by STEREO. *Journal of Atmospheric and Solar-Terrestrial Physics*, 73:551–565.

Gosling, J. T. and Pizzo, V. J. (1999). Formation and Evolution of Corotating Interaction Regions and their Three Dimensional Structure. *Space Sci. Rev.*, 89:21–52.

Gressl, C., Veronig, A. M., Temmer, M., Odstrčil, D., Linker, J. A., Mikić, Z., and Riley, P. (2014). Comparative Study of MHD Modeling of the Background Solar Wind. *Solar Phys.*, 289:1783–1801.

Hady, A. A. (2009). Descriptive study of solar activity sudden increase and Halloween storms of 2003. *Journal of Atmospheric and Solar-Terrestrial Physics*, 71:1711–1716.

Hanslmeier, A., editor (2002). *The Sun and Space Weather*, volume 277 of *Astrophysics and Space Science Library*.

Howard, R. A., Moses, J. D., Socker, D. G., Dere, K. P., Cook, J. W., and Secchi Consortium (2002). Sun earth connection coronal and heliospheric investigation (SECCHI). *Advances in Space Research*, 29:2017–2026.

Hundhausen, A. J., Sawyer, C. B., House, L., Illing, R. M. E., and Wagner, W. J. (1984). Coronal mass ejections observed during the solar maximum mission - Latitude distribution and rate of occurrence. *J. Geophys. Res.*, 89:2639–2646.

Jian, L., Russell, C. T., Luhmann, J. G., and Skoug, R. M. (2006). Properties of interplanetary coronal mass ejections at one au during 1995 – 2004. *Solar Physics*, 239(1):393–436.

Kaiser, M. L., Kucera, T. A., Davila, J. M., St. Cyr, O. C., Guhathakurta, M., and Christian, E. (2008). The STEREO Mission: An Introduction. *Space Sci. Rev.*, 136:5–16.

Kataoka, R. and Miyoshi, Y. (2006). Flux enhancement of radiation belt electrons during geomagnetic storms driven by coronal mass ejections and corotating interaction regions. *Space Weather*, 4:09004.

Kohutova, P., Bocquet, F.-X., Henley, E. M., and Owens, M. J. (2016). Improving solar wind persistence forecasts: Removing transient space weather events, and using observations away from the sun-earth line. *Space Weather*, 14(10):802–818. 2016SW001447.

Krista, L. D. and Gallagher, P. T. (2009). Automated Coronal Hole Detection Using Local Intensity Thresholding Techniques. *Solar Phys.*, 256:87–100.

Lee, C. O., Luhmann, J. G., Odstrcil, D., MacNeice, P. J., de Pater, I., Riley, P., and Arge, C. N. (2009). The Solar Wind at 1 AU During the Declining Phase of Solar Cycle 23: Comparison of 3D Numerical Model Results with Observations. *Solar Phys.*, 254:155–183.

Lemen, J. R., Title, A. M., Akin, D. J., Boerner, P. F., Chou, C., Drake, J. F., Duncan, D. W., Edwards, C. G., Friedlaender, F. M., Heyman, G. F., Hurlburt, N. E., Katz, N. L., Kushner, G. D., Levay, M., Lindgren, R. W., Mathur, D. P., McFeaters, E. L., Mitchell, S., Rehse, R. A., Schrijver, C. J., Springer, L. A., Stern, R. A., Tarbell, T. D., Wuelser, J.-P., Wolfson, C. J., Yanari, C., Bookbinder, J. A., Cheimets, P. N., Caldwell, D., Deluca, E. E., Gates, R., Golub, L., Park, S., Podgorski, W. A., Bush, R. I., Scherrer, P. H., Gummin, M. A., Smith, P., Auker, G., Jerram, P., Pool, P., Soufli, R., Windt, D. L., Beardsley, S., Clapp, M., Lang, J., and Waltham, N. (2012). The Atmospheric Imaging Assembly (AIA) on the Solar Dynamics Observatory (SDO). *Solar Phys.*, 275:17–40.

Lepping, R. P., Acũna, M. H., Burlaga, L. F., Farrell, W. M., Slavin, J. A., Schatten, K. H., Mariani, F., Ness, N. F., Neubauer, F. M., Whang, Y. C., Byrnes, J. B., Kennon, R. S., Panetta, P. V., Scheifele, J., and Worley, E. M. (1995). The Wind Magnetic Field Investigation. *Space Sci. Rev.*, 71:207–229.

Levine, R. H., Altschuler, M. D., and Harvey, J. W. (1977). Solar sources of the interplanetary magnetic field and solar wind. *J. Geophys. Res.*, 82:1061–1065.

Luhmann, J. G., Curtis, D. W., Lin, R. P., Larson, D., Schroeder, P., Cummings, A., Mewaldt, R. A., Stone, E. C., Davis, A., von Rosenvinge, T., Acuna, M. H., Reames, D., Ng, C., Ogilvie, K., Mueller-Mellin, R., Kunow, H., Mason, G. M., Wiedenbeck, M., Sauvaud, A., Aoustin, C., Louarn, P., Dandouras, J., Korth, A., Bothmer, V., Vasyliunas, V., Sanderson, T., Marsden, R. G., Russell, C. T., Gosling, J. T., Bougeret, J. L., McComas, D. J., Linker, J. A., Riley, P., Odstrcil, D., Pizzo, V. J., Gombosi, T., DeZeeuw, D., and Kecskemety, K. (2005). IMPACT: Science goals and firsts with STEREO. *Advances in Space Research*, 36:1534–1543.

MacNeice, P. (2009). Validation of community models: Identifying events in space weather model timelines. *Space Weather*, 7(6):n/a–n/a. S06004.

McComas, D. J., Bame, S. J., Barker, P., Feldman, W. C., Phillips, J. L., Riley, P., and Griffee, J. W. (1998). Solar Wind Electron Proton Alpha Monitor (SWEPAM) for the Advanced Composition Explorer. *Space Sci. Rev.*, 86:563–612.

McComas, D. J., Elliott, H. A., Schwadron, N. A., Gosling, J. T., Skoug, R. M., and Goldstein, B. E. (2003). The three-dimensional solar wind around solar maximum. *GeoRL*, 30:1517.

Mullan, D. J. (2000). Solar Physics: From the Deep Interior to the Hot Corona. In Page, D. and Hirsch, J. G., editors, *From the Sun to the Great Attractor*, volume 556 of *Lecture Notes in Physics, Berlin Springer Verlag*, page 1.

Neugebauer, M. and Snyder, C. W. (1966). Mariner-2 Measurements of the Solar Wind. In Mackin, Jr., R. J. and Neugebauer, M., editors, *The Solar Wind*, page 3.

NOAA Satellite and Information Service (2018). NOAA Satellite and Information Service Deep Space Climate Observatory (DSCOVR) PLASMA-MAGNETOMETER (PlasMag).

Odstrcil, D. (2003). Modeling 3-D solar wind structure. *Advances in Space Research*, 32:497–506.

Odstrcil, D., Linker, J. A., Lionello, R., Mikic, Z., Riley, P., Pizzo, V. J., and Luhmann, J. G. (2002). Merging of coronal and heliospheric numerical two-dimensional mhd models. *Journal of Geophysical Research: Space Physics*, 107(A12):SSH 14–1–SSH 14–11. 1493.

Oliveira, D. M. and Samsonov, A. A. (2018). Geoeffectiveness of interplanetary shocks controlled by impact angles: A review. *Advances in Space Research*, 61:1–44.

Owens, M. J., Arge, C. N., Spence, H. E., and Pembroke, A. (2005). An event-based approach to validating solar wind speed predictions: High-speed enhancements in the wang-sheeley-arge model. *Journal of Geophysical Research: Space Physics*, 110(A12):n/a–n/a. A12105.

Owens, M. J., Challen, R., Methven, J., Henley, E., and Jackson, D. R. (2013). A 27 day persistence model of near-Earth solar wind conditions: A long lead-time forecast and a benchmark for dynamical models. *Space Weather*, 11:225–236.

Owens, M. J., Spence, H. E., McGregor, S., Hughes, W. J., Quinn, J. M., Arge, C. N., Riley, P., Linker, J., and Odstrcil, D. (2008). Metrics for solar wind prediction models: Comparison of empirical, hybrid, and physics-based schemes with 8 years of L1 observations. *Space Weather*, 6:S08001.

Parker, E. N. (1958). Dynamics of the Interplanetary Gas and Magnetic Fields. *ApJ*, 128:664.

Parker, E. N. (1965). Dynamical Theory of the Solar Wind. *Space Sci. Rev.*, 4:666–708.

Pesnell, W. D., Thompson, B. J., and Chamberlin, P. C. (2012). The Solar Dynamics Observatory (SDO). *Solar Phys.*, 275:3–15.

Pomoell, J. and Poedts, S. (2018). EUHFORIA: EUropean Heliospheric FORecasting Infromation Asset. *Submitted to SWSC*.

Reiss, M. A., Temmer, M., Veronig, A. M., Nikolic, L., Vennerstrom, S., Schöngassner, F., and Hofmeister, S. J. (2016). Verification of high-speed solar wind stream forecasts using operational solar wind models. *Space Weather*, 14:495–510.

Richardson, I. G. and Cane, H. V. (2010). Near-earth interplanetary coronal mass ejections during solar cycle 23 (1996 – 2009): Catalog and summary of properties. *Solar Physics*, 264(1):189–237.

Richardson, I. G., Cane, H. V., and Cliver, E. W. (2002). Sources of geomagnetic activity during nearly three solar cycles (1972-2000). *Journal of Geophysical Research (Space Physics)*, 107:1187.

Riley, P., Linker, J. A., and Mikić, Z. (2001). An empirically-driven global MHD model of the solar corona and inner heliosphere. *J. Geophys. Res.*, 106:15889–15902.

Rotter, T., Veronig, A. M., Temmer, M., and Vršnak, B. (2012). Relation Between Coronal Hole Areas on the Sun and the Solar Wind Parameters at 1 AU. *Solar Phys.*, 281:793–813.

Rotter, T., Veronig, A. M., Temmer, M., and Vršnak, B. (2015). Real-Time Solar Wind Prediction Based on SDO/AIA Coronal Hole Data. *Solar Phys.*, 290:1355–1370.

Sakao, T., Kano, R., Narukage, N., Kotoku, J., Bando, T., DeLuca, E. E., Lundquist, L. L., Tsuneta, S., Harra, L. K., Katsukawa, Y., Kubo, M., Hara, H., Matsuzaki, K., Shimojo, M., Bookbinder, J. A., Golub, L., Korreck, K. E., Su, Y., Shibasaki,

K., Shimizu, T., and Nakatani, I. (2007). Continuous Plasma Outflows from the Edge of a Solar Active Region as a Possible Source of Solar Wind. *Science*, 318:1585.

Schatten, K. H., Wilcox, J. M., and Ness, N. F. (1969). A model of interplanetary and coronal magnetic fields. *Solar Phys.*, 6:442–455.

Schou, J., Scherrer, P. H., Bush, R. I., Wachter, R., Couvidat, S., Rabello-Soares, M. C., Bogart, R. S., Hoeksema, J. T., Liu, Y., Duvall, T. L., Akin, D. J., Allard, B. A., Miles, J. W., Rairden, R., Shine, R. A., Tarbell, T. D., Title, A. M., Wolfson, C. J., Elmore, D. F., Norton, A. A., and Tomczyk, S. (2012). Design and Ground Calibration of the Helioseismic and Magnetic Imager (HMI) Instrument on the Solar Dynamics Observatory (SDO). *Solar Phys.*, 275:229–259.

Schwenn, R. (1990). *Large-Scale Structure of the Interplanetary Medium*, page 99.

Schwenn, R. (1996). An Essay on Terminology, Myths and Known Facts: Solar Transient - Flare - CME - Driver Gas - Piston - BDE - Magnetic Cloud - Shock Wave - Geomagnetic Storm. *Astrophys. Space Sci.*, 243:187.

Schwenn, R. (2000). *Solar Wind: Global Properties*, page 2301.

Schwenn, R. (2006a). Solar Wind Sources and Their Variations Over the Solar Cycle. *Space Sci. Rev.*, 124:51–76.

Schwenn, R. (2006b). Space Weather: The Solar Perspective. *Living Reviews in Solar Physics*, 3:2.

Smith, C. W., L'Heureux, J., Ness, N. F., Acuña, M. H., Burlaga, L. F., and Scheifele, J. (1998). The ACE Magnetic Fields Experiment. *Space Sci. Rev.*, 86:613–632.

Stone, E. C., Frandsen, A. M., Mewaldt, R. A., Christian, E. R., Margolies, D., Ormes, J. F., and Snow, F. (1998). The Advanced Composition Explorer. *Space Sci. Rev.*, 86:1–22.

Temmer, M., Hinterreiter, J., and Reiss, M. A. (2018). Coronal hole evolution from multi-viewpoint data as input for a STEREO solar wind speed persistence model. arXiv:1801.10213.

Timothy, A. F., Krieger, A. S., and Vaiana, G. S. (1975). The structure and evolution of coronal holes. *Solar Phys.*, 42:135–156.

Tóth, G. and Odstrčil, D. (1996). Comparison of Some Flux Corrected Transport and Total Variation Diminishing Numerical Schemes for Hydrodynamic and Magnetohydrodynamic Problems. *Journal of Computational Physics*, 128:82–100.

Vennerstrom, S. and Leer, K. (2015). Automated classification of solar wind disturbances. In *EGU General Assembly Conference Abstracts*, volume 17 of *EGU General Assembly Conference Abstracts*, page 9817.

Volpes, L. and Bothmer, V. (2015). An Application of the Stereoscopic Self-similar-Expansion Model to the Determination of CME-Driven Shock Parameters. *Solar Phys.*, 290:3005–3022.

Vršnak, B., Temmer, M., and Veronig, A. M. (2007). Coronal Holes and Solar Wind High-Speed Streams: II. Forecasting the Geomagnetic Effects. *Solar Phys.*, 240:331–346.

Wang, Y.-M. and Sheeley, Jr., N. R. (1990). Solar wind speed and coronal flux-tube expansion. *ApJ*, 355:726–732.

Wenzel, K. P., Marsden, R. G., Page, D. E., and Smith, E. J. (1992). The ULYSSES Mission. *Astron. Astrophys. Suppl. Ser.*, 92:207.

Woodcock, F. (1976). The Evaluation of Yes/No Forecasts for Scientific and Administrative Purposes. *Monthly Weather Review*, 104:1209.

Woods, T. N., Eparvier, F. G., Hock, R., Jones, A. R., Woodraska, D., Judge, D., Didkovsky, L., Lean, J., Mariska, J., Warren, H., McMullin, D., Chamberlin, P., Berthiaume, G., Bailey, S., Fuller-Rowell, T., Sojka, J., Tobiska, W. K., and Viereck, R. (2012). Extreme Ultraviolet Variability Experiment (EVE) on the Solar Dynamics Observatory (SDO): Overview of Science Objectives, Instrument Design, Data Products, and Model Developments. *Solar Phys.*, 275:115–143.

Wuelser, J.-P., Lemen, J. R., Tarbell, T. D., Wolfson, C. J., Cannon, J. C., Carpenter, B. A., Duncan, D. W., Gradwohl, G. S., Meyer, S. B., Moore, A. S., Navarro, R. L., Pearson, J. D., Rossi, G. R., Springer, L. A., Howard, R. A., Moses, J. D., Newmark, J. S., Delaboudiniere, J.-P., Artzner, G. E., Auchere, F., Bougnet, M., Bouyries, P., Bridou, F., Clotaire, J.-Y., Colas, G., Delmotte, F., Jerome, A., Lamare, M., Mercier, R., Mullot, M., Ravet, M.-F., Song, X., Bothmer, V., and Deutsch, W. (2004). EUVI: the STEREO-SECCHI extreme ultraviolet imager. In Fineschi, S. and Gummin, M. A., editors, *Telescopes and Instrumentation for Solar Astrophysics*, volume 5171 of *Proc. SPIE*, pages 111–122.

Yashiro, S., Gopalswamy, N., Michalek, G., St. Cyr, O. C., Plunkett, S. P., Rich, N. B., and Howard, R. A. (2004). A catalog of white light coronal mass ejections observed by the SOHO spacecraft. *Journal of Geophysical Research (Space Physics)*, 109:A07105.